A first-principles investigation of the magnetic, structural and dynamical properties of Ni_2MnGa

Von der Fakultät für Naturwissenschaften
der Universität Duisburg-Essen
(Standort Duisburg)
zur Erlangung des akademischen Grades eines
Doktors der Naturwissenschaften (Dr. rer. nat.)
genehmigte Dissertation von

Alexey T. Zayak
aus
Chelyabinsk, Russland

Referent: Prof. Dr. P. Entel
Korreferent: Prof. Dr. R. Feder
Tag der mündlichen Prüfung: 24 November 2003

Abstract

This work contains the theoretical investigations of the magnetic, structural and dynamical properties of the ferromagnetic Heusler compound Ni_2MnGa. The physical properties have been studied by means of electronic structure calculations, using advanced methods of Density Functional Theory. State-of-the-art *ab-initio* computational algorithms, which are used throughout the work, ensure that no adjustable empirical parameters are required. The purpose of this work was to understand and explain the properties of Ni_2MnGa on an atomic scale, meaning that the entire variety of different crystal structures can be analysed in terms of the electronic structure and phonon spectrum. The big challenge of this work is to explain the driving forces for the martensitic transformations, which is still an unresolved problem even after one hundred years of studies.

The total energy calculations for the cubic and the tetragonal structures yield correct site ordering, lattice parameters, magnetic moments and elastic constants which are in excellent agreement with the experimental data for Ni_2MnGa. Without atomic shuffles only two stable structures could be obtained, the cubic $L2_1$ and the tetragonal distorted T structure. Supercell simulations with shuffles allowed to obtain further stable structures, in particular theexperimentally observed modulated martensitic structure called 5M. The main conclusion here is that the atomic shuffles play a principal role in stabilizing the modulated structures.

As origin of the modulated shuffles one can consider the transverse acoustic phonon mode TA_2 -[110], which has been found to completely soften for a particular wave vector related to the modulation which appears at low-temperature. The other two acoustic modes of Ni_2MnGa, which do not soften, are coupled to the optical modes of Ni lying at rather low energies, giving rise to hybridization of acoustic-optical modes. This coupling of acoustic and optical modes is directly related to the modulated structures of Ni_2MnGa which is a completely novel feature of martensitic transformations. Further analysis showed that the electron-phonon coupling should be particularly strong in Ni_2MnGa; this problem is left for future work.

Additionally, some calculations have been done for a single off-stoichiometric composition like $Ni_{2-x}Mn_{1+x}Ga$. The results show that off-stoichiometry yields a stable tetragonal structure with the same c/a ratio as the 5M structure has.

The analysis of the electronic structure allows to clearly identify the important role of Ni and Ga hybridized electronic states. This hybridization benefits from a non-symmetric local distribution of the nearest neighbour atoms of Ga. This can be associated with the modulation or other kinds of defects or even surfaces, which facilitate, to some extent, the optimal redistribution of hybrid electronic orbitals.

The Appendix gives a brief description of a Ginzburg-Landau type of approach applied to Ni_2MnGa. The model involves three different groups of order parameters needed to describe the homogeneous lattice distortion, the magnetization and the modulation of the lattice, which are coupled to each other. This theory, if supplied by appropriate parameters, allows to obtain realistic phase diagrams for the system describing all possible phase transitions like the magnetic, premartensitic and martensitic transition.

Contents

List of Figures

List of Tables

1 Introduction

1.1 Shape-memory Heusler alloys Ni-Mn-Ga

Heusler alloys (Campbell, 1975; Heusler, 1903; Webster, 1969) are magnetic ternary intermetallic systems with $L2_1$ (or B2) crystal structure (see Fig. 1.1) and are drived from the corresponding compounds with the generic formula X_2YZ. Here, X is usually a transition metal, such as Co, Cu, Ni, Fe or Pt; Y is usually Mn and Z can be Ge, Si, Ga, Sn, Sb, Al, In, etc. When the elements X and Z are nonmagnetic, the magnetization is essentially confined to the Mn sublattice. When the element X is Ni or Co, an additional magnetization appears at the Ni or Co sites (Kübler, Williams and Sommers, 1983; Webster, 1971).

There are two main fields where Heusler alloys are of great interest. The first field of application is spin-electronics. In the past electronic devices were designed to use the effects of the charge of the electrons, while the spin degree of freedom was not important. However, since the discovery of the Giant Magnetoresistence in 1988 there has been a great deal of research for spin dependent effects and devices. This new technology is called *spintronics*. Some Heusler alloys are predicted to be both strongly ferromagnetic and half-metallic, where the half-metalicity means that for some alloys the minority-spin density of states vanishes at the Fermi energy. This leads to particular transport properties which may be useful for various devices.

The second field of application is mainly related to the Ni_2MnGa compound and alloys derived from it. Since the discovery of a martensitic transformation, Ni_2MnGa became a material of special interest (Webster, Ziebeck, Town and Peak, 1984). This Heusler alloy is one of the very rare materials which undergoes a martensitic transformation below the Curie temperature, whereby the combination of magnetic and structural features is responsible for its unique magnetomechanical properties. From the technological

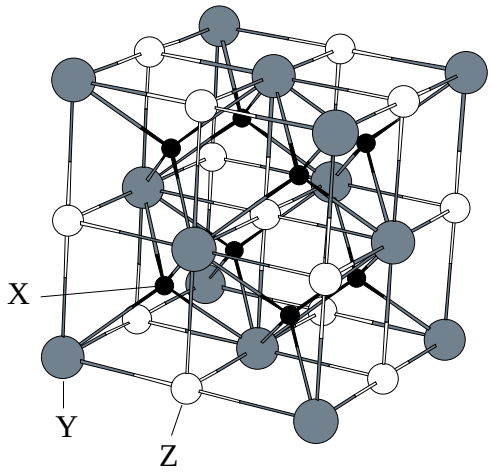

Figure 1.1: Cubic cell of the Heusler compound X_2YZ. Black, white and gray circles show the positions of the X, Y and Z atoms, respectively.

point of view, Ni_2MnGa is much more promising than other materials being presently in commercial use. In particular, the well known material Tb-Dy-Fe (Terfenol-D) exhibits magnetostrictive strains of about 0.1 %, while deformations of up to ~ 0.2 % have been observed for Ni_2MnGa at room temperature in an external magnetic field of 8 kOe (Ullakko, Huang, Kantner, O'Handley *et al.*, 1996). Recently, some groups have reported the observation of a giant magneto-strain effect (Murray, Marioni, Kukla, Robinson *et al.*, 2000; Ullakko, Sozinov and Yakovenko, 2000). Shear deformations of more than 5% have been obtained in magnetic fields of about 4 kOe (Murray, Marioni, Kukla, Robinson *et al.*, 2000). At the same time, the maximum achievable strain is estimated to be $\sim$ 6%. An important point is that the strain development and recovering of the initial state are very fast (comparable to the sound velocity in the solid). All these features together make Ni_2MnGa very efficient for the magnetic shape memory (MSM) technology (Ullakko, Huang, Kantner, O'Handley *et al.*, 1996). The MSM technology is based on the magnetic field induced redistribution of martensitic domains in the sample. Design of new efficient MSM magneto-mechanical actuator devices is on the way (Aaltio and Ullakko, 2000). They are going to be economical in use and will have a wide field of commercial applications.

1.2 Martensitic transformations

Displacive, diffusionless solid state structural transformations of the martensitic type are known to occur in many metallic alloys. The name *Martensite* is associated with the german Scientist Martens. The nature of martensite remains of the greatest technological importance, but after a century of study fundamental physics still lacks explanation of this phenomenon. Typically, upon cooling, the high-temperature symmetric phase (austenite) transforms to a low-temperature structure with lower symmetry (martensite) through a first-order phase transition (Nishiyama, 1978). These transformations involve a cooperative rather than diffusive displacements of atoms and are often associated with phonon anomalies in the parent phase and related precursor phenomena. Sometimes, the martensitic transformation is called a *shear* or *displacive transformation*. The diffusionless character of the martensitic transformations implies that martensite can form at very low temperatures, where diffusion, even of interstitial atoms, is not conceivable over the time period of the experiment. The martensitic transformation is characterized by the martensite-start, M_s, and the martensite-final, M_f, temperatures.

The martensitic transformation involves only small displacements of atoms relative to their neighbours, but the macroscopic effect is quite large. A passage of a slip dislocation through a crystal causes the formation of a step. A passage of many such dislocations on parallel slip planes causes macroscopic shear. Slip causes a change in shape but not a change in the crystal structure, because the Burgers vectors of the dislocations are also lattice vectors.

The change from the fcc to bcc crystal structure in iron can be used to discuss the mechanism of martensitic transformations. In 1924 Bain proposed that the change in the structure could be achieved by a simple homogeneous deformation illustrated in Fig.

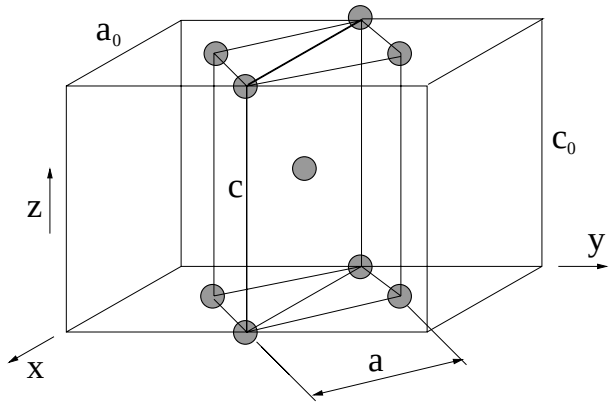

Figure 1.2: Bain (fcc → bcc) distortion of martensite. This transformation involves about 20% contraction of the parent structure along the z direction, and a uniform expansion of about 12% in x and y directions.

1.2. It is then easy to see how the bct cell of austenite may be deformed to produce the required bcc cell. Thus, the Bain strain consists of a contraction along the z axis and identical expansion along the x and y axes. The Bain strain implies the following orientational relationships between the parent and the product lattices:

$$[001]_{fcc} \parallel [001]_{bcc}, \qquad [1\underline{1}0]_{fcc} \parallel [100]_{bcc}, \qquad [110]_{fcc} \parallel [010]_{bcc},$$

but, in fact, the experimentally observed orientational relationships are irrational, e.g., close to the Kurdjumov-Sachs orientation:

$$\{111\}_{fcc} \parallel \{011\}_{bcc}, \qquad \langle 10\underline{1}\rangle_{fcc} \parallel \langle 11\underline{1}\rangle_{bcc}.$$

The Bain deformation alone would cause enormous strains yielding also a "wrong shape" of the sample, see Fig. 1.3(b), which is usually not observed in experiments. In order to avoid these intolerable strains, the martensite either slips or undergoes transformation twinning. Thus, although the Bain strain gives a wrong crystal structure, the combined effect of the Bain strain and the slip/twinning is to convert the macroscopic strain into a shear. The total strain and the whole shape of the sample is correct in this case.

The mechanism by which martensite nucleates must be consistent with a diffusionless transformation and with the fact that the phase can form at remarkably low temperatures and high strain rates. The classical idea that nucleation occurs when random phase and composition fluctuations reach a critical size is not a reasonable concept in such circumstances. The probable mechanism involves the dissociation of three-dimensional arrays of dislocations. The faulted structure between them represents the embryo, which is said to become the nucleus of martensite when the circumstances are right for rapid growth of the embryo. In most cases this means that the chemical driving force for the transformation must be large enough to allow the partially transformed regions to propagate with a rate limited only by the usual barriers for dislocation motion. This theory is particularly useful because it correctly predicts that the activation energy for nucleation is directly proportional to the driving force of the transformation. This behaviour is not expected in classical nucleation by heterophase fluctuations. There have also been many proposals that nucleation involves some sort of lattice instability or a strain spinodal. This approach can be useful in case that the driving force of the transformation is extremely large. In

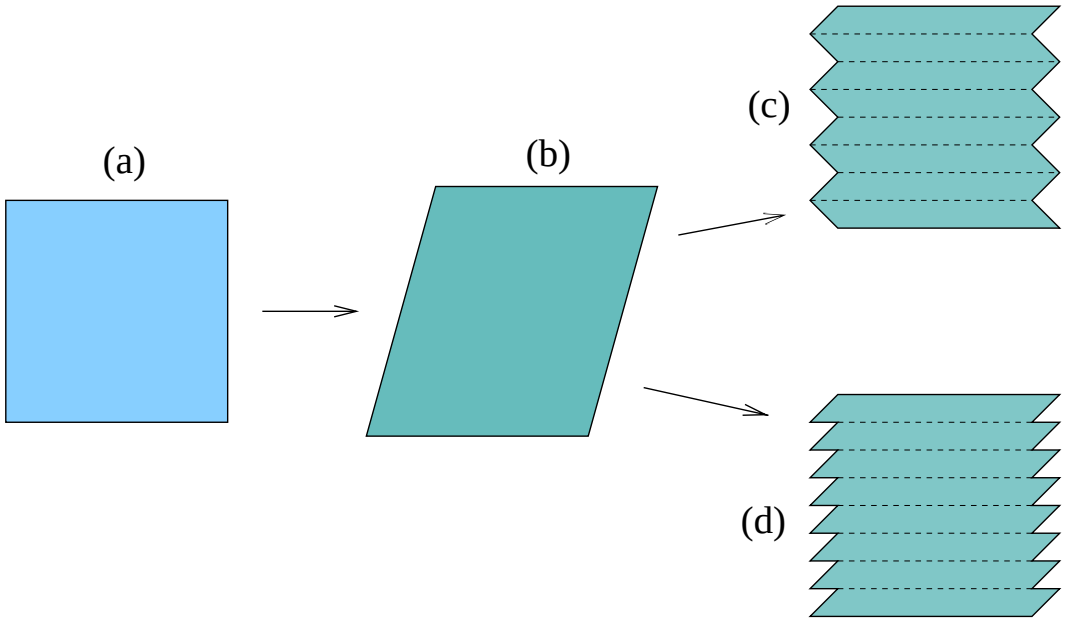

Figure 1.3: (a) Initial austenite structure. (b) Martensite structure which would result from the Bain strain. This is a "wrong" martensite structure which is never observed in experiment. Slips (d) and twins (c) (lattice - invariant transformations) bring the Bain strain in agreement with experiment yielding a correct macroscopic shape and correct structure.

fact, required driving forces can be reduced dramatically if the martensite transformation involves some additional lattice invariant distortion like modulation (Zayak, Entel, Enkovaara, Ayuela *et al.*, 2003c).

Here is a brief summary of the most important features associated of the martensitic transformations:

- Martensitic transformations are (usually) first order, diffusionless, shear (displacive) solid state structural changes.

- Their kinetics and morphology are dictated by the strain energy arising from shear displacements.

- The atoms move in an organised manner relative to their neighbours and therefore they are known as *military* transformations in contrast to diffusional *civilian* transformations.

- The displacements can be described as a combination of a homogeneous lattice deformation known as *Bain distortion* and *shuffles*.

- In a homogeneous lattice deformation one Bravais Lattice is converted to another by the coordinated shift of atoms.

- A shuffle is a coordinated shift of atoms within a unit cell, which may change the crystal lattice but does not produce a homogeneous lattice distortive strain.

1.3 The magnetic shape memory (MSM) effect

The nature of a martensitic transformation is that of a cooperative phenomenon in a solid which can be compared to the occurrence of ferromagnetism. Although the displacement of each atom is not large, the transformation results in a macroscopic change in shape, because all of the atoms in a single structural domain (variant) move in the same direction. As a result the transformation gives rise to unique features like *superelasticity* and the *shape-memory effect* (Otsuka and Kakeshita, 2002). Because of their unique properties, shape-memory materials have been used as so called functional materials for various applications such as couplings, sensors, actuators an so on.

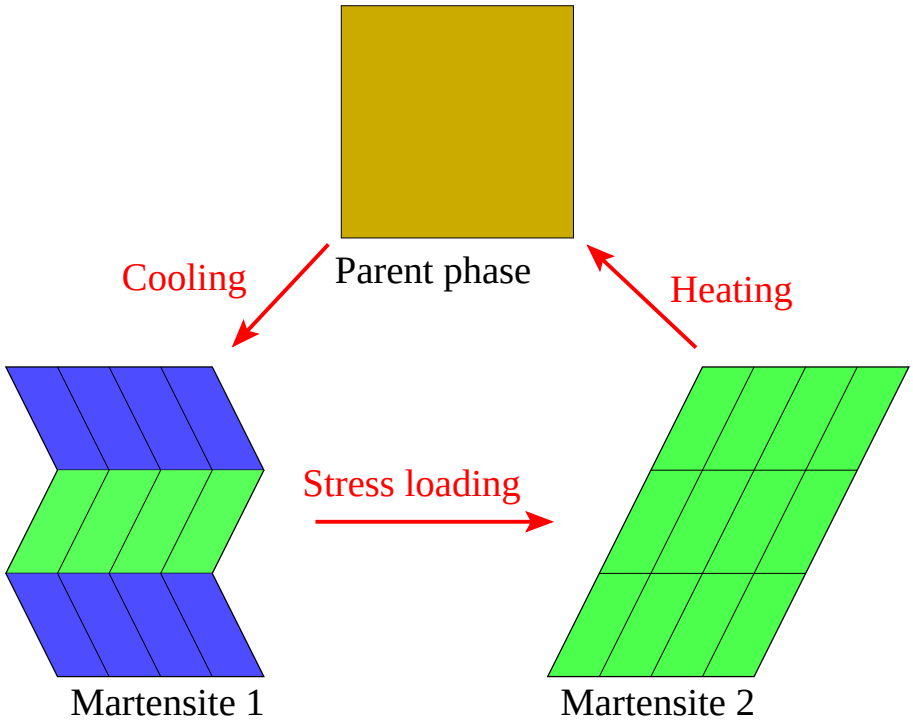

Figure 1.4: Schematic representation of the shape-memory effect. The initial high-temperature structure (austenite) is cooled down so that the structure undergoes a martensitic transformation. In the martensitic phase the macroscopic structure is formed by variants with different orientation when applying pressure to martensite one can obtain any desirable shape of the sample. The flexibility of the sample is due to the motion (redistribution) of the structural domains. Finally, one can return to the initial parent structure by heating the system.

The traditional shape memory effect was originally discovered in a Au-Cd alloy in 1951. It allows to control very large recoverable strokes of materials because of the reversible character of the martensitic transformations (see Fig. 1.4). Later, in 1963, the

effect was also observed in Ti-Ni alloys, which exhibit a prominent shape-memory performance. Research on shape-memory alloys became then more active because of the interest in new *smart materials* (used as sensors and actuators). There is a huge demand for these technologies because they promise to be very economical in use. For practical applications it would mean that some very complicated electro-mechanical device can be replaced by small and cheap crystals, which consume less energy and can work for a very long time being simple for routine maintenance. It turns out that in electro-mechanical devices the ordinary shape-memory process is not really applicable. The necessary cooling and heating are rather slow processes and require for additional complicated devices. There is still a lot of applications in connection with the temperature-pressure controlled shape-memory effect, but it is very much desirable to control the shape-memory effect by other means.

Very recently, a new kind of materials called *magnetic-shape-memory materials* have been found to be very promising for technological applications of smart materials. A unique feature of these materials is that the two cooperative phenomena, martensite and ferromagnetism, co-exist and interact. It has been suggested first that one can realise a magnetically controlled shape-memory effect similar to that driven through cooling and heating (see Fig. 1.4). Namely, by applying an external magnetic field one can induce the martensitic transformation. In other words, the magnetic field will shift the martensitic transition temperature up or down, depending on the concrete system. This possibility was studied for the case of Ni_2MnGa - based alloys by Bozhko *et al.* (1999).

However, there is another way to realise the magnetic-shape-memory (MSM) effect. It was discovered just recently (1995-96) that in the martensitic phase, the structural domains (martensitic variants) can be forced to rearrange themselves under applied external magnetic field (Ullakko, Huang, Kantner, O'Handley *et al.*, 1996; Ullakko, Sozinov and Yakovenko, 2000). This effect has led to a completely new class of actuator and sensor devices (Aaltio and Ullakko, 2000; Wei and G.Engdahl, 2000). Compared to the ordinary (temperature driven) shape-memory effect the magnetic control offers faster response, compared to heating and especially cooling. Also the maximum deformation achievable by MSM alloys is much larger than in the ordinary magnetostrictive materials (like Terfenol-D). Presently for the case of off-stoichiometric Ni_2MnGa giant field-induced strains up to 5% can be obtained in moderate magnetic fields (3-4 kOe) at room temperature[1].

The magnetically controlled twin structure is a remarkable achievement of material science. Developments in this area of research contribute to the general knowledge about martensite, which has been a matter of research for more then a century. Now, these magnetic properties of martensite open new prospects towards more sophisticated applications, like magnetically-controlled micro-instruments. The MSM materials will lead to a change of mechanical engineering design allowing to simplify the mechanical constructions. The potential MSM applications can include devices for fluid control as valves, pumps, mechanical couplers, positioning devices for robots and manipulators, devices for active vibration damping etc.

[1] Very recent works report strains in Ni_2MnGa up to 10% (Enkovaara, 2003)

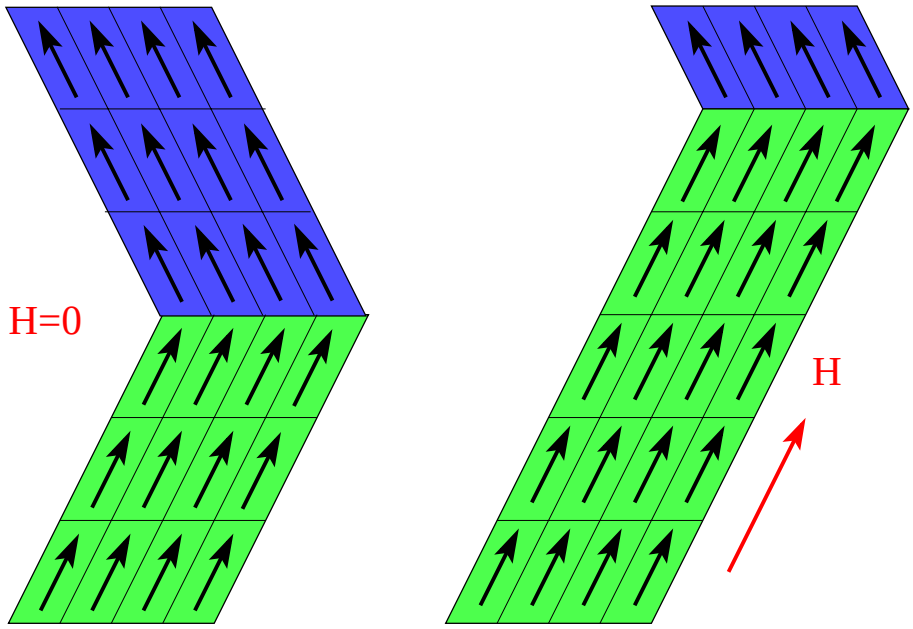

Figure 1.5: Schematic representation of the magnetic-field-induced redistribution of the martensitic domains. Those domains which benefit from the applied field will dominate in the sample leading to a macroscopic deformation up to 10 % (Enkovaara, 2003)

The MSM is an entirely material dependent technology and enormous efforts are made to find optimal MSM materials. Presently, several systems are known which include Ni_2MnGa, Co_2MnGa, FePt, CoNi and FeNiCoTi (Ullakko, Huang, Kantner, O'Handley *et al.*, 1996). Nowadays calculations on the basis of density functional theory will help to predict the properties of new MSM materials. In general, as summarized by Enkovaara (2003), the MSM materials must possess the following properties:

- It should be (ferro)magnetic and exhibit the martensitic transformation.
- The magnetic anisotropy energy must be larger than the energy needed to move the twin boundaries.
- It should be in the martensitic phase at room temperature.
- The magnetic moment should be large enough since the required external field depends on it.

To date, the most promising MSM materials belong to the family of Ni-Mn-Ga alloys which has initiated many experimental and theoretical works in the recent years [2].

[2] A brief summary of these works and an interesting introduction to the subject of the MSM technology can be found in the PhD thesis of Jussi Enkovaara from the Laboratory of Physics of the Helsinki University of Technology

1.4 Computer simulations on the atomistic scale

The development of computers during the last decades has led to remarkable achievements in solid state theory as well as in other areas of natural science. In 1953 Metropolis demonstrated that a classical problem of N particles can be solved by means of the Monte-Carlo methods using computers (Metropolis, Rosenbluth, Rosenbluth, A *et al.*, 1953). Much more sophisticated Monte-Carlo methods have been developed since that time. They are used to solve a wide range of models describing magnetic order, structural transformations, different kinds of kinetics, etc. Not long after the work of Metropolis, first works on molecular-dynamics simulations appeared (Alder and Wainwright, 1957; Wood and Jacobsen, 1957). In this method, the classical equations of motion are solved for each particle of the system using appropriate numerical procedures. The simplicity of this method allows to simulate very big systems with realistic interatomic potentials. The more realistic the potentials are, the better comparison with experiment can be achieved and more physical properties can be predicted. Molecular-dynamics methods can be very effective when using semi-empirical model potentials which take into account electronic structure features of the materials. Recent simulations with *Embedded-Atom Method* allowed to model realistic transformation phenomena on the system of about 1,000,000 atoms (Kadau, Germann, Lomdahl and Holian, 2002).

The increasing computational capabilities encourage development of new electronic structure methods. *Ab-initio* methods have become of ultimate importance in modern solid state physics. *Ab-initio* means to perform the calculations of the properties of a system from first principles with no parametrisation. The main goal of these methods is to solve the Schrödinger equation very accurately, that is in principle a perfect approach in order to obtaining any desired information on the system under study. However, one has to invoke various approximations in order to solve this problem. Among many successful approximate approaches which allow to solve the *ab-initio* problem, Hartree-Fock and Density-Functional based methods form the basis for almost all current electronic-structure methods. Presently, *ab-initio* calculations allow to simulate systems of the order of 100 atoms. Of course, there exist other methods which utilise more rough approximations and are not really *ab-initio*, but allow to simulate systems of about 1000 atoms with required precision. A systematic overview of these methods can be found in (Springborg, 2000).

1.5 Objectives of this work

Objective of this work is to understand the stability of the different crystal structures observed experimentally for the Ni_2MnGa compound. This fundamental theoretical challenge arises from the application needs, where Ni_2MnGa is currently used. Namely, crystals of Ni_2MnGa are intended to work as effective micro-machines (so-called) actuators (MSM technology). This work is concentrated on the microscopic properties of a single variant (structural domain) of martensite, rather than on the whole martensitic structure of Ni_2MnGa. Apart from the fact that martensite can form complicated pat-

terns of domains, a single domain of Ni_2MnGa can exist in different structural states. Depending on the structure of a single martensitic domain, the whole martensite correspondingly exhibits different magneto-mechanical properties. Magnetization, magnetic anisotropy energy, mobility of magnetic and structural domain walls are dictated by the electronic structure of a single unit cell. This problem is a big challenge, part of which is studied in this thesis. It is important to investigate the tendencies which are responsible for the stability of the different structural phases. Such a study will help to understand physics of martensitic nucleation.

The work has been carried out on the atomic scale using state-of-the-art electronic structure simulation methods. In case of Ni_2MnGa problem one has to account for extremely small energy scales requiring for a hyghly accurate method. Therefore the basic calculations were done by using one of the most sophisticated implementations of the pseudo-potential and projector-augmented-wave methods as in the *Vienna Ab-initio Simulation Package* (VASP). Test calculations showed that these methods produce reliable results comparable with previous calculation reported in the literature. The role of atomic modulations in the formation of the martensitic structures is studied in the second part of this work. There exist an experimentally constrained model for this kind of structure. So far, no modulation has been ever taken into account in previous *ab-initio* calculations. The main numerical problem arises from the fact that only a relatively large supercell can accomodate this kind of deformation. However, it was possible to perform the necessary calculations and to investigate the stable structure corresponding to the martensitic ground state of Ni_2MnGa. The third part of this work is devoted to the investication of the dynamical properties of Ni_2MnGa. Phonon calculations are performed in order to evaluate the influence of lattice vibrations on the formation of the precursor structures in Ni_2MnGa and on the formation of the different martensites. The last part of the work describes investigation of an off-stoichiometric system of Ni-Mn-Ga. This is a necessary extension of the thesis because the experimentally investigated structures are usually off-stoichiometric and contain defects.

2 Experimental background

2.1 Crystal structures and phase transformations

Ni_2MnGa is ferromagnetic at room temperature ($T_c \approx 380$ K) and exists in a highly ordered (98% order) Heusler, $L2_1$ type, structure (see Figure 1.1) (Webster, Ziebeck, Town and Peak, 1984). This structure may conveniently be considered as four interpenetrating fcc sublattices with atoms of Ga, Mn, Ni and Ni at locations $(0,0,0)$, $\left(\frac{1}{2},\frac{1}{2},\frac{1}{2}\right)$, $\left(\frac{1}{4},\frac{1}{4},\frac{1}{4}\right)$, $\left(\frac{3}{4},\frac{3}{4},\frac{3}{4}\right)$, respectively. The experimental lattice parameter is 5.825 Å, giving an fcc unit cell volume of 198 $Å^3$.

On cooling below 202 K, Ni_2MnGa undergoes a martensitic phase transformation to a tetragonal bct structure with $c/a < 1$ (see Fig. 2.1). X-ray powder diffraction measurements suggest that the lattice of the mean tetragonal structure is given by $c = 5.566$ Å, $a = 5.920$ Å and $c/a = 0.94$ (Webster, Ziebeck, Town and Peak, 1984). However, additionaly, the X-ray spectra show, among the main peaks related to the tetragonal structure, several weaker peaks with only 3% of the main peaks size. It was assumed that the additional peaks are associated with a superstructure having a long periodicity. Further analysis of the additional reflection peaks and diffraction angles shows the existence of a periodical shuffling of atoms (modulation) along the $[1\bar{1}0]$ direction. The modulation is formed in such a way that each 5-th (110) plane remains in its original position (Martynov and Kokorin, 1992). One period of the modulation is accommodated in 5 (110) planes (2.5 lattice spacings of the bct structure) which implies a wave vector for the modulation $q/q_{max} = 0.4$. In the literature, this modulated martensitic tetragonal structure is called 5M (Zayak, Entel, Enkovaara, Ayuela *et al.*, 2003c).

A model for the 5M structure was first proposed by V. V. Martynov and V. V. Kokorin (Martynov and Kokorin, 1992). It is shown schematicaly in Fig. 2.2. The modulation is nothing else but a static wave of atomic displacements with polarization in $[1\bar{1}0]$ and propagation in [110] directions with respect to the $L2_1$ lattice. This kind of periodic shuffling is known to occur in other crystals as well, for instance, the so a called 9R structure in Li (Gooding and Krumhansl, 1988). R. J. Gooding and J. A. Krumhansl presented a Landau theory for the martensitic phase transfromation from the high-temperature cubic phase to the long-period tetragonal 9R structure. This theory had also been applied to the case of Ni_2MnGa by taking into account the magneto-elastic coupling and an external magnetic field (Buchelnikov, Zayak, Vasil'ev, Dalidovich *et al.*, 2001a; Zayak, Buchelnikov and Entel, 2002). In this context, it is important to note, that the orriginal model proposed by V. V. Martynov and V. V. Kokorin had to be corrected after more accurate measurements. Instead of the suggested modulation wave vector $q/q_{max} = 0.4$, the 5M structure has to described by an incommensurate modulation with corresponding wave vector $q/q_{max} = 0.433$ (Zheludev, Shapiro, Wochner and Tanner, 1996).

As a matter of fact, the 5M structure is not the only martensitic structure found in Ni_2MnGa at low temperatures. It had been reported that there can be two more different structures induced by stress. One of them is an orthorhombic-like structure

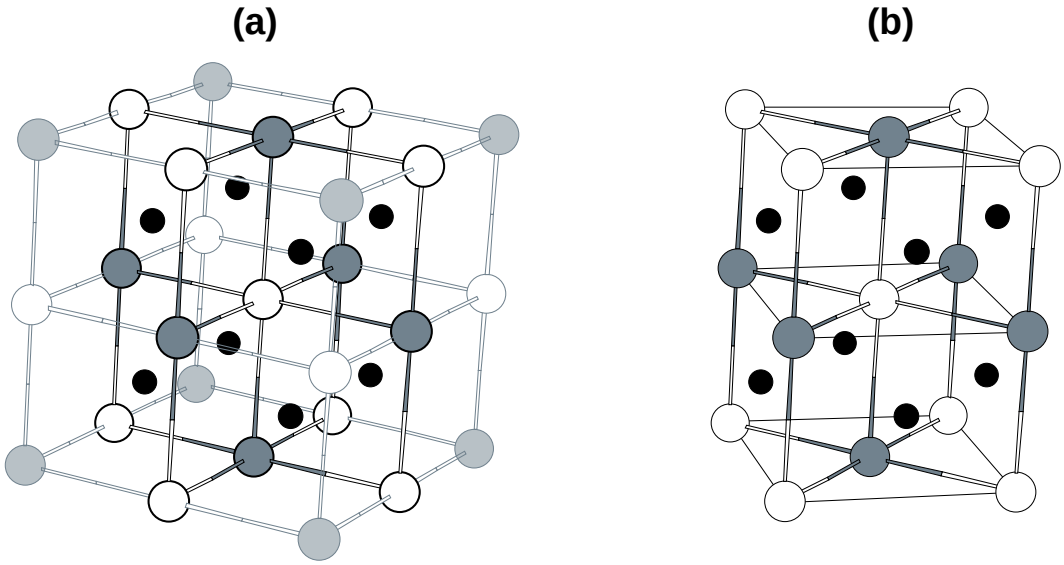

Figure 2.1: Relation between the $L2_1$ and the bct structures of Ni_2MnGa. White, gray and black circles show the positions the of Mn, Ga and Ni atoms, respectively.

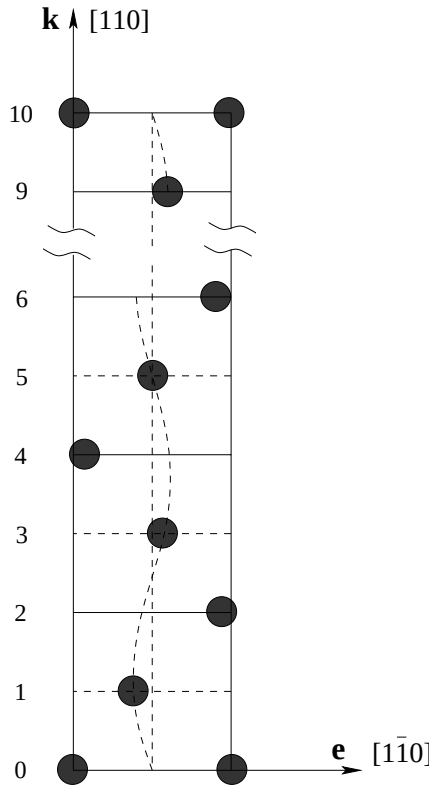

Figure 2.2: Schematic projection of the 5-layer modulated structure (5M in Table 2.1) onto the (010) plane (Martynov and Kokorin, 1992).

Table 2.1: Lattice parameters of the Ni_2MnGa crystal structures (Martynov and Kokorin, 1992); q vectors are in units of $[110](2\pi/a)$ (Zheludev, Shapiro, Wochner and Tanner, 1996). In case of the 7M structure one would expect the modulation with a wave vector $q = 2/7 \approx 0.28$, but there is no experimental evidence for this value to date.

	Lattice parameters (Å)				
Structure	$L2_1$	3M	5M	7M	T
a	5.824	5.824	5.90	6.12	6.44
b	5.824	5.824	5.90	5.78	5.52
c	5.824	5.824	5.54	5.54	5.52
Modulation	none	$q \approx 0.33$	$q \approx 0.43$	...	none
Tetragonality	1	1	0.94	-	≈ 1.2

with a shuffling of atoms similar to that of the 5M structure, but with a longer period (Martynov and Kokorin, 1992). This new structure is called 7M according to the lenght of its period, which is confined to 7 lattice spacings. However, one should not expect a wave number of 1/7 for the 7M structure. In reality, the modulation can be more complicated then a simple sine-like wave. It can be a combination of several harmonics as it was suggested by P. J. Brown *et al.* (Brown, Crangle, Kanomata, Matsumoto *et al.*, 2002). Another experimentally observed structure is tetragonal (bct), which does not show any modulation and has tetragonality ratio of $c/a > 1$. Table 2.1 gives a summary of the structures found for Ni_2MnGa (Brown, Crangle, Kanomata, Matsumoto *et al.*, 2002; Martynov and Kokorin, 1992; Webster, Ziebeck, Town and Peak, 1984). The 3M structure presented in Table 2.1 will be described below in section "Precursor phenomena" because of its particular importance.

2.2 Magnetic properties

Ni_2MnGa is ferromagnetic at room temperature ($T_c \approx 380$ K), i.e. well above the temperatures for which the structural transformations take place. Figure 2.3 shows the experimentally obtained temperature dependence of the total magnetization of Ni_2MnGa for several values of an applied external magnetic fields. One can see a substantially different behaviour of the magnetization in the high temperature $L2_1$ structure compared to the low temperature martensite. This difference is due to the structural domains of martensite called twin variants, which contain the magnetic domains. Magnetostriction leads to easy magnetization directions consistent with directions of the homogeneous deformations of the martensite variants (O'Handley, 1998). Only strong magnetic fiels are able to overtake the effect of structural domains on the magnetization. In terms of the Landau theory, the Zeemann term becomes larger than the magnetostriction term (L'vov, Gomonaj and Chernenko, 1998).

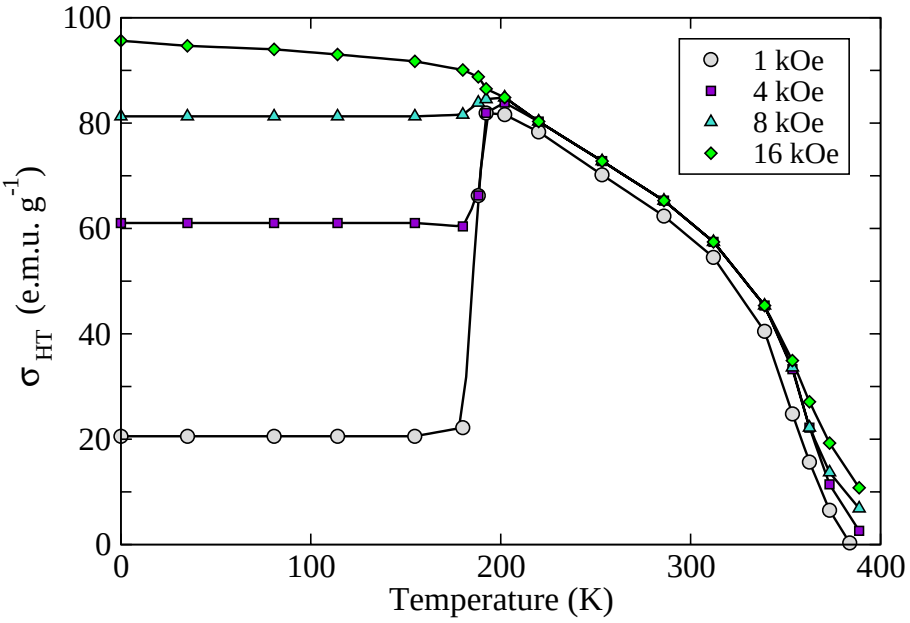

Figure 2.3: The magnetization of Ni_2MnGa as a function of temperature for different external magnetic fields. The low temperature part shows how the structural martensitic domains (variants) affect the value of the macroscpic magnetization. The Figure is was taken from the work of P. J. Webster *et al.* (Webster, Ziebeck, Town and Peak, 1984).

Figure 2.5 and Figure 2.4 show the calculated electronic density of states of Ni_2MnGa in the $L2_1$ structure. These Figures are consistent with the suggestion of J. Kübler *et al.* concerning the formation and coupling of magnetic moments in the Heusler alloys (Kübler, Williams and Sommers, 1983). It was stated that Heusler alloys can be considered to be ideal local-moment systems. The localized character of the magnetization results from the exclusion of minority-spin electrons from the Mn $3d$ states. The Ga atoms have no magnetic moment since the density of states with opposite spin-directions almost coincide (Figure 2.4(Right)), while the Ni atoms have a small magnetic moment.

Known from actual publications values of the magnetic moments in the cubic structure of Ni_2MnGa are: $\mu_{\text{tot}} = 4.09\mu_B$, $\mu_{\text{Ni}} = 0.37\mu_B$, $\mu_{\text{Mn}} = 3.36\mu_B$, $\mu_{\text{Ga}} = -0.04\mu_B$ (Ayuela, Enkovaara, Ullakko and Nieminen, 1999). Summary of the magnetic moments for the $L2_1$ structure will be given below in Table 4.1.

2.3 Precursor phenomena

A specific feature of Ni_2MnGa is that the martensitic transition ($T_{\text{M}} = 202\ K$) is preceded by a weakly first-order premartensitic phase transition (Planes, Obrado, Gonzales-Comas and Ll. Mañosa, 1997). This is known as a precursor phenomenon of the martensitic transformation. Inelastic neutron scattering measurements on Ni_2MnGa showed the existence of a soft $[\zeta\zeta 0]$-TA_2 phonon mode in the parent $L2_1$ structure (see Fig. 2.6) (Fritsch, Kokorin and Kempf, 1994; Kokorin, Chernenko, Pons, Segu *et al.*, 1997; Mañosa Ll.,

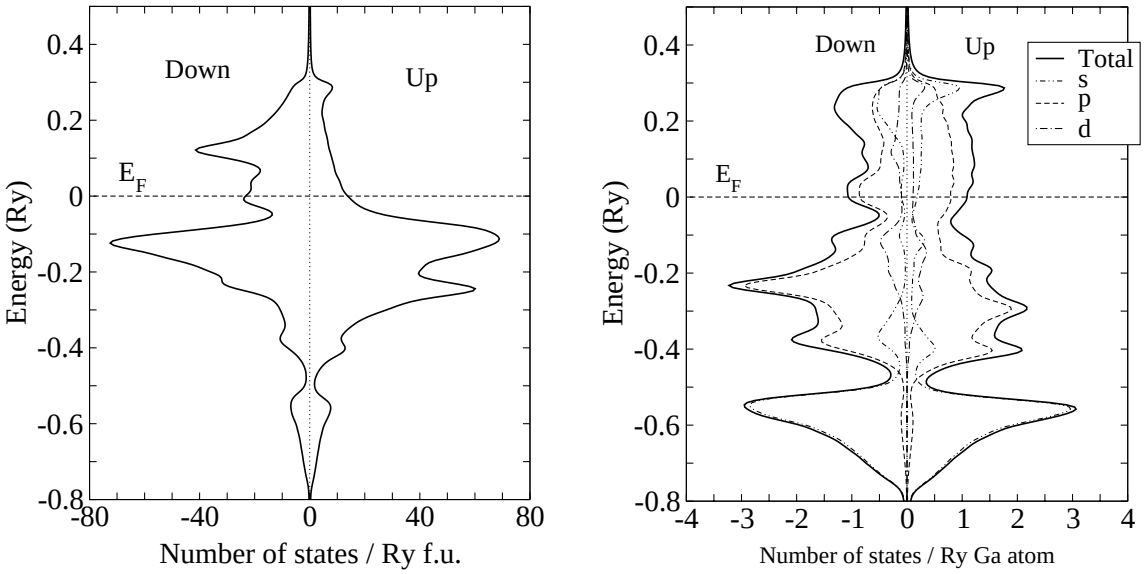

Figure 2.4: The electronic density of states of Ni_2MnGa (left) and the partial contribution of Ga (right) calculated for the $L2_1$ structure.

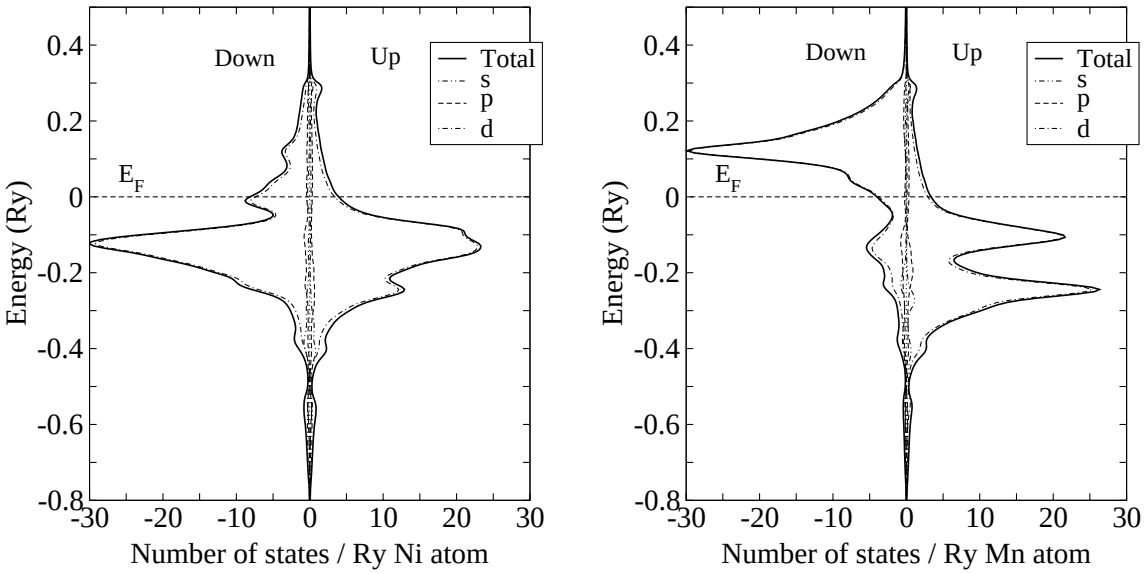

Figure 2.5: The partial electronic density of states of Ni (left) and Mn (right) calculated for the $L2_1$ structure of Ni_2MnGa

Gonzalez-Comas, Obrado, Planes *et al.*, 1997; Mañosa Lluis, Planes, Zarestky, Lograsso *et al.*, 2001; Stuhr, Vorderwisch, Kokorin and Lindgard, 1997; Zheludev, Shapiro, Wochner and Tanner, 1996). It is known that the martensitic transformations are often associated with phonon anomalies in the parent phase (Zhao and Harmon, 1992). However, in case of Ni_2MnGa, the TA_2 phonon mode condenses at a wave vector of $\zeta_0 = 0.33$, well above the martensitic transition temperature, $T_P = 260\ K$ (Zheludev, Shapiro, Wochner, Schwartz *et al.*, 1995; Zheludev, Shapiro, Wochner and Tanner, 1996). Under further cooling from T_P to T_M, the frequency of the soft mode increases. This means that the phonon softening is associated with the premartensitic phase transition rather than with the martensitic transformation (Khovailo, Takagi, Bozhko, Matsumoto *et al.*, 2001). The premartensitic structural transformation gives rise to a commensurate periodic distortion of the parent phase with a propagation vector equal to that of the soft mode, $q = \frac{1}{3}(2\pi/a)$. This corresponds to a static wave with a period, which is accommodated in six atomic planes or three lattice spacings. An attempt to define this structure experimentally was recently done by means of high resolution neutron powder diffraction and single-crystal measurements (Brown, Crangle, Kanomata, Matsumoto *et al.*, 2002). However, in this kind of structural analysis one has to rely on a fit of diffraction data, but the fit itself is a matter of guess. It is possible to fit the same data with different parameters.

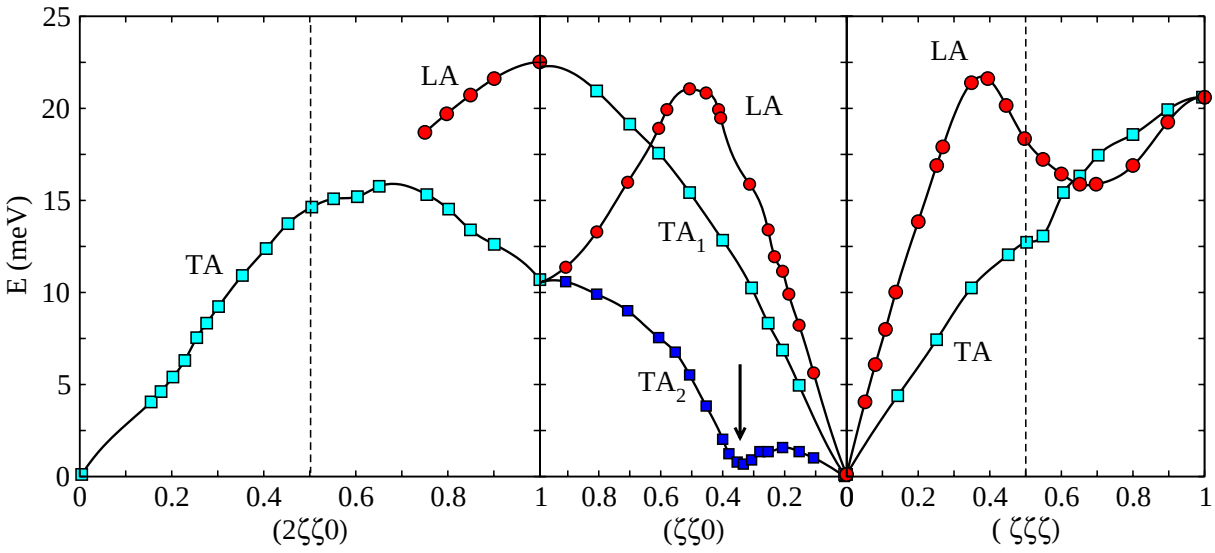

Figure 2.6: Experimental acoustic-phonon curves for the cubic $L2_1$ phase of Ni_2MnGa obtained from inelastic neutron scattering. This Figure was taken from the work of A. Zheludev *et al.* (Zheludev, Shapiro, Wochner and Tanner, 1996).

The premartensitic transformation in Ni_2MnGa has been a matter of wide discussions. Both structural and magnetic changes are involved here, but still there is no understanding of the origin of this precursor phenomenon. Ultrasonic measurements show an anomalous behaviour of elastic constants C_{44}, $C' = 1/2(C_{11} - C_{12})$ and $C_L = 1/2(C_{11} + C_{12} + 2C_{44})$ at T_P and not at T_M (Stenger and Trivisonno, 1998; Worgull, Petti and Trivisonno, 1996). At the same time, it was shown that the premartensitic transition

temperature, T_P, depends on the external magnetic field (Zuo, Su and Wu, 1998). A. Planes *et al.* suggested that the magnetoelastic coupling between the magnetization and the lattice vibrations enables the can lead to the premartensitic transformation (Planes, Obrado, Gonzales-Comas and Ll. Mañosa, 1997). It has been argued that the microscopic origin lies in the electron-phonon coupling and specific nesting properties of the Fermi surface (Zheludev, Shapiro, Wochner and Tanner, 1996). Similar arguments were used to explain phonon anomalies related to the martensitic transformation in Ni-Al alloys (Zhao and Harmon, 1992). However, no premartensitic phenomena has been reported to occur in Ni-Al. As a matter of fact, the ferromagnetic character of Ni_2MnGa is the main difference between these two alloys (Planes, Obrado, Gonzales-Comas and Ll. Mañosa, 1997). From this basis one has tried to model the premartensitic transition being driven by the magneto-elastic interaction (Castan, Vives and Lindgard, 1999). The idea of a magneto-elastic coupling as an origin for the precursor is supported by measurements of the temperature dependence of the magnetization in Ni_2MnGa. The measurements revealed a pronounced dip in magnetization at T_P (Khovailo, Takagi, Bozhko, Matsumoto *et al.*, 2001). At the same time, in contrast to the just mentioned results, experimental studies of spin waves and phonon anomalies in Ni_2MnGa showed that the magnons exhibit no anisotropy in the low-energy range where one would expect the coupling to phonons to play a role. Thus, the premartensitic transition is still under debate, and many aspects have to be investigated further before a comprehensive understanding will be achieved.

2.4 Non-stoichiometric alloys based on Ni_2MnGa

As a matter of fact, the stoichiometric compound Ni_2MnGa serves as a reference system for all practical studies and applications. The real practical interest is focused on different non-stoichiometric alloys based on Ni_2MnGa, which are, however, very close to the stoichiometric composition. Figure 2.7 presents a corresponding ternary phase diagram for the Ni-Mn-Ga alloys, which have been reported in the most recent publications. Depending on the composition, certain important properties of Ni-Mn-Ga change considerably. One of the important characteristic parameters is the number of valence electrons per atom, e/a. There is a number of empirical investigations which consider the value of saturation magnetization, martensitic start temperature, Curie temperature as a function of e/a (Jin, Marioni, Bono, Allen *et al.*, 2002; Mañosa Ll., Gonzalez-Comas, Obrado and Planes, 1999; Murray, Farinelli, Kantner, Huang *et al.*, 1998; Schlagel, Wu, Zhang and Lograsso, 2000; Takeuchi, Famodu, Read, Aronova *et al.*, 2003). It has been shown that the excess of Ni in the formula $Ni_{2+x}Mn_{1-\mathrm{x}}Ga$ reduces the Curie temperature and simultaneously increases the martensitic transition temperature so that at $X \approx 0.2$ they coinside, $T_\mathrm{C} = T_\mathrm{M}$. It has been found that these two transition temperatures coincide for a certain range of the composition parameter x. It is believed that in case when the Curie temperature is equal to the martensitic start temerature, some specific effect might be expected due to the magnetoelastic coupling (Bozhko, Vasil'ev, Khovailo, Dikshtein *et al.*, 1999; Vasil'ev, Bozhko, Khovailo, Dikshtein *et al.*, 1999a,b). Figure 2.8 shows an experimental temperature-composition phase diagram for $Ni_{2+x}Mn_{1-\mathrm{x}}Ga$. This diagram

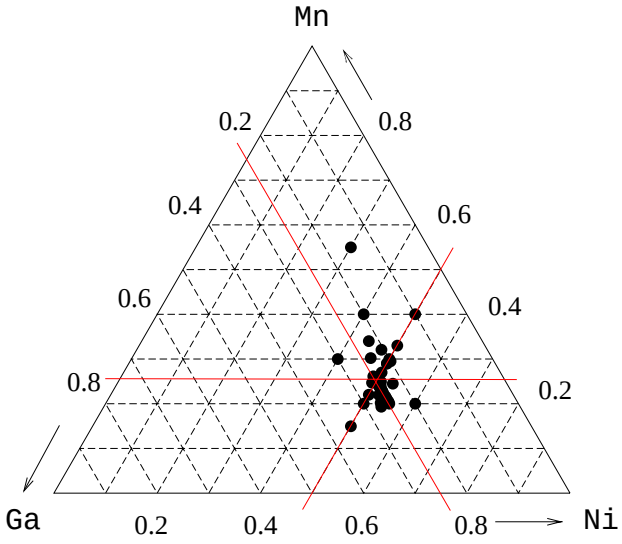

Figure 2.7: Experimental ternary diagram of Ni-Mn-Ga alloys. The black dots mark the compositions, which were widely studied. (Buchelnikov, Zayak, Vasil'ev, Dalidovich *et al.*, 2001a; Cesari, Chernenko, Kokorin, Pons *et al.*, 1997; Chernenko, 1999; Gonzalez-Comas, Obrado, Mañosa, Planes *et al.*, 1999; Khovailo, Takagi, Bozhko, Matsumoto *et al.*, 2001; Mañosa Lluis, Planes, Zarestky, Lograsso *et al.*, 2001; Murray, Farinelli, Kantner, Huang *et al.*, 1998; Overholser, Wutting and Neumann, 1999; Schlagel, Wu, Zhang and Lograsso, 2000; Tickle and James, 1999; Vasil'ev, Bozhko, Khovailo, Dikshtein *et al.*, 1999a; Wu, Yu, Meng, Chen *et al.*, 1999).

shows a compositional dependence of the Curie temperature, martensitic and premartensitic phase transitions. A significant observation is that the premartensitic transition does not depend on the composition, and is suppessed by the martenstic transition when x increases. This can be clearly seen from the measured temperature-composition dependence of the electrical resistivity by Khovailo *et al.* (2001) in $Ni_{2+x}Mn_{1-x}Ga$ for $0 < x < 0.9$. Remarkable is that a prominent anomaly of the resistivity at the premartensitic transition has been observed, which disappears together with the premartensitic transition for $x > 0.9$. Some *ab-initio* studies of the role of non-stoichiometry appeared recently (MacLaren, 2002).

2.5 Previous theoretical investigations of Ni_2MnGa

2.5.1 *Ab-initio* calculations

A number of theoretical works on Ni_2MnGa (including *ab-initio* calculations) were published during the last few years. It was shown that basic structural and magnetic properties of the cubic $L2_1$ structure can be reproduced in the calculations with fairly high aquracy (Ayuela, Enkovaara, Ullakko and Nieminen, 1999). Both lattice parameters and magnetic moments have been obtained in agreement with experimental data. Volume and tetragonality optimization enabled to obtain two stable structures: the $L2_1$and the tetragonal structure T (see Table 2.1). Similar calculations have been done for different Heusler alloys which allowed to trace to some extent chemical trends for lattice parameters and magnetic moments (Ayuela, Enkovaara, Ullakko and Nieminen, 1999). Band structure and generalized susceptibility $\chi(\mathbf{q})$ calculations showed the existance of anomalie in the electronic structure, like the susceptibility peaks along the [110] direction (Velikokhatnyi and Naumov, 1999). One of the peaks was found at the wave vector $q/q_{max} \approx 0.42$, which

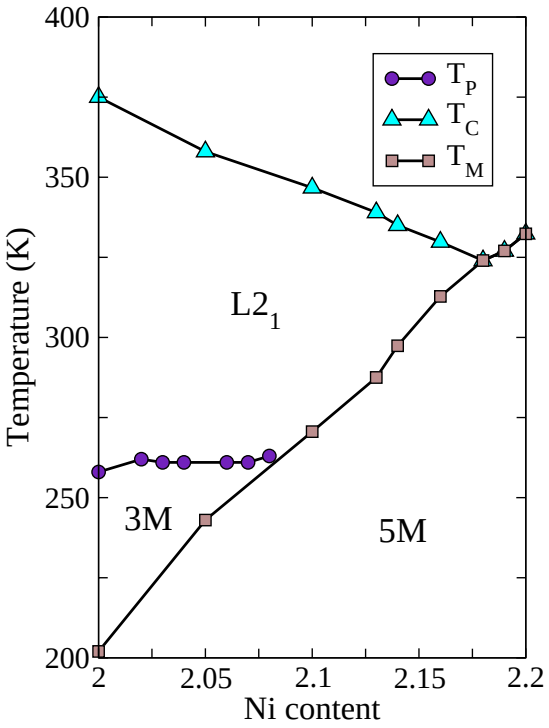

Figure 2.8: Phase diagram for $Ni_{2+x}Mn_{1-x}Ga$ in the (T-X) plane. The data are taken from (Bozhko, Vasil'ev, Khovailo, Dikshtein *et al.*, 1999; Khovailo, Takagi, Bozhko, Matsumoto *et al.*, 2001; Vasil'ev, Bozhko, Khovailo, Dikshtein *et al.*, 1999a).

is practically coincides with the wave vector $q/q_{max} \approx 0.433$ characterizing the lattice modulation of the 5M structure. Analysis of the calculated Fermi surface revealed a nesting vector of the same length, which suggests that the nesting is part of the origin of the modulation in Ni_2MnGa (Lee, Rhee and Harmon, 2002; Velikokhatnyi and Naumov, 1999). Many discussions and efforts have been required to meet agreement of the calculations with experimental data. In particular, it was important for the 5M structure, which is now believed to be martensitic ground state of Ni_2MnGa. A certain success has been achieved by using an extremely high accuracy *ab-initio* full-potential-linear-augmented-plane-wave (FLAPW) calculations (Ayuela, Enkovaara and Nieminen, 2002). These calculations showed, that despite the fact that sufficiently low energy minimum at $c/a = 0.94$ cannot be obtained for a perfect structure of Ni_2MnGa, there is a clear tendency of the structure to show an anomaly at $c/a = 0.94$. A comparizon of the structures with $c/a = 1$ and $c/a = 0.94$ allows to estimate some termal properties related to the martensitic transformation (Enkovaara, Ayuela, Nordström and Nieminen, 2002b). A good agreement with experimental data has been achieved when calculationg the magnetic anisotropy energy for Ni_2MnGa (Enkovaara, Ayuela, Nordström and Nieminen, 2002a). It is important to note that hypothetic non-collinear spin configurations for Ni_2MnGa have been studied as well (Enkovaara, Ayuela, Jalkanen, Nordström *et al.*, 2003a). In addition, a very good *ab-initio* study of magnetic shape-memory alloys, which includes many useful references, was undertaken by Enkovaara (2003).

2.5.2 Model calculations for Ni_2MnGa

There is a number of works in which the properties of Ni_2MnGa (and its alloys) were studied using model calculations. In one of the works a simple model of Ni_2MnGa with a clear physical interpretation was solved by using mean-field and Monte-Carlo simulations (Castan, Vives and Lindgard, 1999). The model considered by Castan *et al.* (1999) includes both magnetic and structural order parameters with a special emphasis on the role of magnetoelastic coupling. Both mean-field and Monte-Carlo simulations allowed to obtain qualitative phase diagrams for Ni_2MnGa allowing to identify the paramagnetic cubic, ferromagnetic cubic, ferromagnetic intermediate (premartensitic), and ferromagnetic martensitic phases. The main point of this study is that the magnetoelastic coupling term can be responsible for the premartensitic phase transition. It was argued that the strength of the magnetoelastic coupling is sufficient to freeze completely the anomalous phonon mode, which leads to the lattice instability. This has been supported by other studies. For example, a phenomenological model for the intermediate phase transition based on Landau theory was considered by Planes *et al.* (1997). The model includes the magnetoelastic coupling and shows that the interaction between the magnetization and the amplitude of the short wavelength phonons can explain the first order premartensitic transition from the cubic structure to the micromodulated superstructure 3M.

Apart from the models which allow to discuss single monodomain crystals, there are a few studies, which use special models for simulating realistic poly-domain martensitic structures. In particular, one these models allowing to describe ferromagnetism of the inhomogeneous martensitic structure is based on a phenomenological expression for the Helmholtz free energy of a cubic crystal (L'vov, Gomonaj and Chernenko, 1998). The martensitic structure in this case is presented as a periodic structure formed by alternating domains (variants) of the tetragonal phase. The most interesting feature of this model is that is allows to reproduce accurately the temperature-field dependence of the magnetization in Ni_2MnGa shown in Figure 2.3.

Another model was proposed by O'Handley (O'Handley, 1998; O'Handley, Murray, Marioni, Nembach *et al.*, 2000). This phenomenological model is designed to simulate magnetization processes and field-induced macroscopic strain, whereby the latter arises the motion of twin and phase boundaris. Both strong and weak magnetic anisotropy cases have been considered. The idea is that the martensite is presented by different tetragonal domains. The corresponding magnetic easy axes are parallel to the four-fold symmetry axes of the variants. The large macroscopic strain of the sample can be obtained in this case by applying an external magnetic field. The motion of twin boundaries is driven by the force of the Zeeman energy difference, $\Delta\mathbf{MH}$, across the twin boundaries. Those domains which have magnetization along the magnetic field will suppress the domains with magnetization in direction, which is opposite to the field. This model predicts a nearly linear field-dependent strain for moderate magnetic fields (less than a saturation field), which makes a clear distinction with the magnetostriction strain, which is quadratically proportional to the magnetization in moderate fields. A similar model was proposed and applied to simulate colossal magnetostriction of the martensite phase in Ni-Mn-Ga by

Buchel'nikov *et al.* (2001).

With respect to the premartensitic phase transformation and all other aspects related to the modulated shuffling of crystal lattices, a Landau theory developed by Gooding and Krumhansl (1988, 1989) has to be mentioned. These authors presented a complete theoretical study, which allows to describe a first-order transition in a strongly anharmonic systems via coupling of homogeneous strains related to the elastic Zener constant $\frac{1}{2}(C_{11} - C_{12})$ to a modulated distortion driven by a soft acoustic phonon mode.

There are also some works considering a Landau-Ginzburg theory for $Ni_{2+x}Mn_{1-x}Ga$, which include almost all order parameters and types of coupling needed to represent the structural and magnetic properties of this system (Bozhko, Vasil'ev, Khovailo, Dikshtein *et al.*, 1999; Buchelnikov, Zayak, Vasil'ev, Dalidovich *et al.*, 2001a; Buchelnikov, Romanov and Zayak, 1999; Buchelnikov, Vasilev, Zayak and Entel, 2001b; Buchelnikov, Zayak and Entel, 2002; Vasil'ev, Bozhko, Khovailo, Dikshtein *et al.*, 1999a,b; Zayak, Buchelnikov and Entel, 2002). Development and application of this theory is discussed in the Appendix A.

3 Density Functional Theory

Density functional theory (DFT) has long been the main element of electronic structure calculations in solid-state physics, and has also become popular in quantum chemistry and biology. This is because present-day approximate functionals provide a useful balance between accuracy and computational cost, allowing much larger systems to be treated than traditional *ab-initio* methods of quantum chemistry, while retaining much of their accuracy. Nowadays, traditional wavefunction methods, either variational or perturbative, can be applied to find highly accurate results for smaller systems, providing benchmarks for developing density functionals, which can then be applied to much larger systems. DFT is much more than just another way of solving the Schrödinger equation, or of parametrizing empirical results. Density functional theory is a highly efficient method to deal with interacting electron systems. Its methodology is applied in a large variety of fields fo many different problems.

In regular quantum mechanics, for a system of N electrons, using the Born-Oppenheimer approximation, one would have to solve a stationary Schrödinger equation of the form:

$$\left\{ -\frac{1}{2}\sum_{i=1\ldots N}\nabla_i^2 + \frac{1}{2}\sum_{i\neq j}^{N}\frac{1}{|\mathbf{r}_i-\mathbf{r}_j|} + \sum_{i=1\ldots N} V_{ext}(\mathbf{r}_i) \right\} \psi(\mathbf{r_1},\ldots,\mathbf{r_N}) = E\psi(\mathbf{r_1},\ldots,\mathbf{r_N}) \quad (3.1)$$

Here, the atomic units are used, whereby $e = \hbar = m = 1$, energies are in Hartrees 1 H = 27.2114 eV = 627.5 kcal/mol and distances are given in Bohr radii $a_0 = 0.529$ Å. The wavefunction for N electrons is a function of 3N spatial coordinates (and N spin coordinates). Solution of (3.1) is extremely complicated and demanding in case of large systems. Since electrons are coupled by the electrostatic repulsion, it is impossible to split wavefunctions into parts related to separate electrons.

The idea of DFT is to imagine a system of non-interacting electrons. These electrons are subject to a potential $V_S(\mathbf{r})$, chosen in a way to mimic the true electronic system. The subscript S denotes the single-electron treatment. If electrons are non-interacting, their coordinates are decoupled, and their wavefunctions can be constructed from a combination of one-electron wavefunctions, which satisfy the one-electron Schrödinger equation

$$\left\{ -\frac{1}{2}\nabla^2 + V_S(\mathbf{r}) \right\} \phi_i(\mathbf{r}) = \epsilon_i \phi_i(\mathbf{r}). \quad (3.2)$$

In this case one has to solve a 3D equation, as opposite to solving a 3N coordinate equation. This leads to a computationaly much more tractable problem. The problem is how to get a non-interacting system to accurately mimic the interacting system.

3.1 Hartree-Fock

One approach to present the true wavefunction by approximate non-interacting electron orbitals, and then minimize the energy, is given by the Hartree-Fock (HF) equations,

which yield an effective potential of the form

$$V_S^{HF}(\mathbf{r}) = V_{ext}(\mathbf{r}) + \frac{1}{2}\int d^3r' \frac{n(\mathbf{r}')}{|\mathbf{r}-\mathbf{r}'|}. \tag{3.3}$$

The correction to the external potential mimics the effect of coupled electrons, in particular screening the nuclei. Insertion of this potential into the Schrödinger equation yields a potential which depends on the electronic density, which in turn is calculated from the solution for the equation. This is called a self-consistent set of equations. An initial guess must be made for the potential, then the eigenvalue problem is solved, yielding the density and a new potential. These steps are repeated until there is no change in the output from one cycle to the next one - self-consistency has been reached. Such a set of equations are often called self-consistent-field (SCF) equations. Sometimes, the Hartree-Fock method is discussed apart from the traditional DFT. The difference is that HF does not deal with the charge density from the very beginning, instead one has to solve a non-local integro-differential equation for the wave function whose solution allows then to define the electron density. The well-known deficiency of the Hartree-Fock method is connected with the fact that there is no prescription to calculate the correlation energy.

3.2 Thomas-Fermi

Another approach was proposed by L. Thomas and E. Fermi in 1927. It is a semi-classical approach, i.e., certain ideas are borrowed from quantum mechanics, but one deals with ordinary functions instead of quantum mechanical operators. In Thomas-Fermi theory the energy of the system is presented by the non-interacting kinetic energy of a uniform gas plus the Hartree and external energy,

$$E[n] = A_S \int d^3r\, n^{5/3}(\mathbf{r}) + \int d^3r\, V_{ext}(\mathbf{r})\, n(\mathbf{r}) + \frac{1}{2}\int d^3r \int d^3r' \, \frac{n(\mathbf{r})n(\mathbf{r}')}{|\mathbf{r}-\mathbf{r}'|}. \tag{3.4}$$

It is important to note that this expression was developed for a non-spin-polarized system, i.e., with equal numbers of spin up and down electrons in a spin-independent external potential. The coefficient A_S is chosen so that agreement with a uniform electronic gas is achieved, yielding $A_S = (3/10)(3\pi^2)^{2/3}$. This also means that the most serious problem of the Thomas-Fermi approach is an unsufficiently accurate treatment of the kinetic energy. It was shown that this theory cannot be improved systematically. More sophisticated approaches are based on the Kohn-Sham equations.

3.3 Hohenberg-Kohn theorems

The external potential determines in principle all properties of the quantum mechanical system. The first Hohenberg-Kohn theorem shows that the density may be used in place of the wave functions or potential as the basic function uniquely characterizing the system or, more rigorously: the ground-state density $n(\mathbf{r})$ uniguely determines the potential up

to an arbitrary constant. A compact form of the theorem can be formulated in terms of all wavefunctions which lead a certain density $n(\mathbf{r})$ defining a functional:

$$F[n] = \min_{\Psi \to n} \langle \Psi | \hat{T} + \hat{V}_{ee} | \Psi \rangle, \tag{3.5}$$

where the search is over all wavefunctions yielding $n(\mathbf{r})$. Then, for any $n(\mathbf{r})$, any wavefunction minimizing F is a ground-state wavefunction, since the ground-state energy is simply obtained from the variational principle,

$$E = \min_{n} \left(F[n] + \int d^3 r V_{ext}(\mathbf{r}) n(\mathbf{r}) \right) \tag{3.6}$$

where the search is over all normalized positive densities. Such a wavefunction can then be used to constrain the unique corresponding potential.

The second Hohenberg-Kohn theorem states that the functional $F[n]$ is universal, i.e., it is the same for all electronic structure problems. And the last part of the Hohenberg-Kohn theorem is the Euler-Lagrange equation for the energy. One needs to minimize $E[n]$ for a given $V_{ext}(\mathbf{r})$ keeping the particle number fixed. One therefore minimizes $E[n] - \mu N$, which gives the Euler-Lagrange equation,

$$\frac{\delta F}{\delta n(\mathbf{r})} + V_{ext}(\mathbf{r}) = \mu. \tag{3.7}$$

Here μ is the chemical potential of the system, $\mu = \partial E / \partial N$. The exact density is such that it makes the functional derivative of F to be exactly equal to the negative of the external potential (up to a constant). The crutial point is find an adequate approximation for F so that it allows to solve Eq. (3.7). This yields a single integro-differential equatin to be solved by a self-consistent procedure for the density, which in turn can be normalized and inserted back into the fuctional $E[n]$ in order to recover the ground-state energy. The Thomas-Fermi theory, discussed above, presents a crude attempt to do this, but its accuracy is insufficient for modern material science.

3.4 Kohn-Sham equation

The basic steps to perform a "Kohn-Sham calculation" are very much the same as in Thomas-Fermi theory, but the logic behind is entirely different. Let us consider a system of non-interacting electrons, which have precisely the same density $n(\mathbf{r})$ as the real physical system. This we denote as the "Kohn-Sham system". Using DFT methods, one can derive its potential $V_S(\mathbf{r})$ provided that one knows dependence of the total energy E on the density. The main feature of the Kohn-Sham method is that the non-interacting kinetic energy is treated exactly, which includes almost all of the true kinetic energy.

When deriving the Kohn-Sham equation one has to recall that the orbitals of the non-interacting electrons are given by Eq. (3.2) and yield

$$n(\mathbf{r}) = \sum_{i=1}^{N} |\phi_i|^2. \tag{3.8}$$

The corresponding Euler equation is

$$\frac{\delta T_S}{\delta n(\mathbf{r})} + V_S(\mathbf{r}) = \mu, \tag{3.9}$$

where

$$T_S[n] = \min_{\Psi \to n} \langle \Psi | \hat{T} | \Psi \rangle, \tag{3.10}$$

is the kinetic energy of non-interacting system.
The ground-state energy of the interacting system can then be written in terms of the non-interacting kinetic energy, the Hartree energy and the rest, which is called exchange-correlation energy:

$$F[n] = T_S[n] + U[n] + E_{xc}[n]. \tag{3.11}$$

Inserting $F[n]$ into Eq. (3.7) and comparing with Eq. 3.9 yields

$$V_S(\mathbf{r}) = V_{ext}(\mathbf{r}) + \int d^3r \frac{n(\mathbf{r})}{|\mathbf{r} - \mathbf{r}'|} + V_{xc}[n](\mathbf{r}), \qquad V_{xc}(\mathbf{r}) = \frac{\delta E_{xc}}{\delta n(\mathbf{r})}. \tag{3.12}$$

This is the most important relationship of exact density functional theory: From the functional dependence of $F[n]$ one can extract the potential felt by the non-interacting electrons of the same density.

Important points of the KS formulation are

— The KS equations are exact, and yield the exact density. For each physical system, the Kohn-Sham formalism is well-defined and unique.

— The KS equations are a set of single-particle equations, and are therefore much easier to solve than the original Schrödinger equation, especially for the case of large numbers of electrons. However, in turn, the unknown exchange-correlation energy cannot be dealt with exactly and must be approximated.

— The great advantage of the KS equations in comparison to Thomas-Fermi theory is that almost all of the kinetic energy, T_S, is treated exactly.

— After substracting T_S and U from F, we are left with the exchange-correlation energy which turns out to be very amenable to local type of approximations.

3.5 Exchange and correlation for the homogeneous electron liquid

A large amount of useful information about general properties of $E_{xc}[n]$ has been obtained by simulating of simple benchmark systems like the homogeneous electron gas. This is a system of interacting electrons of homogeneous density, the charge of which is compensated by a positive homogeneous background charge. It is convenient here to

start from the exchange energy and then generalize the results to the correlation energy. Introducing explicitly spin variables one obtaines

$$E_x = -\frac{1}{2}\iint \frac{n_x^{(\uparrow)}(\mathbf{r},\mathbf{r}')n^{(\uparrow)}(\mathbf{r}')}{|\mathbf{r}-\mathbf{r}'|}\, d^3r\, d^3r' - \frac{1}{2}\iint \frac{n_x^{(\downarrow)}(\mathbf{r},\mathbf{r}')n^{(\downarrow)}(\mathbf{r}')}{|\mathbf{r}-\mathbf{r}'|}\, d^3r\, d^3r'. \tag{3.13}$$

This formula reflects the fact that the exchange interaction does not "mix" two spin components, i.e.,

$$E_x[n^{(\uparrow)}, n^{(\downarrow)}] = E_x[n^{(\uparrow)}] + E_x[n^{(\downarrow)}]. \tag{3.14}$$

Further, the exchange energy density, $\epsilon_x(\mathbf{r})$, is introduced which satisfies

$$E_x = \int d\mathbf{r}\epsilon_x(\mathbf{r})n(\mathbf{r}) \tag{3.15}$$

without loss of generality as long as $\epsilon_x(\mathbf{r})$ depends on the density in all space, but not just at $\mathbf{r}$. After integration and introducing the spin polarization $\zeta(\mathbf{r})$,

$$\zeta = \frac{n^{(\uparrow)} - n^{(\downarrow)}}{n} \quad \text{with} \quad n = n^{(\uparrow)} + n^{(\downarrow)}, \tag{3.16}$$

the exchange energy density can be expressed as

$$\epsilon_x(\mathbf{r},\zeta) = -\frac{3}{2}\left(\frac{3}{4\pi}\right)^{1/3}\frac{n^{4/3}}{2^{4/3}}\left[(1+\zeta)^{4/3} + (1-\zeta)^{4/3}\right]. \tag{3.17}$$

With respect to the dependence on the spin polarization, the exchange energy density can be considered as an interpolation between limiting values of "paramagnetic", $\epsilon_x(\mathbf{r},0)$, and "ferromagnetic", $\epsilon_x(\mathbf{r},1)$, cases so that

$$\epsilon_x(\mathbf{r},\zeta) = \epsilon_x(\mathbf{r},0) + [\epsilon_x(\mathbf{r},1) - \epsilon_x(\mathbf{r},0)]f(\zeta), \tag{3.18}$$

with

$$f(\zeta) = \frac{(1+\zeta)^{4/3} + (1-\zeta)^{4/3} - 2}{2^{4/3} - 2} \tag{3.19}$$

known as the von Barth - Hedin interpolation function (von Barth and Hedin, 1972).

Von Barth and Hedin calculated the correlation energy of a spin-polarized electron gas in lowest order of the random phase approximation for different values of ζ. It was shown that the same interpolation function is accurate enough for the correlation energy density, so that one can write the exchange-correlation in the form

$$\epsilon_{xc}(\mathbf{r},\zeta) = \epsilon_{xc}(\mathbf{r},0) + [\epsilon_{xc}(\mathbf{r},1) - \epsilon_{xc}(\mathbf{r},0)]f(\zeta). \tag{3.20}$$

3.5.1 The local density approximation

The idea of the local density approximation (LDA) was introduced by Kohn and Sham bt also the key point of the Thomas-Fermi method. Once the kinetic energy, $T_S[n]$, is treated exactly, one can use the uniform-electron-gas formula to deal with the unknown parts of the energy functional. Thus, one applies the uniform-electron-gas results to infinitestimal volumes of the interacting system, which contain $n(\mathbf{r})d^3r$ electrons, and sums these local contributions over all space. The resulting scheme is called the local density approximation to the density functional theory. The exchange-correlation energy is then expressed as integral,

$$E_{xc}^{\mathrm{LDA}}[n] = \int d^3r\ \epsilon_x(n(\mathbf{r}), \zeta(\mathbf{r}))n(\mathbf{r}). \tag{3.21}$$

The LDA represents a poorly-justified but reasonable generalization, that is expected to work at least for the case of slowly varying density. In practical calculations, the LDA works surprisingly well. The reason is that the xc energy is the integral over the xc hole of the density times the Coulomb interaction. The Coulomb interaction is spherically symmetric and leaves only a sphrerically averaged part of $n_{xc}(\mathbf{r}, \mathbf{r}')$ around $\mathbf{r}$, which contributes to E_{xc}. The performance of LDA in real systems with chemical bonding (molecules, solids) has been addressed in a large number of publications. When discussing ground-state properties, LDA almost always underestimates the equilibrium volume by a few percent, which reflects the fact that LDA overestimates chemical bonding. This can lead to wrong ground states. The bulk α-Fe is one of the famoust examples, for which LDA fails.

3.5.2 The generalized gradient approximation

One way to get a better description of E_{xc} is to take into account inhomogeneities of the density via gradient expansions. A formally correct gradient expansion is

$$E_{xc}[n] = \int n(\mathbf{r})\epsilon_{xc}^{\mathrm{LDA}}\left[n(\mathbf{r})\right] d^3r + \int B_{xc}\left[n(\mathbf{r})\right] |\nabla n(\mathbf{n})|^2 d^3r + \ldots \tag{3.22}$$

However this expression meets certain problems in its practical implementation:

- The terms of 4th and higher order in the expansion of the exchange energy diverges.
- The exchange potential diverges already in 2nd order.
- In 2nd order, gradient corrections to the exchange energy bring an improvement, but gradient corrections to correlation energy can yield worse results than the LDA.

Therefore, one has to impose necessary constrains, probably using additional gradient terms (nonlinear and not necessary quadratic) beyond those included in the formal gradient expansion (3.22). These working schemes with explicite nonlinear dependence of the

integrand on density and its gradients are refered to as different flavours of generalized gradient approximation (GGA),

$$E_{xc}^{\mathrm{GGA}}[n] = \int n(\mathbf{r})\epsilon_{xc}^{\mathrm{GGA}}\left[n(\mathbf{r}, |\nabla n(\mathbf{r})|, \nabla^2 n(\mathbf{r}))\right]\ d^3r. \tag{3.23}$$

The parametrization of $\epsilon_{xc}^{\mathrm{GGA}}$ is chosen so as to satisfy certain limiting cases, like the LDA.

One of the most sophisticated forms of $\epsilon_{xc}^{\mathrm{GGA}}$ incorporating both exchange and correlation, that satisfies most of essential conditions, has been proposed in 1991 by Perdew and Wang (Perdew, 1992). It is written in terms of n and ζ of Eq. (3.16); $r_s = (3/(4\pi n))^{1/3}$; $g = [(1+\zeta)^{2/3} + (1-\zeta)^{2/3}]/2$; two differently scaled density gradients $s = |\nabla n|/(2nk_F)$ and $t = |\nabla n|/(2gn\sqrt{4k_F/\pi})$, where $k_F = (3\pi^2/n)^{1/3}$, and many tabulated numerical parameters:

$$\begin{aligned}
&\epsilon_{xc}^{(\mathrm{PW91})} = \epsilon_x + \epsilon_c,\\
&\epsilon_x = \epsilon_x^{(\mathrm{LDA})}(n,\zeta)\left[\frac{1 + a_1 s \sinh^{-1}(a_2 s) + (a_3 + a_4 e^{-100s^2})s^2}{1 + a_1 s \sinh^{-1}(a_2 s) + a_5 s^4}\right],\\
&\epsilon_c = \epsilon_c^{(\mathrm{LDA})}(n,\zeta) + H(n,t);\\
&H = \frac{q^3\beta^2}{2\alpha}\log\left[1 + \frac{2\alpha}{\beta}\frac{t^2 + At^4}{1 + At^2 + A^2t^4}\right] + C_{c0}[C_c(n) - C_{c1}]q^3t^2e^{-100g^4(4t^2/(\pi k_F))},\\
&A = \frac{2\alpha}{\beta}\left\{\exp\left[-\frac{2\alpha\epsilon_c^{(\mathrm{LDA})}(n,\zeta)}{g^3\beta^2}\right] - 1\right\}^{-1},\\
&C_c(n) = C_1 + \frac{C_2 + C_3 r_s + C_4 r_s^2}{1 + C_5 r_s + C_6 r_s^2 + C_7 r_s^3}.
\end{aligned} \tag{3.24}$$

An extensive literature exists on the performance of GGA for different systems (Corso, Pasquarello, Baldereschi and Car, 1996). Generally, GGA tends to correct to some extent the effect of overbonding that is typical for LDA results. The equilibrium volumes are typically larger as compared to LDA, i.e., which is closer to physical volumes, and in many cases agrement with experiment improves. In some cases, the GGA slightly overestimates the volume. Quite important is the inclusion of GGA when treating magnetic systems. One of the most known examples of LDA failures is the hierarchy of energies for the different (magnetic and structural) phases of iron, where the LDA wrongly predicts the fcc phase to be favourable over the bcc structure. The inclusion of gradient corrections restores the correct relation between these phases.

3.6 Basis sets

A practical application of the methods described above would imply that one has to solve a system of (integro)-differential equations, which is in many cases too difficult. A remarkable progress was achieved with the use of basis sets in which the unknown functions

can be expanded. Certain approximations on the shape of one-electron wavefunctions and potential helped further on to simplify the problem for the numerical treatment. As example one can mention the so called muffin-tin approximation, which is used in the augmented plane wave (APW) (Singh, 1994), the Korringa Kohn Rostoker (KKR) (Gonis, 2000), the linear augmented plane wave (LAPW) and the linear muffin-tin orbital (LMTO) formalisms (Springborg, 2000). However, with the increase of the computer power the trend of solving the Kohn-Sham equations "directly", i.e., without relation to any particular basis set, becomes noticeable and promising.

The idea is to expand one-electron functions in terms of a limited basis set and thereby reducing the integro-differential equations to a matrix eigenvalue problem. The first attempts to do so are probably due to Roothaan (Roothaan, 1951). The same approach can be applied to both the Hartree-Fock and Kohn-Sham methods. For example the HF equation can be written in a bit simplified form as

$$\left[-\frac{1}{2}\nabla^2 + U(x) + \int \frac{n(x')dx'}{|\mathbf{r}-\mathbf{r}'|}\right]\phi_\alpha(x) - \int \frac{n(x,x')\phi_\alpha(x')}{|\mathbf{r}-\mathbf{r}'|}dx' = \epsilon_\alpha\phi_\alpha(x). \tag{3.25}$$

In case of the Kohn-Sham equation one uses the substitution

$$-\int \frac{n(x,x')\phi_\alpha(x')}{|\mathbf{r}-\mathbf{r}'|}dx' \quad \Longrightarrow \quad V_{XC}(x)\phi_\alpha(x). \tag{3.26}$$

The generalized coordinate used here incorporates both position and spin $x = \{\mathbf{r}, \sigma\}$. It is possible to expand $\phi_\alpha(x)$ over a basis set χ:

$$\phi_\alpha(x) = \sum_{p=1}^{Q} C_{\alpha p}\chi_p(x), \tag{3.27}$$

where the dimension of the basis Q is reasonably larger than the number of occupied states N, and $\chi_p(x)$ may retain the dependence on both spatial and spin variables. Then, the initial equation reduces to

$$\sum_p C_{\alpha p} H\chi_p(x) = \epsilon_\alpha \sum_p C_{\alpha p}\chi_p(x), \tag{3.28}$$

with H is the Hamiltonian of a reference system of independent particles, which produces the one-electron density equal to the correct one. Multiplying the above equation on the left by $\chi_q^*(x)$ and integrating over x yields

$$\sum_p C_{\alpha p}\left[\int \chi_q^*(x)H\chi_p(x)dx - \epsilon_\alpha \int \chi_q^*(x)\chi_p(x)dx\right] = 0. \tag{3.29}$$

This is a system of algebraic equations for the expansion coefficients $C_{\alpha p}$, or a generalized diagonalization problem. The overlap matrix elements

$$S_{qp} = \int \chi_q^*(x)\chi_p(x)dx \tag{3.30}$$

need to be calculated only once (for basis functions fixed in advance). The matrix elements of the Hamiltonian

$$H_{qp} = \int \chi_q^*(x) \left[-\frac{1}{2}\nabla^2 + U(x) + \int \frac{n(x')dx'}{|\mathbf{r}-\mathbf{r}'|} + V_{xc}(x) \right] \chi_p(x) dx \tag{3.31}$$

still depend (via n and V_{xc}) on the yet unknown coefficients $C_{\alpha p}$. Typically, only the eigenvectors corresponding to N lowest eigenvalues ϵ_α must be included in the construction of the ground-state density, so the density is

$$n(x) = \sum_{\alpha=1}^{N} \phi_\alpha^*(x)\phi_\alpha(x) = \sum_{pq} \underbrace{\left[\sum_{\alpha=1}^{N} C_{\alpha q}^* C_{\alpha p} \right]}_{\text{density matrix}} \chi_q^*(x)\chi_p(x). \tag{3.32}$$

The density can be either diagonal in the spin variables, if basis functions for both spin components remain completely decoupled, or it may retain a general form, if spin components interact due to spin-orbit interaction and/or spin non-collinearity effects are included. The internal dependency of H_{qp} on $C_{\alpha q}$ via the density matrix prevents the solution of Eq. (3.32) as in a single matrix manipulation. However, an iterative solution is possible: One fixes a trial set of $C_{\alpha q}$ in the density matrix and constructs the Hamiltonian, then Eq. (3.32) becomes a system of linear equations solvable by a single diagonalization. Among the $C_{\alpha q}$ ($q = 1, \ldots Q > N$) found by diagonalization one selects those corresponding to the N lowest eigenvalues, uses them to update the density matrix and proceeds till everything convereges. In practical calculations, one would typically use a "dempfing" parameter $\beta < 1$,

$$C^{next} = \beta C^{new} + (1-\beta)C^{old}$$

or a more sophisticated mixing scheme.

So far, the specific form of the basis functions χ has not been discussed. A quite common choice is to use atom-centered functions localized in real space. Also, the functions localized in reciprocal space (plane waves) can be a convenient option,

$$\chi_{\mathbf{k}}^{\mathbf{G}} = \frac{1}{\sqrt{\Omega}} e^{\imath(\mathbf{k}+\mathbf{G})}.$$

Some hybrid basis set can be constructed as well. The choice of basis is usually related to the nature of boundary conditions used. Thus, for a simulation of a periodic solid with Bloch-von Karman boundary conditions the use of a plane wave basis set seems a natural choice, whereas non-periodic systems like molecules or clusters may be better treated with localized atom-centered basis. Between the two extremities of plane waves and atom-centered functions as candidates for a basis set definition, a large variety of combined methods has been developed and is in use. The practical situation is that the electron density in real materials behave very differently near atomic cores (large fluctuations with short spatial period) and far from the cores (smooth distribution of the density with possibly elevated values on the atomic bonds).

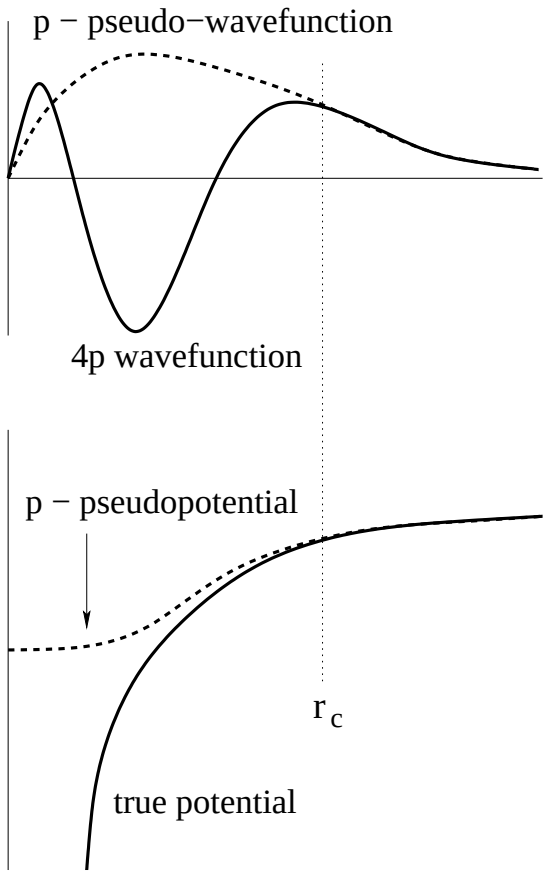

Figure 3.1: Schematic view of pseudo-wavefunctions and corresponding pseudopotentials. The pseudo-wavefunction is smooth and has no nodes in contrast to the "true" one. At $r > r_c$, the pseudo-wavefunction concides with the all-electron wavefunction which is an important constraint imposed on the pseudopotential. Compared to the real Coulomb field of a bare charge, the pseudopotential has no singularity in the vicinity of the nuclei.

3.7 Pseudopotentials

In planewave calculations, the main problem arises when dealing with rapidly fluctuating electron densities in the vicinity of atomic cores. One needs a very large number of plane waves in order to describe such fluctuations properly. The only possibility to save a purely planewave basis set is to discard core states. The exclusion of the cire states from the direct consideration means that one has to deal in the following not with the effect of bare nuclei potentials, but rather with the potentials screened by the core electrons. This potential is more smooth and shallow than the "true" one. This simplification gives rise to a family of pseudopotential methods in contrast to the "all-electron methods" (i.e., those where all electrons, valence and core electrons, are treated in the same way).

Historically, the pseudopotential approach is related to the orthogonalized planewave method (OPW), in which the basis set consists of plane waves, orthogonalized to lower-lying core states χ^{α}_{core}:

$$\chi_{k+G}(\mathbf{r}) = e^{\imath(\mathbf{k}+\mathbf{G})\mathbf{r}} - \sum_{\alpha}\sum_{core}\langle\chi^{\alpha}_{core}|e^{\imath(\mathbf{k}+\mathbf{G})\mathbf{r}}\rangle\chi^{\alpha}_{core}(\mathbf{r}).$$

The most straightforward way of screening the "true" potential with a fixed core density is not practically used. The Coulomb field of a not fully compensated bare charge

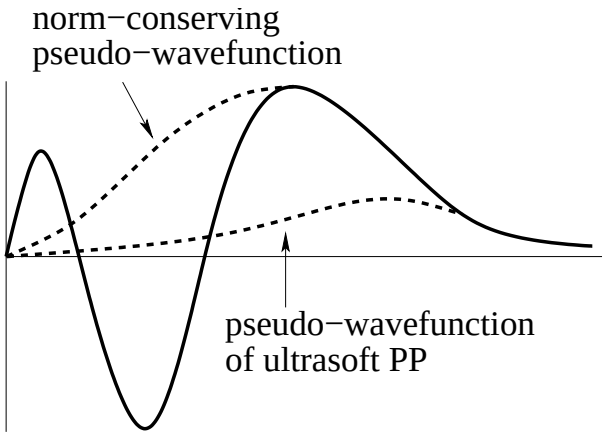

Figure 3.2: Schematic representation of the pseudo-wavefunction of an ultrasoft pseudopotential compared to the pseudo-wavefunction of a norm-conserving pseudopotential.

remains singular at the nuclei. Moreover, a true valence wavefunction must have nodes in the intra-atomic region for ensuring its orthogonality to the core states. The description of these nodes by plane waves needs high cutoffs. In reality, one works with smooth node-free pseudofunctions generated in a shallow pseudopotential.

The construction of a pseudopotential typically starts with the choice of an appropriate reference configuration (e.g., Fe$3d^7 4s^1$) and pseudopotential radii r_c, which can be different for different l-channels. As a rule, the following conditions are imposed:

- The pseudofunction must have no nodes (in order to avoid wiggles that would demand for higher cutoff).
- The pseudofunction matches the all-electron one beyond the cutoff radius.
- Norm conservation, meaning that the charge contained within the pseudopotential radius is the same for the pseudofunction and the all-electron one. Otherwise, deviations from this rule give rise to ultrasoft pseudopotentials.
- The eigenvalues corresponding to pseudofunctions must be equal to those of the all-electron solution - at least for the reference configuration.

Nowadays, pseudopotentials being in use are usually of *ab-initio* nature. They are "cooked" (with the use of certain approximations and criteria) from the "true" (all-electron) solutions for free atoms or ions.

As it was mentioned above, there can be some deviations from the rule of norm conservation for pseudopotentials. Namely, Vanderbilt (Vanderbilt, 1990) suggested to abandon the norm-conservation condition, that would allow to make the pseudolization radius r_c essentially larger (see Fig. 3.2), limited only by the condition that the spheres of this radius centered on different atoms must not overlap in a simulation. A big advantage would be that pseudopotentials generated with larger r_c are much softer and hence a much lower planewave cutoff is needed.

The ultrasoft pseudopotentials acn be characterized by some important features:

- The cutoff radius R, beyond which all all-electron and pseudo-properties (wavefunctions, potential) coincide, is only limited by next-neighbor distance.

- The necessary planewave cutoff for the planewave basis is drastically reduced.
- The amount of computational work (in the generation of pseudopotential) is increased. But most of these additional efforts need not to be repeated in the course of iterations.
- If the local potential in the sphere varies in the course of iterations, it can be considered as part of pseudopotential, so the pseudopotential develops itself as the calculation proceeds (similar to all-electron methods).
- The main area of application of ultrasoft pseudopotentials is for large systems, where the relative cost of the pseudopotential generation is relatively low, as compared to solving the electronic structure problem. For the latter, a low planewave cutoff is a major advantage.

3.8 Projector-Augmented wave method

The Projector-Augmented wave method (PAW) has been developen by Peter Blöchl in 1994 (Blöchl, 1994). The new method was needed to enhance the accuracy and computational efficiency of the plane wave pseudopotential approach and to provide the correct wave functions, rather than the ficticious wave functions provided by the pseudopotential approach. The PAW method describes the wave functions by a superposition of different terms: There is a plane wave part, the pseudo wave function, and expansions into atomc and pseudo-atomic orbitals at each atom. One one hand, the plane wave part has the flexibility to describe the bonding and tail region of the wave function, but fails to describe correctly all the oscillations of the wave function near the nuclei. On the other hand, the expansions into atomic orbitals are well suited to describe the nodal structure of the wave function near the nuclei, but the local orbitals lack flexibility to describe the bonding and tail regions. The PAW method combines the virtues of both numerical representations in one well-defined basis set.

In order to avoid solving two electronic structure calculations, i.e., one with plane waves and one using atomic orbitals, the PAW method does not determine the coefficients of the “atomic orbitals” variationally. Instead, they are unique functions of the plane wave coefficients. The PAW method is in principle able to recover rigorously the density functional total energy, if plane wave and atomic orbital expansions are complete. This provides a systematic way to improve the basis set errors.

3.9 Software and required computer facilities

4 Results of calculations for Ni_2MnGa

The purpose this work is to simulate and explain the variety of structural properties of the Ni_2MnGa compound by using state-of-the-art computational *ab-initio* methods. According to the experimental data, there are several structures that are found in Ni_2MnGa corresponding to different thermodynamic conditions. In terms of theoretical simulations it means that there might be several different arrangements of the atoms, which realize different local energy minima, whereby the deepest minimum would be related to the ground state structure. Other minima, which are not so deep as compared to the ground state, correspond to metastable structures. Each of these metastable states could be ground states under some different conditions (at higher temperature, under pressure, in magnetic field, etc). All these minima exist on the energy hypersurface, which dimensionality is defined by the number of degrees of freedom given by the structure of Ni_2MnGa. At this point, one faces a general minimization problem which, practically, has no general solution. There is no method, which would scan the hypersurface and find all possible minima. Mathematical methods of minimization work in the vicinity of some minimum providing an exact position of it at the end of the calculation. The only way to perform the minimization is to use some preliminary information which would allow to locate roughly the positions of the hypothetical minima. First of all this information is usually given by experimental investigations. Secondly, the knowledge of crystallography allows to consider different structures in separated domains according to their symmetry. From the Landau theory one knows that the high symmetry structure undergoes phase transformations to different structures of lower symmetry. Thus, it is natural for this kind of calculations to start from the structure which has the highest symmetry and then reduce its symmetry towards other stable structures.

4.1 Volume-c/a optimization

In case of Ni_2MnGa, we have complete information about the high temperature cubic $L2_1$ structure, but only partial information about other structures (see Table 2.1). It is convenient for the whole series of calculations to keep the $L2_1$ structure as a reference system and to reproduce first the properties of this structure in the calculations. This also gives some information about the accuracy of the method being used. The $L2_1$ structure can be simulated by supplying coordinates of four atoms in the basis of the fcc cell by using the experimentally determined lattice parameter $a = 5.820$ Å (Webster, Ziebeck, Town and Peak, 1984). The corresponding coordinates of the atoms

Ga	(0,0,0),
Ni	(1/4,1/4,1/4),
Mn	(1/2,1/2,1/2),
Ni	(3/4,3/4,3/4).

Since all the atoms are in high symmetry positions known from experiment, the only degree of freedom to be optimized is the volume, the result of which allows then a comparison of the experimentally determined lattice constant with the theoretical one. Depending on the method of calculation the theoretical volume will be more or less different from the experimental value. But it is important for calculations to use the theoretical one keeping in mind that this value is not really transferable from one method of calculations to another. In Figure 4.1 (left), the total energy of Ni_2MnGa is plotted against the lattice parameter. The minimum of this curve determines the equilibrium theoretical lattice parameter yielding $a = 5.8067$ Å. In order to obtain a very accurate position of this minimum, a special fit procedure has been used, which is based on the equation of state for a solid under pressure derived by F. D. Murnaghan (Murnaghan, 1944). One of coefficients being used in this fit is the bulk modulus, which is in this case $B_0 = 155.42$ GPa (result of PAW calculation using the VASP - *Vienna Ab-initio Simulation Package*). A corresponding calculation done with the VASP code, but a using different numerical scheme gives different results for the lattice parameter and related values (see Fig. 4.1 (right)). As mentioned above when discussing elements of the DFT, the LDA calculation underestimates the volume, while the gradient corrections for the exchange-corelation (GGA) yield a remarkable improvement to the lattice parameter. Using of PAW instead of pseudopotentials gives a smaller lattice parameter compared to the GGA & PP calculation, but the difference is not dramatic, and it will be shown later that the PAW method is more accurate with respect to other important aspects.

Table 4.1: Structural and magnetic parameters of the $L2_1$ structure of Ni_2MnGa calculated by different methods and compared to the experimental values. Magnetic moments are given for low temperatures, $T \ll 300$ K

	Structural parameters		Magnetic moments (μ_B)			
Method	Lattice const. (Å)	Bulk mod. (GPa)	Total	Mn	Ni	Ga
VASP GGA & PAW	5.8076	155.42	4.0	3.41	0.324	-0.058
VASP GGA & PP	5.8205	149.72	4.22	3.588	0.347	-0.061
KKR-ASA	5.7273	177.72	3.783	3.217	0.308	-0.05
LSD & PP [a]	5.7735	170	4.228	3.700	0.301	-0.075
FLAPW GGA [b]	5.8106	156	4.09	3.360	0.370	-0.04
Experiment [c]	5.82	149	4.17	...	...	...

[a] Godlevsky and Rabe (2001)
[b] Ayuela *et al.* (1999)
[c] Webster *et al.* (1984)

Table 4.1 summarizes structural and magnetic parameters obtained from different calculations. It shows that, in principle, all theoretical values are in a good agreement with experimental findings. This allows us to assume that other calculated properties, which have no experimental counterparts, will also be reliable.

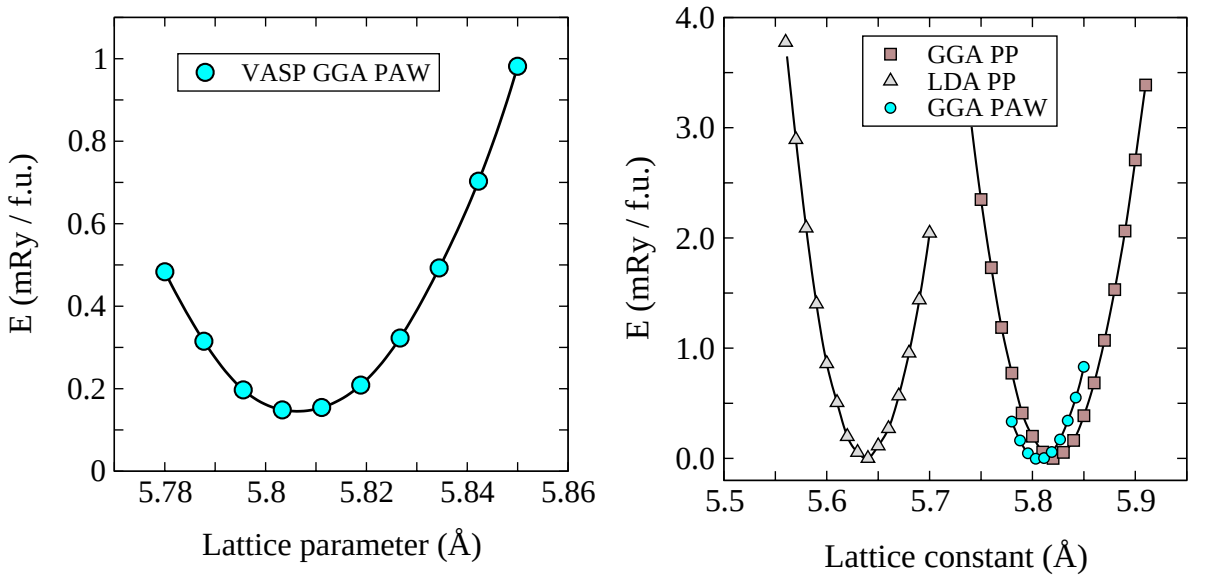

Figure 4.1: The total energy of $L2_1$ Ni_2MnGa as a function of the volume. Left: The total energy calculated by the most sophisticated available method, namely, by using VASP with the GGA and PAW schemes. Right: The total energy calculated by using different schemes implemented in VASP, which are: LDA & PP, GGA & PP, and GGA & PAW.

As the $L2_1$ structure has been defined properly, the next step is to deform this structure in such a way that other stable structures will be found. From experimental data, it is known that there are at least two tetragonal structures and one orthorhombic. It is natural to gradually reduce the symmetry first from the cubic towards the tetragonal, and then to extend the deformations further for the case of the orthorhombic structure one or structures of even lower symmetry.

A tetragonal deformation can be applied to the initial cubic structure by changing corresponding lattice parameters. Tetragonal symmetry implies that the lattice parameters of the basal plane coincide, $a = b$, while the tetragonality ratio c/a is changed. Additional restrictions arise from the condition of a constant volume. It is reasonable to keep the volume constant in order to make the calculations more transparent. The corresponding transformation matrix (Söderling, Eriksson, Wills and Boring, 1993) is then

$$\begin{bmatrix} 1+\delta & 0 & 0 \\ 0 & 1+\delta & 0 \\ 0 & 0 & \dfrac{1}{(1+\delta)^2} \end{bmatrix}, \tag{4.1}$$

where δ is the normalized change of the lattice constant relative to the undistorted case.

Figure 4.2 shows the total energy of Ni_2MnGa as a function of the c/a ratio calculated for the optimal volume, which is kept constant. Two different minima of the energy correspond to two different structures. One of them, at $c/a = 1$, is the cubic $L2_1$ structure. The second minimum is found close to $c/a = 1.25$ and has considerably lower energy as compared to the cubic structure. This tetragonal structure is known from experiment

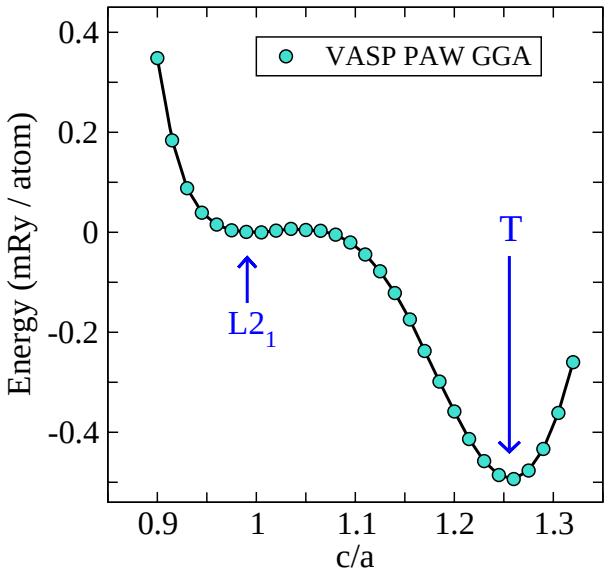

Figure 4.2: The total energy of Ni_2MnGa as a function of the c/a ratio calculated for constant volume. The minimum at $c/a = 1$ corresponds to the cubic $L2_1$ structure, which is the high-temperature phase. In fact, $L2_1$ is metastable with respect to tetragonal distortion at with $c/a \approx 1.25$, the T structure (see Table 2.1).

(denoted as T in Table 2.1) (Martynov and Kokorin, 1992) and from calculations (Ayuela, Enkovaara, Ullakko and Nieminen, 1999). Relative energy values of both structures agree with the experimental situation, where the $L2_1$ structure is stable at high temperatures, and becomes metastable at low temperatures. The T structure, in turn, is one of the low-temperature structures of Ni_2MnGa.

According to Table 2.1, there should be another minimum of energy at $c/a = 0.94$, which would correspond to the tetragonal 5M structure. The 5M structure is usually the ground state of Ni_2MnGa at low temperatures. The T structure must be metastable with respect to the 5M (at least for stoichiometric Ni_2MnGa). As mentioned in the introduction, the T structure can be obtained from the 5M one by applying a uniaxial pressure to the sample. The question is now, why the 5M structure does not appear in Fig. 4.2 at $c/a < 1$. The same question was addressed by other research groups involved in theoretical investigations of Ni_2MnGa (Ayuela, Enkovaara, Ullakko and Nieminen, 1999). It is believed that the numerical methods being in use here are accurate enough. Hence, some physics being responsible for the stability of the ground state is missing. It is a challenge for the following calculations to find the factors, which make the $c/a < 1$ structure stable. This will be the central point for the further discussions in this work.

The c/a curve (Fig. 4.2) is very flat in the vicinity of $c/a = 1$. It could be that some very tiny effect is needed to obtain the missing minimum at $c/a = 0.94$, as it was proposed by Ayuela *et al.* (2002). However, the missing minimum must not only be at $c/a = 0.94$, but must also have the lowest energy compared to all other structures. Since the calculations above were done for constant volume it is reasonable to investigate first the effect of volume variation on the c/a-curve. Therefore, a series of c/a calculations have been performed for different volumes. Figure 4.3 shows the evolution of the c/a curves when the volume is changed. One of the effects is that increasing the volume makes the tetragonal structure at $c/a > 1$ less stable. However, both minima move towards higher energies away from the optimal volume. But it shows that the stability of the tetragonal

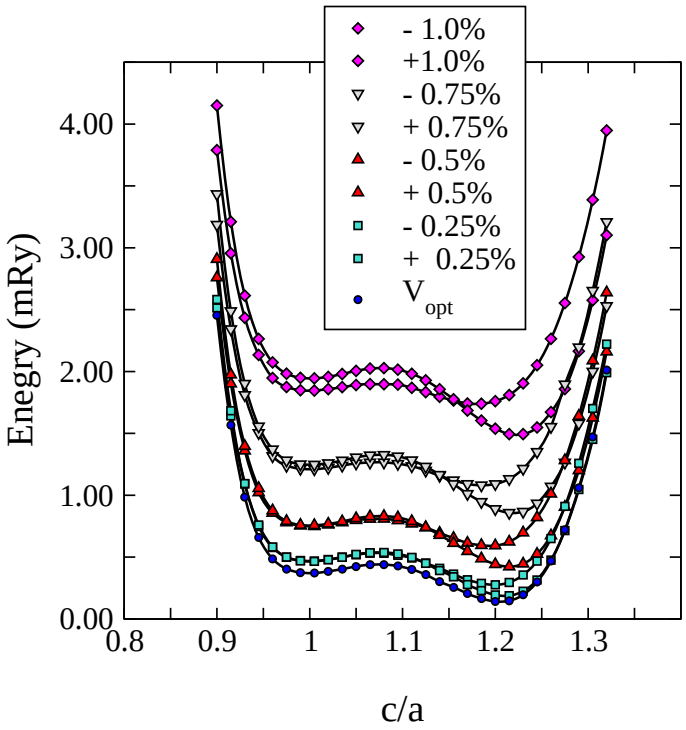

Figure 4.3: The total energy of Ni_2MnGa as a function of the c/a ratio for different volumes.

structure significantly depends on the volume. In Fig. 4.4 the relative change of the energies for the two structures is shown. The curves have been joined together in such a way that zero energy corresponds to the $L2_1$ structure.

The electronic origin of the stable $c/a > 1$ structure (as discussed by Ayuela *et al.* (2002)) is associated with a kind of Jahn-Teller effect in the metallic system. The increase of the volume reduces the overlap of the electron orbitals making the tetragonal structure less favourable. Smaller volumes force the system to reduce its symmetry in order to accommodate the electrons in a tighter area.

It is seen now that all these c/a calculations for various volumes do not yield the stability of other structures, in particular, the one at $c/a = 0.94$. Moreover, for $c/a < 1$ the total energy increases so fast due to the electrostatic repulsion that it would be extremely difficult to expect any structure with $c/a < 1$ to be stable. The strong increase of the energy can be explained in terms of the atomic structure. Namely, both Mn and Ni have nearly spherical distributions of the charge around them making tetragonal deformations towards $c/a < 1$ very unfavourable.

In order to make sure that no other minima have been lost in the present calculations, a corresponding total iso-energy surface in the c/a-volume plane has been evaluated, which is shown in Fig. 4.5. This plot illustrates clearly that no other structures apart from the $L2_1$ and T can be obtained when considering cubic and tetragonal structures. Hence other phases of Ni_2MnGa found experimentally must be of lower symmetry.

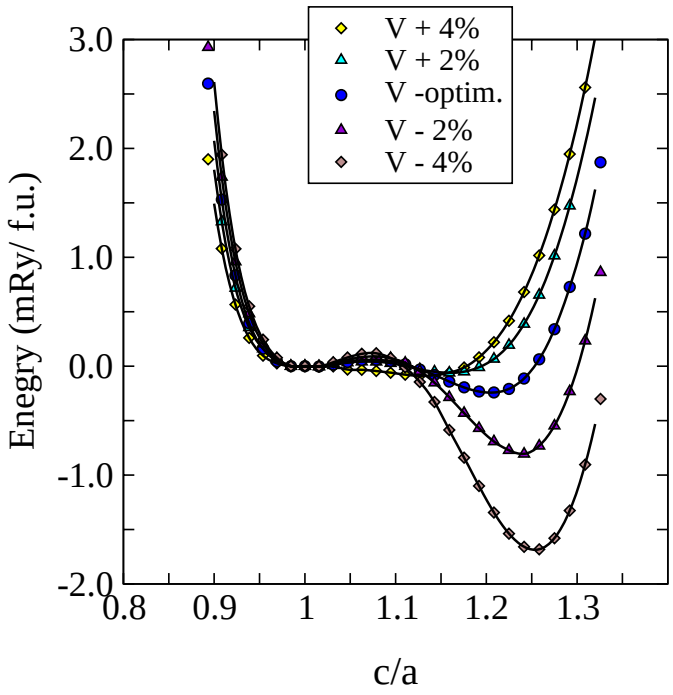

Figure 4.4: The relative change of the total energy as a function of c/a for different volumes. The zero of energy corresponds to the $L2_1$ structure.

4.2 Magnetic moments

Variation of the c/a ratio yields considerable changes in the magnetic parameters of the system. The total magnetic moment as a function of the c/a ratio is shown in Fig. 4.6 (left). It has two maxima: at $c/a \approx 0.94$ and $c/a \approx 1.15$. Remarkable is that the total magnetic moment has a pronounced minimum at $c/a = 1$, i.e., for the cubic structure, and the position of the maxima at $c/a = 0.94$ coincides exactly with the value of c/a for the missing 5M structure. The minimum and both maxima are mostly due to the contribution of Ni to the total magnetic moment (Fig. 4.6, right). This can be associated with the small peak of the Ni minority electron density of states located just below the Fermi level (Fig. 2.5 (left)). The magnetic moment of Ni is smaller than the one of Mn, but is very important for the exchange interaction yielding the ferromagnetic order in Ni_2MnGa (Kübler, Williams and Sommers, 1983). Moreover, Ni is the one contributing mainly to the magnetic anisotropy energy in Ni_2MnGa as found by Enkovaara *et al.* (2002a). The Mn atoms, in turn, exhibit maximal magnetic moment in the cubic structure (Fig. 4.7, left). According to Kübler *et al.* (1983), the Mn-to-Mn coupling might be mediated by Ni, but the atoms of Ga can play a very important role in the exchange interaction as well. If we concentrate on Fig. 4.6 (right) and Fig. 4.7 (left), it is seen that there is no correlation between the two curves. Some correlation would be present if Mn-Mn interaction were mediated by the Ni atoms alone. This means that Ga contributes to the formation of the magnetic moment at the Mn site, depending on the position of the Fermi level with

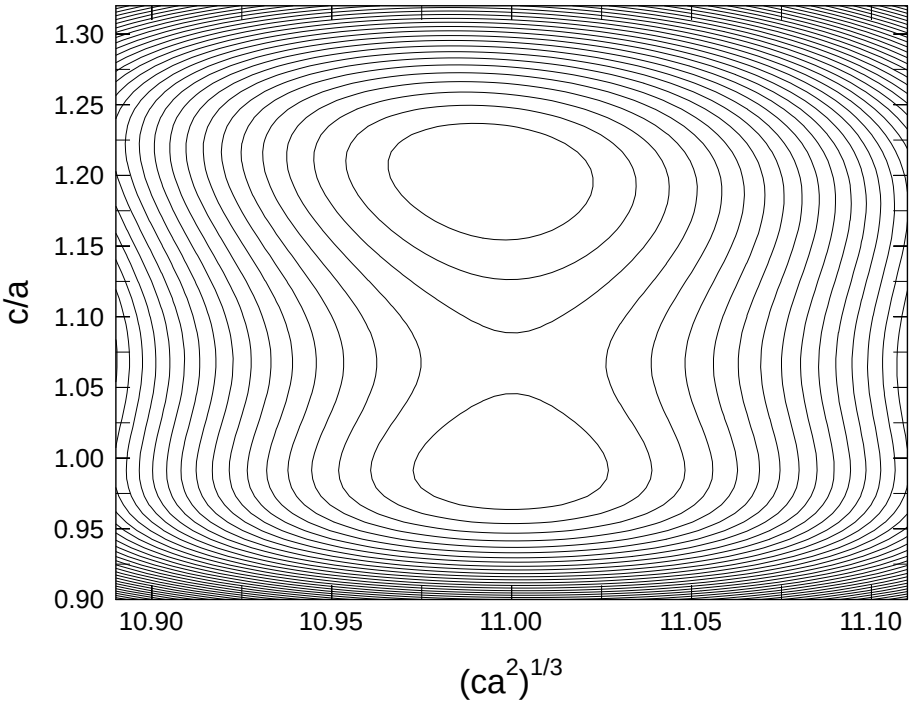

Figure 4.5: The iso-energy surface for Ni_2MnGa in the (c/a-volume) plane. The contour lines are at intervals of 0.125 mRy.

respect to the Mn-Ga or Ni-Ga p-d hybrid states (Kübler, Williams and Sommers, 1983). One more plot (Fig. 4.7, right) shows the dependence of the total magnetic moment on the volume.

A detailed analysis of the magnetic moments can provide useful information about the electronic structure of Ni_2MnGa. In this context the role of the peak in the Ni minority-spin density of states is of special interest. The minimum of the total magnetic moment at $c/a = 1$ is due to the contribution of Ni, but the question is what causes the reduction of the magnetic moment of Ni without affecting the magnetic moments of Mn. Ga, in turn, has no magnetic moment. However the presence of Ga in Ni_2MnGa makes it very different from other metallic systems. It was calculated by Godlevsky and Rabe (2001) that the binary Mn-Ni alloy also shows ferromagnetic order. This system one obtains by replacing all Ga atoms in Ni_2MnGa by Mn atoms. The Ni-Mn alloy has a stable cubic structure. The calculated total magnetic moment for this structure as a function of c/a shows no minimum at $c/a = 1$, instead, the curve is very much similar to the one of Mn in Fig. 4.7 (left). One can suggest that without Ga, Ni does not show the kind of dependence presented in Fig. 4.6 (right).

The Ga-p and Ni-d minority-spin orbitals form hybrid states, which can be responsible for many of the Ni_2MnGa properties. Kübler *et al.* (1983) have considered several aspects of ferromagnetic ordering in Heusler alloys. In particular, the observation that the electronic structure of the Heusler alloys depends on the covalent interaction. Although

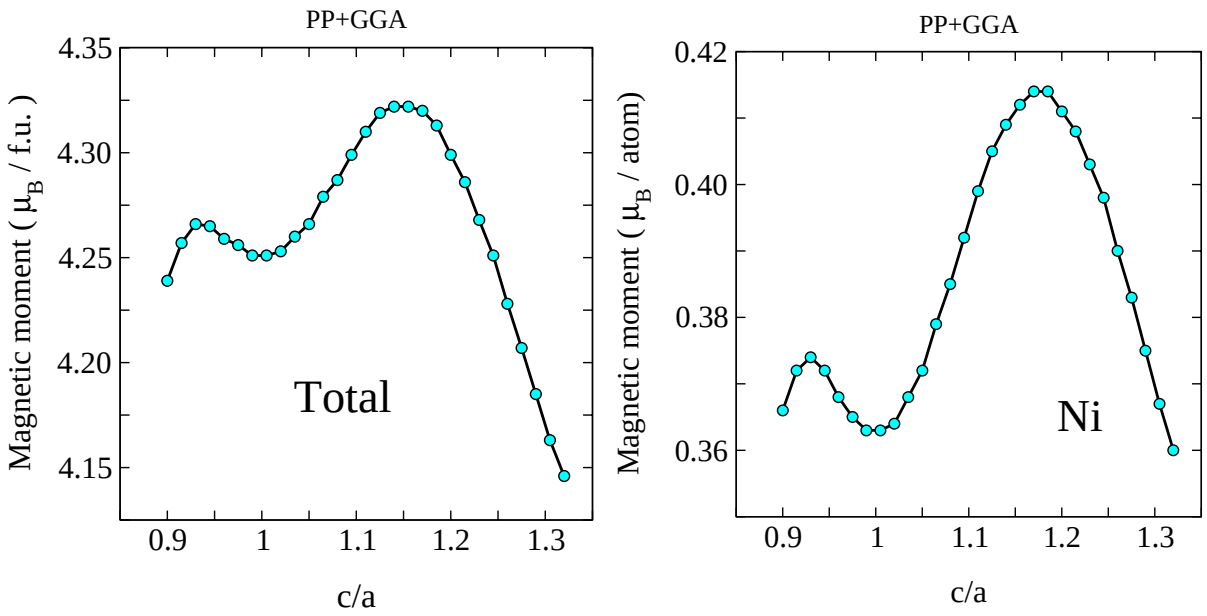

Figure 4.6: (Left) The total magnetic moment of Ni_2MnGa as a function of the c/a ratio. (Right) The corresponding Ni contribution to the magnetic moment.

this is very weak, the magnetic properties depend on it. It plays an important role in the competition between the ferro- and antiferromagnetic alignments of the moments. Two physical mechanisms are involved here. On one side, it is the intra-atomic exchange splitting of the Mn d states, on the other side, it is the covalent inter-atomic interaction of d states on different Mn atoms mediated by the d states of Ni and p states of Ga (or their hybrids).

Note, that the covalency mechanism favours the antiferromagnetic order, but not ferromagnetic order, because the interatomic interactions couple only electrons of the same spin. Also the interactions are only effective in lowering the total energy if the states involved lie both above and below the Fermi energy. The covalency mechanism lowers the energy of bonding hybrids and raises the energy of anti-bonding hybrids. This stands also for the minority density of states for Ni and Ga in Ni_2MnGa (shown in Fig. 2.5 and Fig. 2.4). The DOS of Ni exhibits a peak, just below the Fermi level which is due to the d-electrons, while the DOS of Ga exhibits a peak, just above E_F, which is stems from the p-states. Thus, for the cubic structure the DOS of Ni_2MnGa bears features, of of the anti-ferromagnetic order. The reason, why Ni_2MnGa is ferromagnetic, is connected with the contribution to the covalency arising from a mixture of states of different atoms, which form hybrid states. This implies for the case of Ni_2MnGa population of the minority-spin states close to E_F (see Fig. 2.4), and therefore a reduction of local magnetization and loss of exchange energy, which causes the minimum at $c/a = 1$ in Fig. 4.6. Thus, development of the covalent interaction in Ni_2MnGa means a loss of local magnetization on the Ni site. In other words, there is a competition between the effect of exchange energy and the possibility to form energetically favourable hybrid states. The maximum of the magnetic moment of Ni at $c/a = 0.94$ (see Fig. 2.5) shows that in this case hybrid state are not

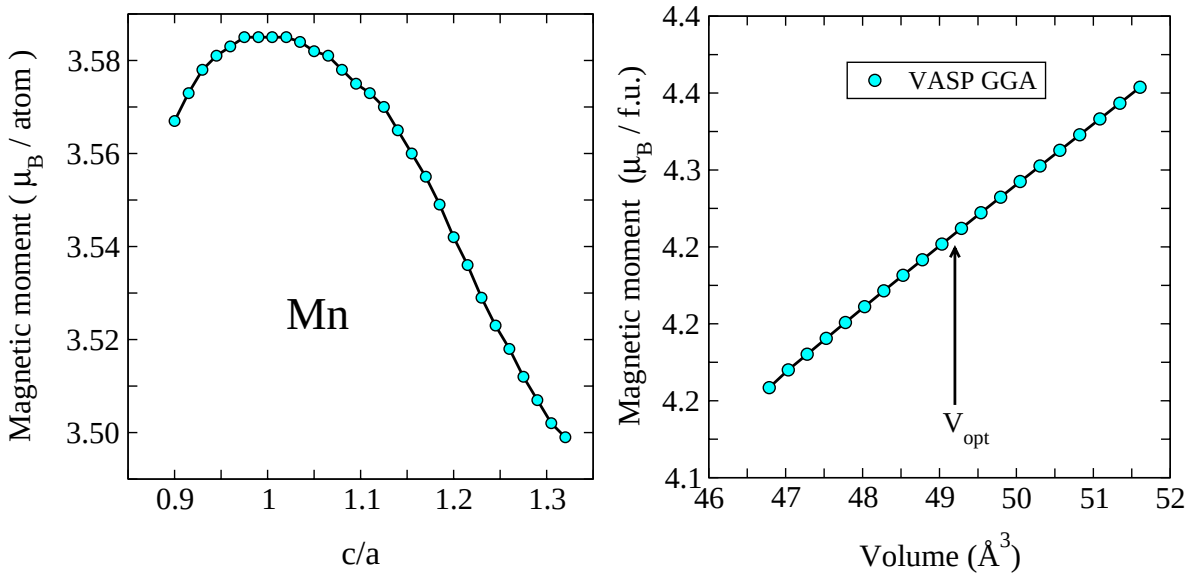

Figure 4.7: Left: The magnetic moment of Mn as a function of c/a. Right: Dependence of the total magnetic moment on the volume ($V_{\mathrm{opt}} = 49.2$ Å^3).

formed. As a consequence, the total energy of the system increases, which means that $c/a = 0.94$ corresponds to an energetically unfavourable distribution of Ga-p and Ni-d minority-spin orbitals. Hence, there is a tendency that the system will try to rearrange the atoms in such a way that hybrid states can form leading to a decrease of the Ni magnetic moments.

The two peaks in the minority DOS density of states of Ni (just below E_{F}) and Ga (just above E_{F}) arise from the hybrid orbitals and are responsible for the covalent interaction in Ni_2MnGa. We would like to emphasise that the interpretation of the maximum of the Ni magnetic moment and its increase (compared to the value for the cubic structure) for $c/a = 0.94$, is important. The peak in the Ni minority-spin DOS moves to higher energies thereby reducing the population of Ni-d states which form hybrid states with Ga. However, this situation is unstable because formation of the hybrid states is energetically more favourable compared to the small increase of exchange energy. This means that $c/a = 0.94$ structure requires for additional deformation, which will push the bonding Ni-Ga minority-spin hybrid states below E_{F}, thereby lowering the total energy.

We will emphasise the role of these hybrid states in all further discussions. It will be shown that this aspect is of crucial importance for the electronic structure of Ni_2MnGa. The question is now which kind of deformation is needed to stabilize the $c/a = 0.94$ structure.

4.3 Orthorhombic deformations

In the following we will discuss orthorhombic deformations of Ni_2MnGa as a further means to lower the symmetry compared to the cubic or tetragonal symmetry in order to obtain

other stable structures. The orthorhombic deformation of the initial cubic structure can be obtained by allowing all three lattice parameters to change, $a \neq b \neq c$, for the constant angles, $\alpha = \beta = \gamma = \pi/2$. An additional constraint arises from the condition of keeping the volume constant. It is convenient to express this deformation in terms of relative distortions, a/c and b/c. Then, for constant volume only two lattice parameters have to be changed.

The orthorhombic deformation can also be described by introducing a dimentionless parameter δ, which allows to derive corresponding equations of states and to obtain the physical parameters from them, like the elactic constant C_{44}. The transformation matrix depends on the cell it is applied to:

$$\begin{bmatrix} 1 & \delta & 0 \\ \delta & 1 & 0 \\ 0 & 0 & \dfrac{1}{1-\delta^2} \end{bmatrix} \text{ for s.t. , } \quad \begin{bmatrix} 1+\delta & 0 & 0 \\ 0 & 1-\delta & 0 \\ 0 & 0 & \dfrac{1}{1-\delta^2} \end{bmatrix} \text{ for s.c. . } \tag{4.2}$$

The constant C_{44} can be calculated from $U = 2C_{44}\delta^2 + O(\delta^4)$ yielding for Ni_2MnGa $C_{44} \approx 101.7$ GPa, which agrees well with experimental data as summarized in Ref. (Ayuela, Enkovaara, Ullakko and Nieminen, 1999). Here, H is the internal energy.

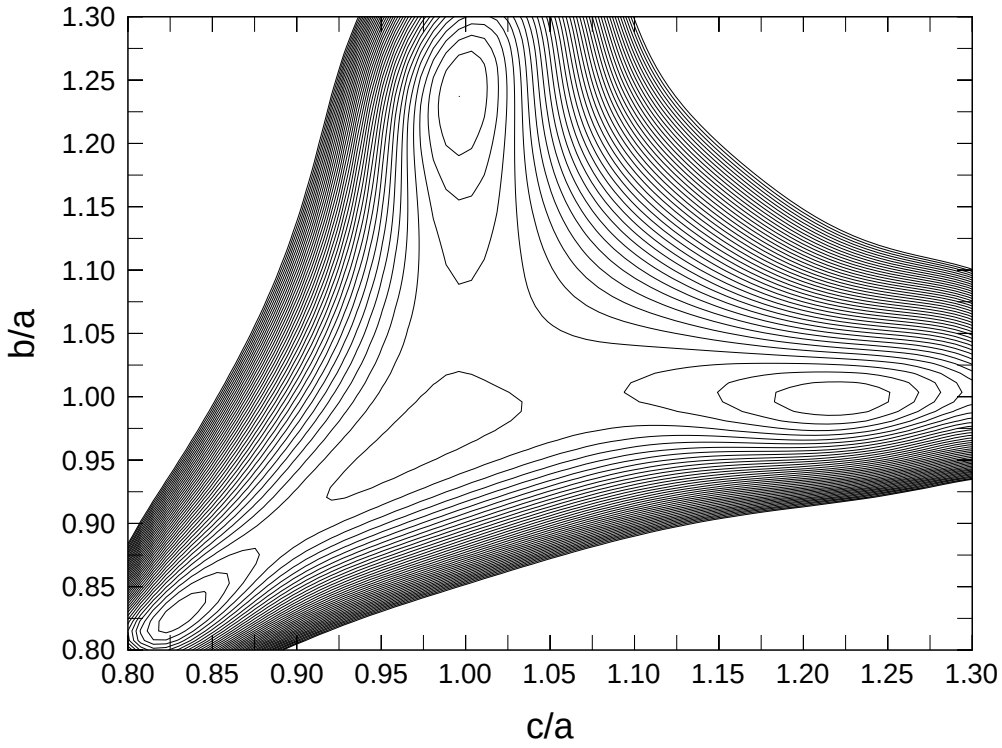

Figure 4.8: The iso-energy surface of Ni_2MnGa in the (b/a, c/a) plane (contour lines are at 0.2 mRy intervals).

The resulting iso-energy surface in the $(b/a,\ c/a)$ plane is shown in Fig. 4.8. This picture shows the energy for all possible combinations of the lattice parameters for the orthorhombic deformation at fixed volume. The point at $b/a = c/a = 1$ corresponds to the cubic structure $L2_1$. Three lines defined by the conditions $b/a = c/a$, $b/a = 1$, $c/a = 1$ correspond to the c/a curve shown in Fig. 4.2, i.e., to tetragonal symmetry. All other combinations of b/a and c/a lead to structures with orthorhombic symmetry. One can see that the orthorhombic deformations do not yield any new minima on the energy surface, and only shows the two minima, for the $L2_1$ and the T structures. Figure 4.8 shows three symmetrically equivalent minima corresponding to the corresponding directions for the tetragonal deformation, which are allowed by the symmetry.

We briefly conclude what has been done so far. The calculations of iso-energy surfaces did not show any sign of the structures 3M, 5M or 7M (see Table 2.1). The cubic $L2_1$ structure and the tetragonal T structure are present, with the latter one corresponding to the global minimum of the total energy. The next step would be to apply further deformations, for instance, a monoclinic one, which also leads to a lower symmetry. However, this is actually not necessary because it is clear that a completely different approach must be used to study this problem. What was done up to now takes only short range interactions into account. The deformations studied so far allow to draw statements on the role and influence of short-range interactions only. Obviously, the formation of other structures demands for a more sophisticated treatment and an investigation of long range interactions.

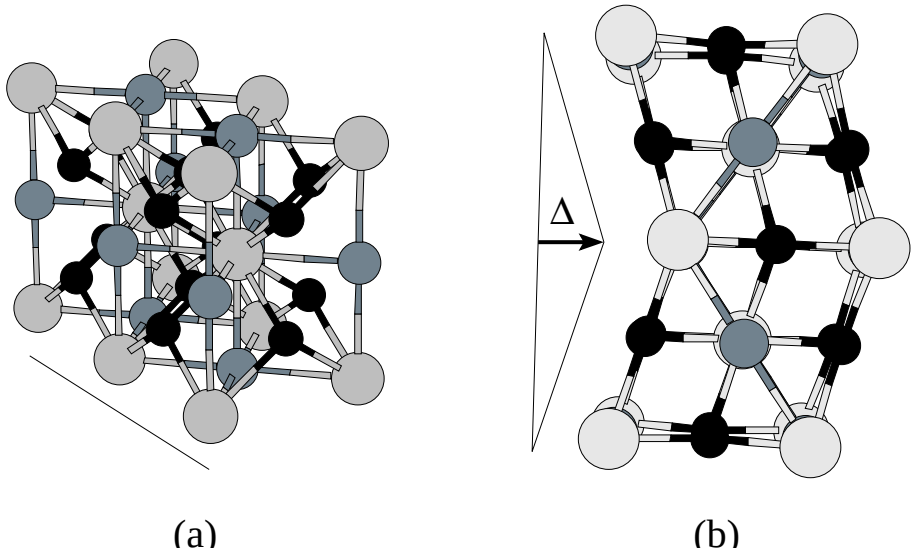

Figure 4.9: Schematic view of a supercell used to take into account the influence of long-range interactions due to atomic displacements in Ni_2MnGa. (a) A double supercell which consists of two bct cells; (b) deformation of this super-structure by an amount Δ.

In order to apply required deformations, we need to consider appropriately created supercells. The question is what is the optimum supercell to be chosen. An example of a small supercell formed by two bct structures (see Fig. 2.1) and corresponding deformation

by a parameter Δ is shown in Fig. 4.9. In this case a very small energy barrier has to be overcome in order obtain the deformed structure with twin-like shape. However, this structure is not stable in the calculations. The parameter Δ tends to increase until both parts of the structure form a structure which is identical with the T structure. Thus, a double supercell is not enough to study the impact of long range interactions.

The structures listed in Table 2.1 help to understand what is really missing in the calculations. Experimental studies seem to prove that the long range interactions may be caused by a modulation of the structure. All structures, which could not be obtained in the calculations so far are the 3M, 5M and 7M structures, where M stands for "modulated" (Martynov and Kokorin, 1992). But it is important to note that the modulations have so far not been considered as an important factor for the stabilization of certain structures. It was always considered to be a kind of exotic effect related to weak interactions. Modulations were not assumed to be related to the homogeneous tetragonal strains associated with a stiffening of the shear constant C'. The calculations done here show that all possible ways to obtain the missing structures without taking into account the modulation have been checked. It was necessary to do that regular work in order to clearly understand that the modulated shuffling of atoms according to the experimental data is the only reasonable way to proceed further. This will be the subject of the next chapter.

In addition a small amount of disorder in the Heusler alloy or the existence of vacancies could be important. The necessary electronic structure calculations which would take into account all possible atomic disorder effects simultaneously with the shuffles of atoms are extremely demanding and time consuming. We have performed so far a few calculations of atomic disorder effects. Preliminary results and conclusions drawn from are presented in the following chapters.

5 Modulation

As discussed above, the structures resulting from a modulated shuffling of atoms in Ni_2MnGa (see Table 2.1) cannot be obtained from calculations which take into account nearest neighbour interactions only. Modulated structures require supercell calculations. A problem here is that shuffling is associated with a bind of ambiguity having many degrees of freedom. It would be impossible to move atom by atom "by hands" in such circumstances. The solution is to use some optimization method (reference to some numerical methods) which will move atoms from their initial positions after each electronic-structure relaxation step, in directions dictated by local forces experienced by the atoms in the current configuration. After a number of such steps, the iteration process will hopefully finally converge to a configuration where the forces are zero, i.e., some stable structure. If the initial configuration has been chosen properly, the resulting structure will converge to the right energy minimum. An example of a wrongly chosen structure was shown in Fig. 4.9. Whatever initial shuffling of atoms was applied to that structure, it converged always towards the two already known structures: $L2_1$ and T. Not only the shuffling is important for such structure calculations, but one would also need to allow the volume and the the shape of the supercell to relax.

5.1 Supercell for the 5M structure

A straightforward way to start calculations of the modulated shuffling is to consider the five-layered structure obtained by Martynov and Kokorin (1992) (see Fig. 2.2). The construction of the supercell is explained in Fig. 5.1. It is created by merging together five bct unit cells, see Fig. 5.1(a). The result of merging is a long supercell, (Fig. 5.1(b,c), having orthorhombic symmetry. The basal plane is spanned by the $[1\bar{1}0]$ and [110] vectors of the $L2_1$ structure with the modulation along [110]. Altogether, ten atomic planes perpendicular to [110] are used to form the supercell incorporating two full periods of modulation in it. The modulation is generated by displacing these atomic planes along the $[1\bar{1}0]$ direction. Since two full five-layered periods fit into the supercell, the corresponding modulation wave vector is $(2\pi/a)[\zeta, \zeta, 0]$, $\zeta = 2/5 = 0.4$. The initial magnitude of the displacements, both for Ni and Ga-Mn layers, was chosen to be 0.175 Å. All atoms are displaced with the same phase according to the acoustic character of the static wave of modulation. In this way the supercell with modulation resembles as close as possible the experimentally observed structure (Fig. 2.2) (Martynov and Kokorin, 1992).

Due to the wave vector with $\zeta = 2/5 = 0.4$, the constructed structure (as well as the model in Fig. 2.2) is still different from what is really observed in experiment. The experimental structure has an incommensurate period with $\zeta = 2/5 = 0.433$ (Zheludev, Shapiro, Wochner and Tanner, 1996). However, this incommensurate structure cannot be presented by a supercell, which is ten atomic planes long, while a larger supercell is computationally too demanding. But we expect that $\zeta = 2/5 = 0.4$ is a rational approximation which will at least allow to study the physical implications.

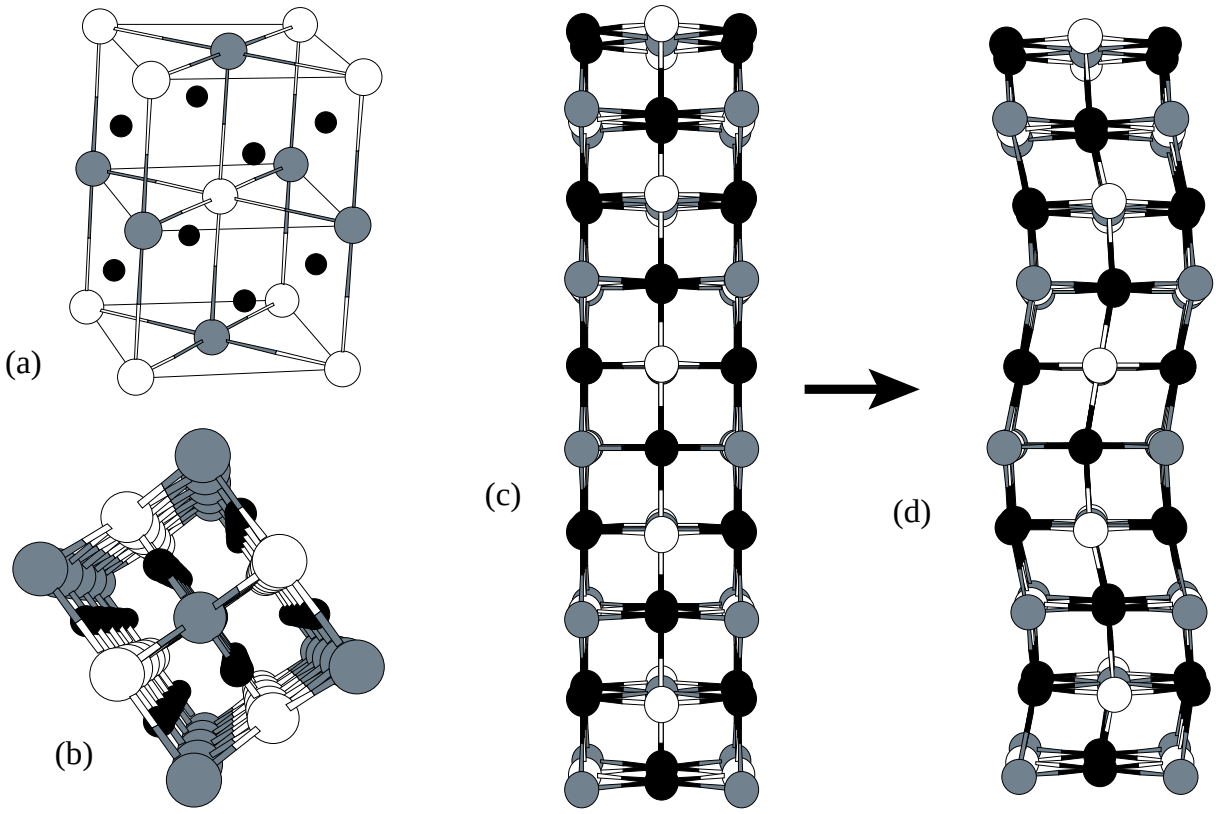

Figure 5.1: (a) The tetragonal unit cell of Ni_2MnGa. (b,c) Top and front view of the non-modulated supercell which consists of five tetragonal unit cells. (d) A modulated superstructure resembling the 5M structure of Ni_2MnGa.

This constructed orthorhombic supercell, see Fig. 5.1(d) has lattice parameters a', b' and c'. These parameters are related to the $L2_1$ lattice parameter $a = a_{L2_1} = 5.8067$ Å, see Table 4.1 (Ayuela, Enkovaara, Ullakko and Nieminen, 1999; Godlevsky and Rabe, 2001; Zayak, Entel and Hafner, 2003a) by $a' = a/\sqrt{2.0} = 4.106$ Å, $b' = 5a/\sqrt{2.0} = 20.53$ Å, $c' = c = a = 5.8067$ Å. In addition, a small tetragonal distortion, $c/a < 1$ is allowed in order to facilitate convergence in the calculations towards the structure, which is needed to be stabilized. The final supercell parameters are then $a' = a \times 0.709 \approx 4.127$ Å, $b' = 5 \times a' \approx 20.630$ Å, $c' = a \times 0.974 \approx 5.669$ Å, with a starting tetragonality ratio of $c/a \approx 0.971$.

5.2 Structural relaxation of the 5M structure

The Vienna *Ab-initio* Simulation Package (VASP) (Kresse and Furthmüller, 1996; Kresse and Joubert, 1999) with the implemented projector-augmented wave formalism (Blöchl, 1994), was used to perform the ionic relaxation. Within density functional theory (DFT) the electronic exchange and correlation are treated by using the generalized gradient approximation (GGA). Further computational details: the $3d$ states of Ga are included

as valence states, the plane-wave cutoff energy is chosen to be 241.6 eV, the Monkhorst-Pack k points generation scheme is used with a grid of $9 \times 7 \times 2$ points in the full Brillouin zone for a long orthorhombic supercell, which means 36 inequivalent k-points. A smearing parameter of 0.2 is used (after a careful test) which is the default value of VASP.

The atomic positions in the supercell were allowed to relax as well as the volume of the cell and its shape. By means of the conjugate-gradient algorithm the structure converged to a minimum of energy which is different from the minima found in other calculations (Ayuela, Enkovaara, Ullakko and Nieminen, 1999; Godlevsky and Rabe, 2001; Zayak, Entel and Hafner, 2003a). The period and phase of the modulation did not change with respect to the initial values. However, the ratios between the lattice parameters have changed considerably. New parameters of the supercell, after the convergence has been achieved, are $a' \approx 4.17$ Å, $b' \approx 20.73$ Å, $c' \approx 5.633$ Å. In comparison with the cubic phase we obtain a tetragonality of $c/a \approx 0.955$, which is close to the experimental value of $c/a = 0.94$.

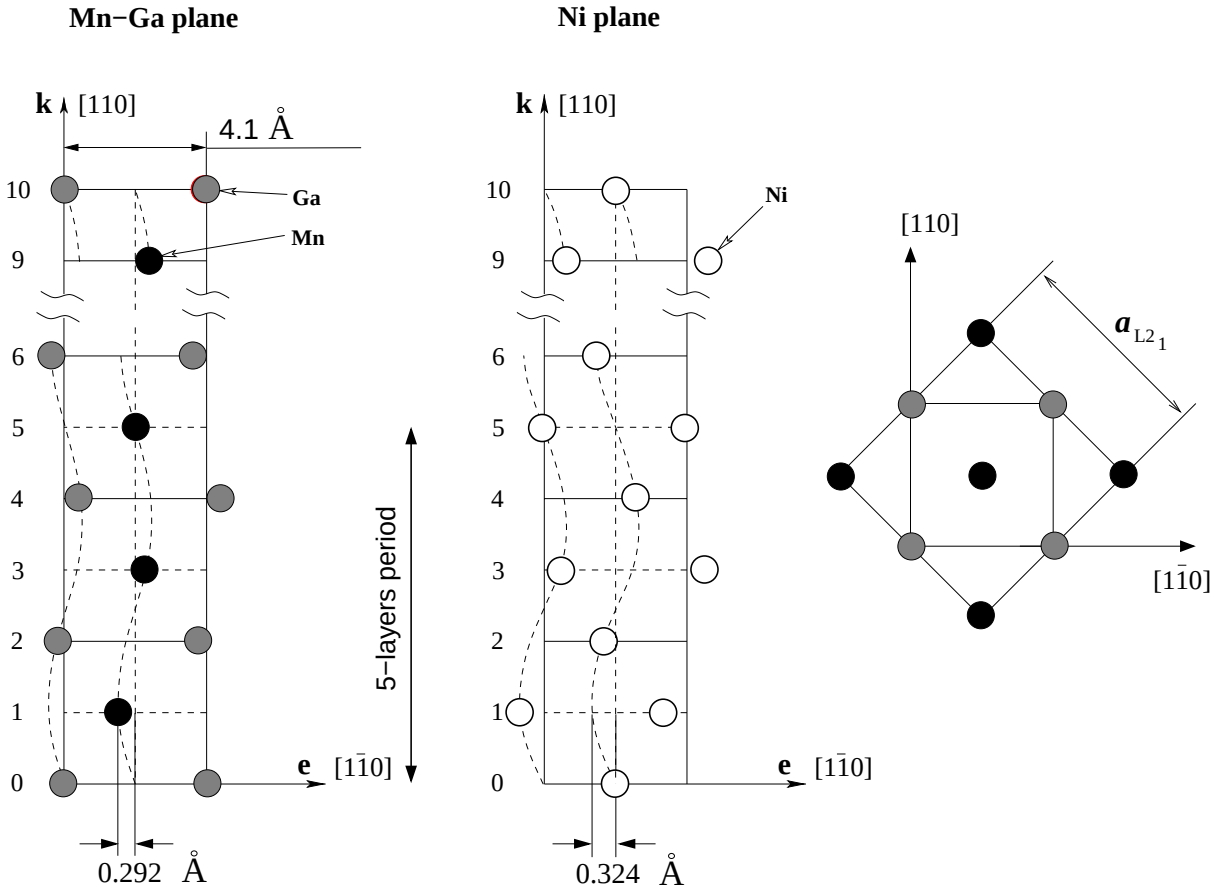

Figure 5.2: Computational results for the modulation of two different atomic planes (001) in Ni_2MnGa after structural relaxation.

A detailed consideration shows that the structure has two different atomic (001) layers

as sketched in Fig. 5.2. One of them consists of Mn and Ga atoms, while the second one consists only of Ni atoms in agreement with the experimental reference structure (Martynov and Kokorin, 1992). The modulation amplitudes in both atomic layers have different values: 0.292 Å and 0.324 Å for the Mn-Ga and Ni planes, respectively. These different amplitudes found theoretically have not yet been confirmed by experiment or mentioned in other works.

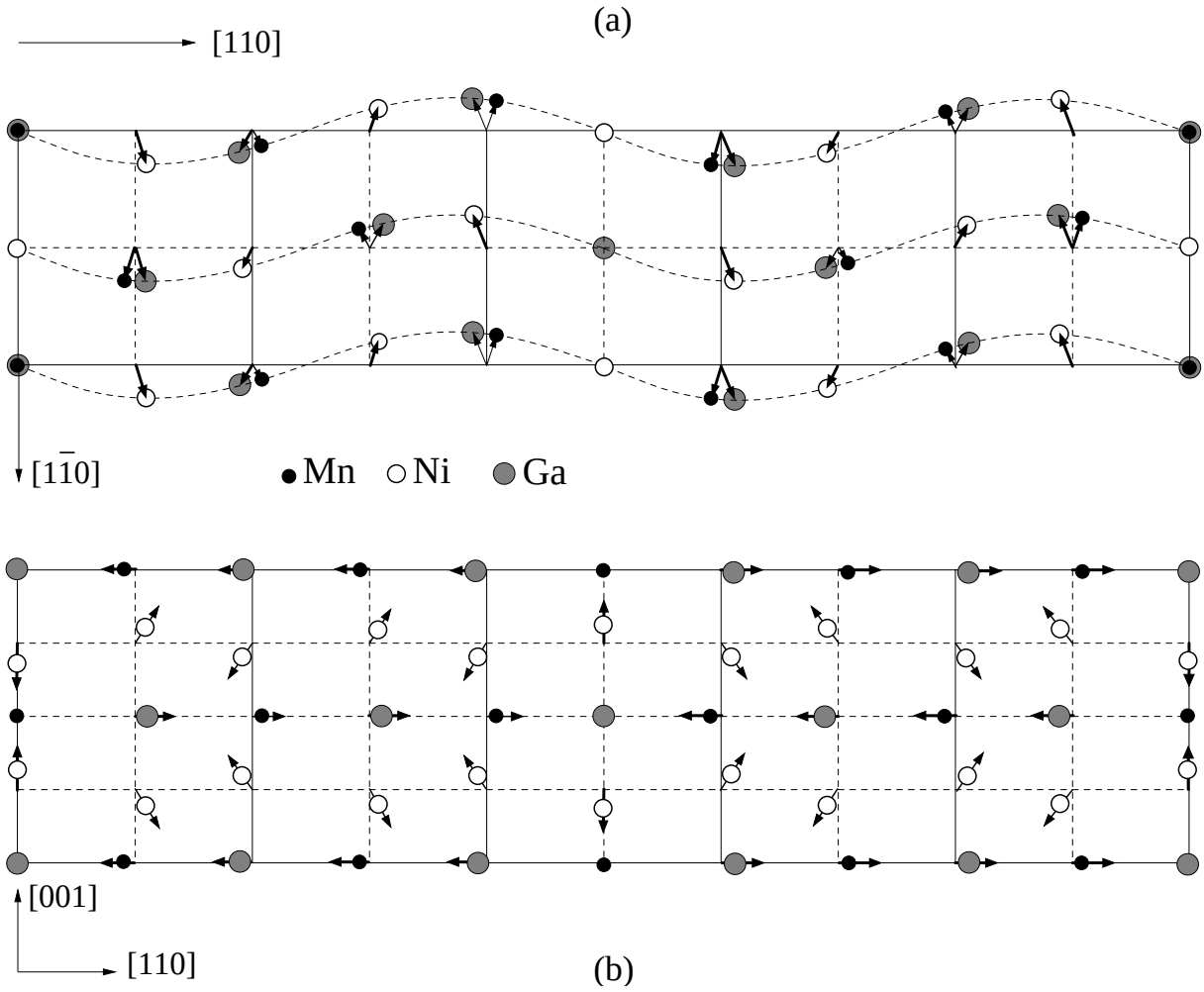

Figure 5.3: Modulated martensite 5M structure of Ni_2MnGa (schematically). In addition to the main modulation with polarization along the [1$\bar{1}$0] direction, there is a tiny shuffling, which moves atoms in directions [001] and [110], corresponding to displacements of the order of 0.001 Å, i.e., about 1% of the main modulation amplitude. These extremely small displacements of atoms have been enlarged the Figure for clearness. Black, white and gray dots show the positions of Mn, Ni and Ga, respectively.

In the model for the 5M structure proposed by Martynov and Kokorin (1992) shown in Fig. 5.2 the modulation is presented as a static wave with a perfect polarization, i.e., the atoms move only along one direction [1$\bar{1}$0] which is perpendicular to the propagation wave vector [110]. The atoms move in the same phase which agrees with the acoustic

nature of the anomaly. However, analysis of the calculated 5M structure shows that some additional effects are present. A more detailed consideration confirmed the existence of extremely small shuffling which, however, can be of great importance for the stability of the modulation. Figure 5.3 shows details of this fine structure. Altogether, we get a complicated structure with different amplitudes of the modulation for Mn-Ga planes and for planes containing Ni atoms, see Fig. 5.2 with the atoms moving not only along $[1\bar{1}0]$ direction, but also in directions [110] and [001]. In contrast to the main shuffling shown in Fig. 5.2, the fine shuffling involves just very small displacements of order 0.001 Å or about 1% of the main modulation.

The fine modulation shows several interesting features. In the (001) plane in Fig. 5.3(a) Ga and Ni approach each other forming a pair of atoms. The Mn atoms move towards the free space left by the Ni atoms. Another plane $(1\bar{1}0)$ in Fig. 5.3(b) shows that each Ga atom is actually connected with two Ni atoms at the same time. Thus, each Ga atom forms a group with two Ni atoms, which can be explained by the coupling of the Ga $4p$ and the Ni $3d$ states. The two peaks of the minority-spin DOS located near E_{F} in Fig. 2.5 and 2.4 are involved in this coupling. The formation of p-d hybrid states reduces the total energy of the system due to the covalent coupling of Ni and Ga states.

It is remarkable that this kind of deformation has been observed before in other systems and discussed in terms of the *rigid-hybrid* concept, which was introduced by Harrison and Phillips (1974) for the treatment of the $(C_{11} - C_{12})/2$ elastic constant [1]. We assume that the physical picture drawn by Harrison and Phillips (1974) for a crystal having the symmetry of diamond or zincblende, i.e., with cubic elasticity, stands also for Ni_2MnGa. The concept is based on the consideration of tetrahedral structures, which are also present in case of Ni_2MnGa. Each atom of Ni in Ni_2MnGa is surrounded by two tetrahedral structures, whereby one of them is formed by Ga and another one is formed by Mn atoms, see Fig. 1.1. There is radial distortion determining the value of the bulk modulus $(C_{11} + 2C_{12})/3$, and angular distortion determining $C_{11} - C_{12}$. The lattice is softened to those distortions which can be accommodated by the hybrids. Taking into account also a concept of *rehybridization* allows to explain that softening is reflected in a lower value of C_{44}. This is important because the softening of C_{44} has been observed in experiments for Ni_2MnGa (Mañosa Lluis, Planes, Zarestky, Lograsso *et al.*, 2001; Stenger and Trivisonno, 1998; Worgull, Petti and Trivisonno, 1996).

5.3 Stability of the 5M structure

The calculated super-structure in Fig. 5.2 and 5.3 has to be checked for stability with respect to the main degrees of freedom, which make this structure different from the previously known $L2_1$ and Tstructures. In other words, it must be a local energy minimum. The first parameter to check is the c/a ratio since the 5M structure known from experiment (Martynov and Kokorin, 1992) has tetragonality $c/a = 0.94$. Our computa-

[1] See Chapter 8 "Elasticity", Sections 8-B "Rigid Hybrids" and 8-C "Rehybridization" in (Harrison, 1980)

tional result of the relaxation of the atomic positions yields $c/a = 0.955$ value, which is close to the experimental value. However, the relaxation process requires extremely high accuracy in order to give correct structure parameters. Since, the relaxation is based on the calculation of local forces experienced by the atoms, we need in case of plane waves a very high energy cutoff in order to obtain accurate forces.

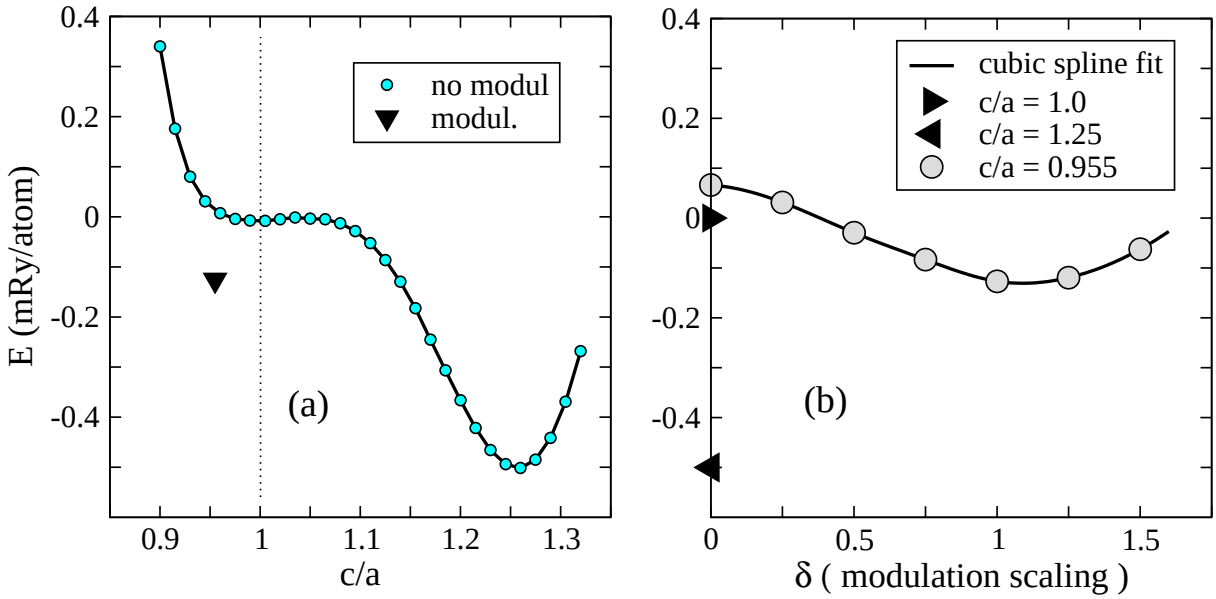

Figure 5.4: (a) Dependence of the total energy on the amplitude of modulation for a fixed tetragonality ratio of $c/a = 0.955$. (b) Variation of the energy if we scale the modulation with a parameter δ, where $\delta = 1.0$ corresponds to the optimum value found after structural relaxation while $\delta = 0.0$ means no modulation.

Figure 5.4 shows the total energy landscape for the unmodulated ($L2_1$ and T) and the new modulated (5M) structures. The dependence of the total energy on c/a for the non-modulated structure is presented in Fig. 5.4(a) (the same curve was shown in Fig. 4.2). In addition to the two minima obtained previously (Ayuela, Enkovaara, Ullakko and Nieminen, 1999; Zayak, Entel and Hafner, 2003a) the point marked by a triangle shows the energy decrease for the relaxed supercell structure with modulation obtained in the present calculations. The modulated structure is lower in energy compared to the cubic structure by about 0.15 mRa/atom, which, however, is not lower than the energy for the tetragonal structure T with $c/a \approx 1.25$. There can be several reasons for this. One of them is that the obtained modulation is not optimal. Probably, some additional shuffling must be taken into account, because the calculated modulation has a commensurate wave vector of $q = 0.4$ while the experimentally observed structure is incommensurate with $q = 0.433$.

The stability of the 5M structure shows that a finite amplitude of modulation leads to a local energy minimum. If we scale the modulation for fixed $c/a = 0.955$, by a factor δ we obtain the result shown in Fig. 5.4(b) [2]. The value $\delta = 1.0$ corresponds to the optimized

[2]This useful idea was kindly proposed by Andrei Postnikov

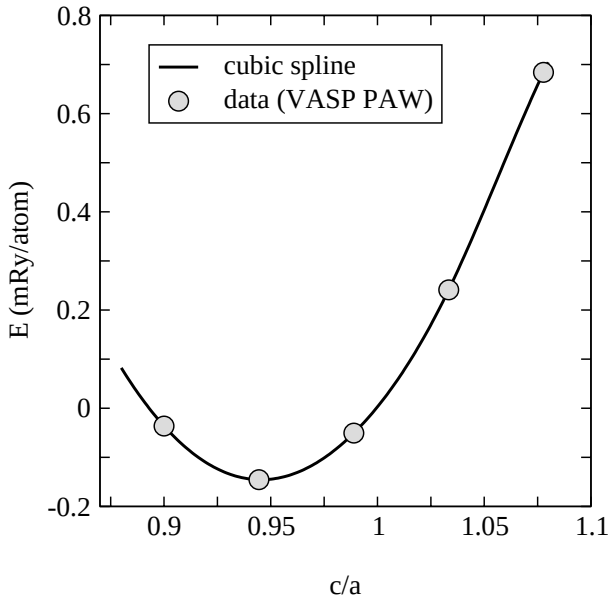

Figure 5.5: Dependence of the total energy on the variation of the c/a ratio for a fixed modulation obtained from relaxation. This curve agrees with experimental data for structures with $c/a \approx 0.94$.

structure while $\delta = 0.0$ describes the non-modulated case. It is obvious from Fig. 5.4(b) that a non-zero amplitude of modulation leads to a lower energy compared to the the energy of the $L2_1$ structure. Keeping the ratio $c/a = 0.955$ fixed, we obtain an optimum value for the amplitude of modulation. This optimum value gives a new crystal structure, which is energetically more favourable than the cubic structure ($c/a = 1.0$). The fact that this energy decrease is not large enough to suppress the $c/a \sim 1.25$ structure, which is so far one order of magnitude lower in energy compared to the case $c/a = 1.0$ (Ayuela, Enkovaara and Nieminen, 2002) is not really a negative result. One may speculate that if we were able to calculate the free energy, the lattice entropy term could favour the modulated structure at finite temperature and not the structure with $c/a \approx 1.25$. In addition as explained before, some disorder or non-collinear magnetic moments could further stabilize the modulated structure.

Results for the c/a variation over a large range for the optimum modulated 5M structure are shown in Fig. 5.5. This gives a considerable improvement with respect to previous total energy calculations, because the new tetragonality is $c/a = 0.94$, which is the experimental value as well. We may conclude that calculated low-temperature martensitic structure is derived from the high-temperature cubic structure through a combination of both a homogeneous lattice deformation and modulated shuffling of the atoms. This is also the clue to understand how the martensite phase will nucleate. Instead of twinning and stacking faults the modulation of the martensitic tetragonal structure of Ni_2MnGa corresponds to a smaller structural change which is easier to accommodate or to derive from the parent cubic structure. With respect to the electronic structure, the lowering of the symmetry leads to a splitting of the DOS peak at E_F, thereby decreasing the valence band energy contribution to the total energy. Thus, structural modulation and lowering of the electronic energy may explain the stability of the 5M structure of Ni_2MnGa below room temperature (Zayak, Entel, Enkovaara, Ayuela *et al.*, 2003c).

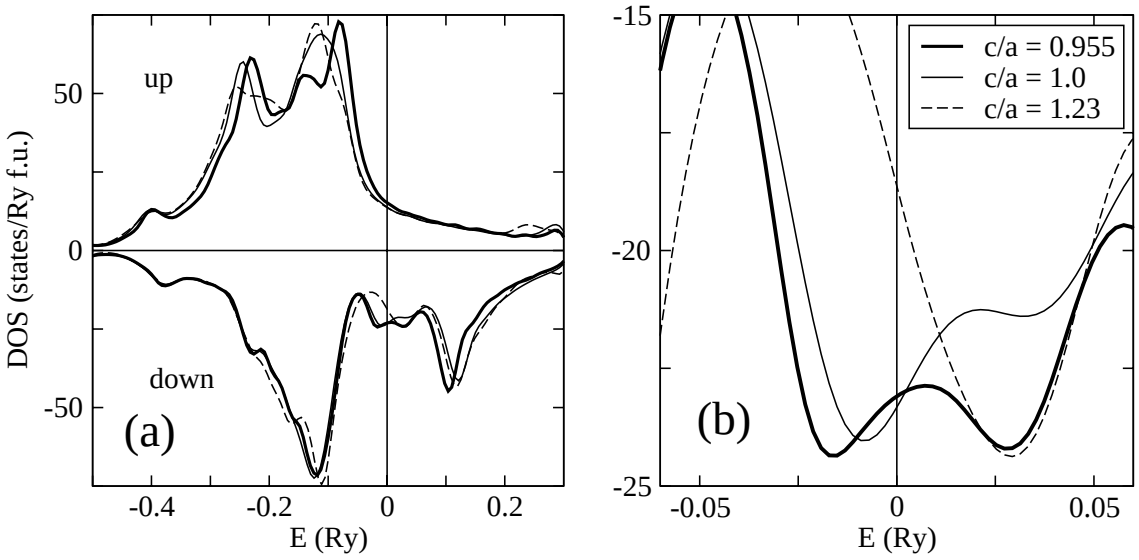

Figure 5.6: (a) Total density of states for three different structures of Ni_2MnGa: Cubic $L2_1$, tetragonal with $c/a \approx 1.25$ and modulated tetragonal structure with $c/a = 0.955$. (b) Enlargement of the minority spin DOS around the Fermi level.

5.4 Electronic properties of the 5M structure

In Fig. 5.6 we present the calculated DOS for the three different structures: The cubic structure ($c/a = 1.0$), the tetragonal structure ($c/a = 1.25$) and the modulated tetragonal 5M structure ($c/a = 0.955$). Figure 5.6(b) shows an enlargement of the minority-spin DOS around the Fermi level. Obviously the modulated tetragonal structure with $c/a = 0.955$[3] shows a tendency to open a pseudogap close to E_F, which arises from the hybridization of Ga-Ni states discussed above. The 5M structure can be characterized by showing a symmetrical distribution of bonding and anti-bonding p-d states around E_F, which is a particular feature of covalent bonding.

Although layered crystal structures are different from the Heusler structure, there is some useful analogy. On the basis of band theory (Singleton, 2001) many layered substances (organic molecular solids, oxides) are said to be unstable with respect to the so called *Peierls transition*, which causes a periodic modulation of the crystal structure. Figure 5.8 describes this schematically for a one-dimensional material: Fig. 5.8(a) displays the nearly free-electron band of a monovalent one-dimensional material with band gap at $\pm\pi/\alpha$ and the Fermi surface extension of half the length of the Brillouin zone, i.e., $k_F = \pm\pi/2\alpha$. The corresponding real space situation is shown in Fig. 5.8(b). On average there is one electron per atom, and electrons are free to move along the chain of atoms, which are spaced by α. It turns out that in this situation, a very simple distortion of the lattice in real space can lower the energy of the electron system. Such a distortion is shown in Fig. 5.8(d), where adjacent atoms have moved together to form *dimers* leading

[3]Here, we continue to discuss the 5M structure with $c/a = 0.955$ and not with $c/a = 0.94$ because most of the calculations and analysis were done before the value of $c/a = 0.94$ had been obtained.

the unit-cell of 2α, so that the Brillouin zone has halved in size, see Fig. 5.8(c) with the new boundaries at $\pm k_F = \pm\pi/2\alpha$. The band gap now opens up at the Brillouin-zone boundaries, lowering the electronic energy and turning the substance into an insulator.

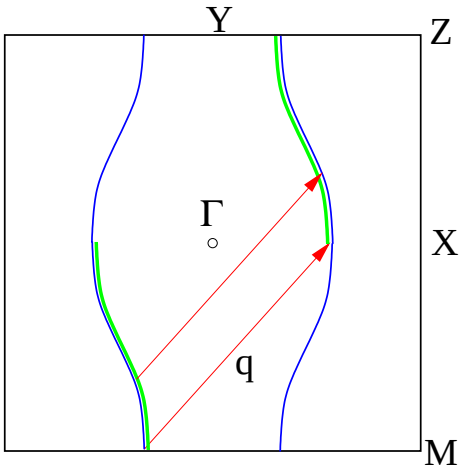

Figure 5.7: Nesting behaviour of a hypothetical Fermi surface in the (011) plane.

The distortion leads to the electronic charge piling up on the dimers, the resulting state is known as a *charge-density wave*, since the electron density has become modulated. A similar lowering of energy can be obtained by doubling the unit cell with a periodic modulation of the electron spin leading to the formation of a *spin-density wave*. Modulation of this type can be described by a series of terms $\propto \cos(Qx)$, where the wave vector Q is known as *nesting vector*. A detailed review of Peierls transitions is given in (Grüner, 1988; Kagoshima, Nagasawa and Sambongi, 1988).

A very similar effect is also observed in the case of Ni_2MnGa. The modulated shuffling moves the atoms in such a way that a pseudo-band gap opens at the Fermi level. In the literature this effect is usually described by other words, namely the origin of the modulation has been argued to be related to specific nesting properties of the Fermi surface (Lee, Rhee and Harmon, 2002; Velikokhatnyi and Naumov, 1999; Zheludev, Shapiro, Wochner and Tanner, 1996). For a three-dimensional metal, nesting means that a piece of a 3D Fermi surface can be translated by a single vector $\mathbf{q}$ and superposed on another piece of the Fermi surface. The Fermi surface is said, in this case, to be nested by the vector $\mathbf{q}$. Figure 5.7 schematically shows nesting of a two dimensional Fermi surface. The nesting vector reported for Ni_2MnGa is $q \approx 0.433$, i.e., the one which corresponds to the wave vector of the 5M modulation (Lee, Rhee and Harmon, 2002; Velikokhatnyi and Naumov, 1999).

Here the discussion of the Peierls transitions is used in addition to the discussion of the Fermi surface nesting in order to understand in a simple picture that interatomic coupling can explain the long-range modulated distortion. The shuffling of atoms shown in Fig. 5.2 and Fig. 5.3 indicates that the atoms move forming a kind of dimers similar to the situation shown in Fig. 5.8 for the Peierls distortion. We conjecture that this can lead to a kind of pseudo-gap in the minority-spin DOS shown in Fig. 5.6.

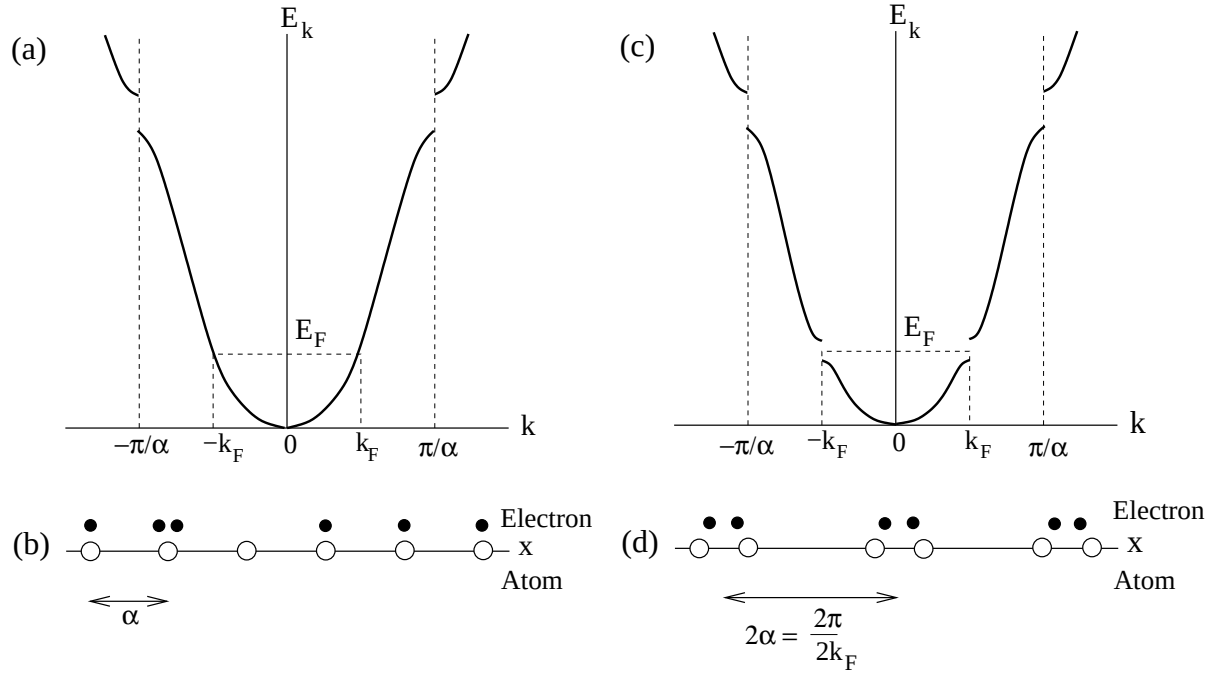

Figure 5.8: Figures taken from Singleton (2001): (a) A simple nearly-free electron band in a monovalent one-dimensional material with a band gap at the Brillouin-zone boundary; the Fermi surface extends over half of the Brillouin-zone. (b) The equivalent of (a) plotted in real space showing (schematically) one electron (black dot) per atom (hollow point); an electron has been "caught in the act" of hopping from one atom to the next. (c) The band after the Peierls distortion shown in (d). The crystal has distorted, doubling the real space unit-cell size, and halving the Brillouin zone size. As new zone boundaries exist at $\pm k_F$, a band-gap opens up there, lowering the electronic energy and turning the substance into an insulator with two electrons per unit cell.

In order to underline this further we analyse the calculated density of charge shown in Fig. 5.9 and Fig. 5.10. The figures show the distribution of electronic charge in the (001)-plane of Ni for the $L2_1$ and 5M structures. In case of $L2_1$ (see Fig. 5.9) the charge is distributed around the Ni atoms equivalently for all directions (within the plane). In other words, every Ni atom is connected to its nearest Ni neighbours with same priority. In case of the 5M structure (Fig. 5.10) the charge is distributed in a different way. The Ni atoms form pairs (or dimers) and trimers. This redistribution of charge leads to a stronger coupling between the paired Ni atoms which may yield stability of the modulated structure. In fact, one can envisage the modulated structure from a different point of view. Now the modulation does not appears as a *sine*-like wave of atomic displacements, but as discrete structure formed by Ni-Ni dimers and trimers.

We expect similar distribution of charge in other atomic planes with Mn and Ga, however it has not been analyses so far. It is obvious that Mn and Ga also contribute to the whole effect of modulation. In Fig. 5.3, one can see that Ga moves always towards one of the nearest Ni atom, while Mn fills the free space, which was created after redistribution

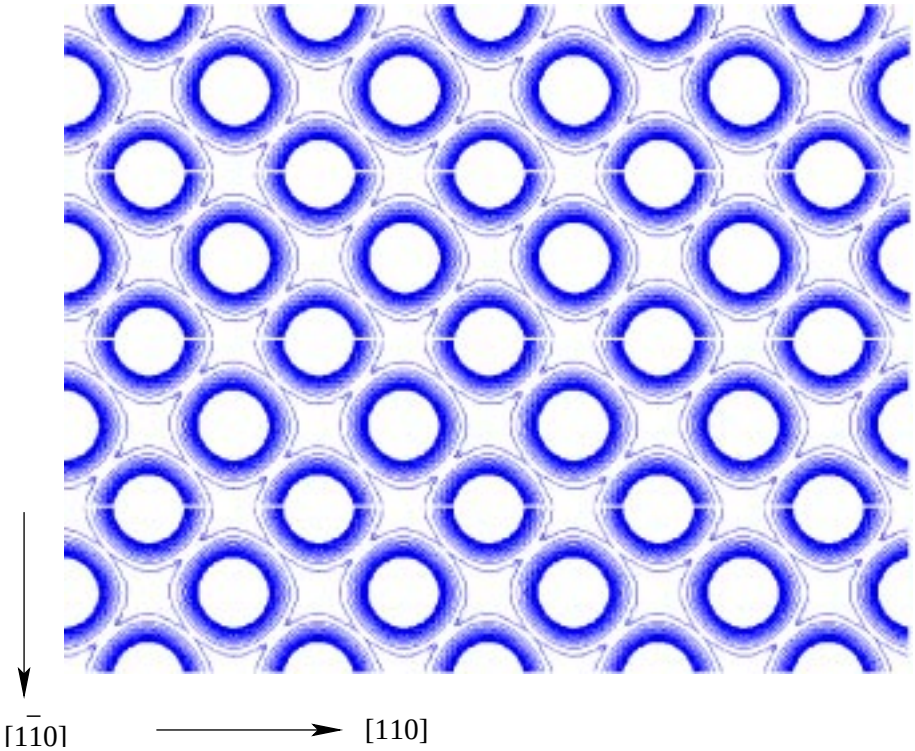

Figure 5.9: Distribution of charge in the Ni-plane of Ni_2MnGa in the $L2_1$ structure.

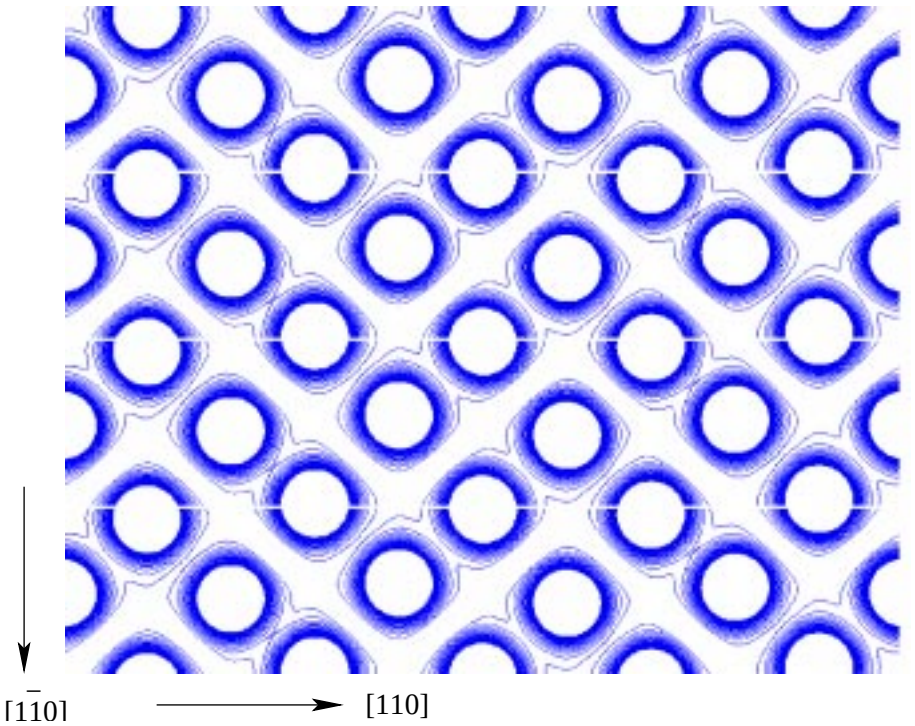

Figure 5.10: Distribution of charge in the Ni-plane of Ni_2MnGa in the 5M structure.

of Ga and Ni. Moreover, it was discussed above that Ga and Ni form hybrid states close to the Fermi level. Thus, it is expected that the picture of charge distribution shown in Fig. 5.10 must cause specific changes in the states of Ga.

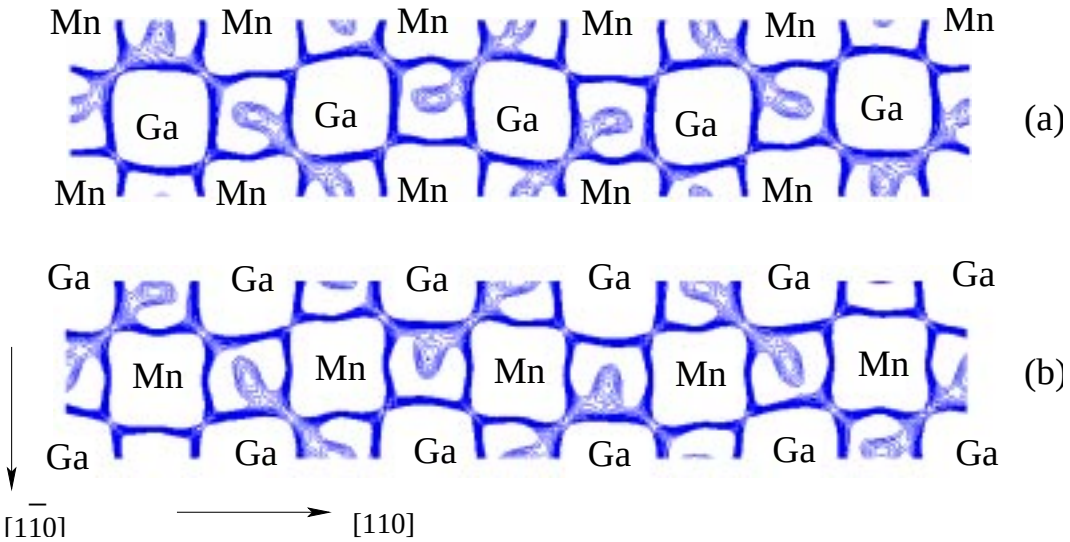

Figure 5.11: Charge transfer in the GaMn-planes of Ni_2MnGa in the 5M structure. The picture shows the result of subtracting the charge of the initial and final configurations during the process of the electronic structure relaxation.

This can be checked by analysing the redistribution of charge, which takes place when the cubic $L2_1$ structure transforms to the 5M structure. In other words, one could subtract the charges of these two structures in order to see whether the modulation causes some charge transfer in the system. Since the role of Ni-Ga coupling has been emphasized, we expect some additional charge to show up in the bonds between Ni and Ga corresponding to the hybrid states mentioned above. Unfortunately, it is practically impossible to subtract correctly the charge data of the $L2_1$ and 5M structure because the atomic positions are so different.

As an alternative we use a trick based on the computational technique of the first-principles method. In VASP package, in particular, the initial configuration of the electronic structure is constrained from the quantum-mechanical s, p and d atomic orbitals. The initial configurations for the $L2_1$ or 5M structures are almost the same. In the iteration process, at each step, the charge is redistributed according to the solution of the eigenvalue problem. One can analyse the redistribution of the charge during the convergence process to the final electronic configuration. For both structures, one can subtract the initial and the final charge data. The results can be compared in order to see whether the modulation leads to some effects which are not present in the $L2_1$ structure.

One of these effects is shown in Fig. 5.11, which displays the difference in charge between the initial and the final electronic configurations in case of the 5M structure. Two (001) planes are shown here (which are not the atomic planes). One of them, see Fig. 5.11(a) is taken 0.3 Å above the Ga-Mn plane of the 5M structure, see Fig. 5.2; the second one is 0.3 Å above the next Ga-Mn plane. The two planes are separated by a

distance of $c/2$. They are different in the sense that Ga and Mn are in different positions. The planes considered here are a bit out from the atomic planes in order to cut through the interplain bonds to Ni. The interpretation of this figure is that some charge moves from the Ga-Mn plane towards the Ni plane. Moreover, the comparison with Fig. 5.10 shows that the dimers mentioned above are related to the charge transfer shown in Fig. 5.11. This observation underlines the idea that hybrid states (see Fig. 5.6) stabilize the modulated structure.

This discussion about the 5M structure and the role of modulated shuffles in Ni_2MnGa can explain the experimental data. The calculated superstructure with modulation resembles earlier proposed experimental models and leads to the correct c/a ratio for the tetragonal martensitic structure. Also, considering the DOS allows to give a reasonable explanation for the modulation. However, the results obtained so far do not allow to conclude that the calculated 5M structure corresponds to the real structure. The 5M structure has been found to be stable (metastable compared to the structure with $c/a = 1.25$) but some other metastable configurations are possible. Thus, in earlier experimental studies of modulated structures in Ni-Mn-Al alloys (Morito and Otsuka, 1996) the 5M structure was presented by different staking sequences, rather than by a sine - like wave model which was proposed by Martynov and Kokorin (1992). In order to show that other structures can be stable as well, another modulated structure shown in Fig. 5.12, has been simulated in this work. The difference with respect to the 5M structure is that the two periods of modulation have been taken with opposite phases. A full relaxation has been performed for this structure. The result is that this structure is also metastable. It is less favourable compared to the normal 5M structure, but it is more stable than the cubic $L2_1$ structure and has a tetragonality ratio $c/a < 1$, although it has not been optimized completely. Another feature of this structure is that it includes both staking faults and wave-like shuffles. The staking appears in the middle of the structure, where the two waves with opposite phases meet each other.

Summarizing this part of the study we may say that first-principles calculations have shown for the first time that the tetragonal martensite structure of Ni_2MnGa with $c/a < 1.0$ can be stabilized by allowing for shuffles of the atoms with a well - defined period. The structural parameters obtained in the calculations are in agreement with the experimental ones (Martynov and Kokorin, 1992). The energy of the modulated structure is considerably lower compared to the energy of the $L2_1$ structure of Ni_2MnGa, which makes the theory to agree with experimental trends. A novel finding is that the amplitudes of modulation are different for Mn-Ga and Ni planes. This result would probably encourage further experimental studies, e.g., with respect to the interpretation of X-ray results. The effect of modulation is not negligible and certainly will induce further work, for example, with respect to the orthorhombic phases of Ni_2MnGa. Stability of the modulation is related to the features found in the minority-spin DOS right at E_F, namely, there is a dip in the DOS originating from Ni and Ga states, which develops when the modulation is formed.

Further work necessitates the inclusion of atomic disorder and the consideration of

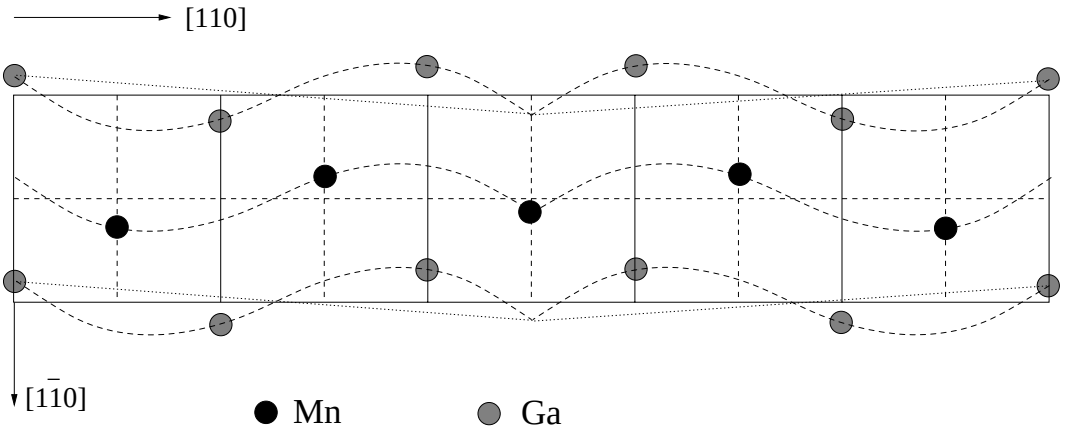

Figure 5.12: Long superstructure with two periods of modulation (like the 5M structure but with two periods in opposite phase). This structure has been found to be stable in the calculations. An interesting feature is that in the middle of the structure, where two waves with opposite phases meet each other, is a staking fault.

non-collinear magnetic structures. Here we concentrate in the following on dynamical aspects associated with the phonon properties of Ni_2MnGa. It is important that the fact of modulation can be explained in terms of nesting, but it has not been explained in the literature how far the phonons are involved in the formation of the modulation.

6 Theory of lattice dynamics

The formulation of this theory starts from the definition of an infinitely extended crystal. This theory is greately simplified by using perfect lattice periodicity and space group symmetry which results from the absence defects and of crystal surfaces (Born and Kun, 1988; Cochran, 1973; Dove, 1993; Horton and Maradudin, 1974; Srivastava, 1990).

An arbitrary Bravais lattice is defined by the lattice translational vectors

$$\mathbf{x}(l) = l_1\mathbf{a}_1 + l_2\mathbf{a}_2 + l_3\mathbf{a}_3, \tag{6.1}$$

where l_1, l_2, l_3 are arbitrary integers labeled collectively by l. The three, noncomplanar vectors $\mathbf{a}_{1,2,3}$ are the primitive translational vectors of the lattice. If there are r atoms in the basis of the lattice, the positions of these r atoms in the unit cell, with respect to the origin of the unit cell, are given by the vectors $\mathbf{x}(k)$, where the index k distinguishes the different atoms in the basis, or, equivalently, in the primitive unit cell, and takes the values $1, 2 \ldots r$. Thus, in general the position vectors of the kth atom in the lth primitive cell is given by

$$\mathbf{x}(lk) = \mathbf{x}(l) + \mathbf{x}(k). \tag{6.2}$$

The atomic positions in an infinite crystal defined by the set of vectors $\{\mathbf{x}(lk)\}$ are refered as rest positions of the atoms.

As a results of thermal fluctuations at nonzero temperatures and of zero-point motions at zero temperature the atoms in the crystal execute vibrations about their rest positions. If we denote by $p_\alpha(lk)$ the α cartesian component of the momentum of the kth atom in the lth primitive unit cell, the total kinetic energy of the crystal can be written as

$$T = \sum_{lk\alpha} p_\alpha^2(lk)/2M_k, \tag{6.3}$$

where M_k is the mass of the kth kind of atom.

We assume that the potential energy Φ of a crystal is a function of the instantaneous position of the atoms. We denote by $u_\alpha(lk)$ the α cartesian component of the displacement of the kth atom in the lth primitive unit cell from its rest position given by (6.2). The potential energy Φ can be formally expressed as a powers series of these components leading to

$$\begin{aligned}\Phi &= \Phi_0 + \sum_{lk\alpha} \Phi_\alpha(lk)u_\alpha(lk) + \frac{1}{2}\sum_{lk\alpha}\sum_{l'k'\alpha'} \Phi_{\alpha\beta}(lk;l'k')u_\alpha(lk)u_\beta(l'k') + \\ &\quad \frac{1}{6}\sum_{lk\alpha}\sum_{l'k'\alpha'}\sum_{l''k''\alpha''} \Phi_{\alpha\beta\gamma}(lk;l'k';l''k'')u_\alpha(lk)u_\beta(l'k')u_\gamma(l''k'') + \ldots\end{aligned} \tag{6.4}$$

In this expression Φ_0 is the potential energy of the static lattice, i.e., when all atoms are in their rest positions, while the expansion coefficients are

$$\Phi_\alpha(lk) = \left.\frac{\partial\Phi}{\partial u_\alpha(lk)}\right|_0, \tag{6.5}$$

$$\Phi_{\alpha\beta}(lk;l'k') = \left.\frac{\partial^2\Phi}{\partial u_\alpha(lk)\partial u_\beta(l'k')}\right|_0, \tag{6.6}$$

$$\Phi_{\alpha\beta\gamma}(lk;l'k';l''k'') = \left.\frac{\partial^3\Phi}{\partial u_\alpha(lk)\partial u_\beta(l'k')\partial u_\gamma(l''k'')}\right|_0, \text{ etc.,} \tag{6.7}$$

where the subscript 0 means that the derivatives are evaluated with all the atoms at their rest positions.

The physical interpretation of the coefficient $\Phi_\alpha(lk)$ is that it is the negative of the force in the α direction acting on the atom (lk) when it and all other atoms in the crystal are at their rest positions. Similar interpretation can be given to the higher order coefficients $\Phi_{\alpha\beta}(lk;l'k')$, $\Phi_{\alpha\beta\gamma}(lk;l'k';l''k'')$, ... Consequently, the coefficients $\Phi_\alpha(lk)$, $\Phi_{\alpha\beta}(lk;l'k')$, $\Phi_{\alpha\beta\gamma}(lk;l'k';l''k'')$, ..., are known as *atomic force constants* of the first, second, third, ..., order, respectively.

The first order atomic force constants distinguish in the case when the atoms are in their rest positions and also in the case when the rest positions are also equilibrium positions. In the latter case the whole configuration of the crystal corresponds to vanishing stress. While the rest positions imply only that there is no net force action on the atoms. For the equilibrium crystal this is a more strict definition yielding meaning that the first order atomic force constants must vanish. There are several problems of physical interest where it is necessary to consider atoms in their rest positions which are not equilibrium positions (Horton and Maradudin, 1974). One example is the study of the dynamical properties of crystals being under externally imposed stress.

It is convenient to combine the terms linear in the atomic displacements with the terms of third and higher order and to treat them as a perturbation of the contributions to the vibrational part of the energy obtained from the quadratic terms in the atomic displacements. Then, the vibrational Hamiltonian for a crystal can be written as

$$H = H_0 + H_A, \tag{6.8}$$

where

$$H_0 = \sum_{lk\alpha}\frac{p_\alpha^2(lk)}{2M_k} + \frac{1}{2}\sum_{lk\alpha}\sum_{l'k'\alpha'}\Phi_{\alpha\beta}(lk;l'k')u_\alpha(lk)u_\beta(l'k'), \tag{6.9}$$

$$H_A = \sum_{lk\alpha}\Phi_\alpha(lk)u_\alpha(lk) + \frac{1}{6}\sum_{lk\alpha}\sum_{l'k'\alpha'}\sum_{l''k''\alpha''}\Phi_{\alpha\beta\gamma}(lk;l'k';l''k'')u_\alpha(lk)u_\beta(l'k')u_\gamma(l''k'') + \ldots \tag{6.10}$$

The Hamiltonian H_0 is the vibrational hamiltonian in the *harmonic approximation*. The Hamiltonian H_A is called the *anharmonic* part of the vibrational Hamiltonian. In many crystals the anharmonic terms in the crystal potential energy are small and can be treated as a perturbation of the harmonic Hamiltonian; in some cases the anharmonic effects are so negligibly small so that they can be left out from the consideration. A great advantage is that in the harmonic approximation, the equations of motion of the atoms become simple and are somethimes exactly solvable.

From the Hamiltonian (6.9) and Hamilton's equations of motion

$$\dot{u}_\alpha = \partial H_0/\partial p_\alpha(lk) = p_\alpha(lk)/M_k, \tag{6.11}$$

$$\dot{p}_\alpha = -\partial H_0/\partial u_\alpha(lk) = -\sum_{l'k'\beta} \Phi_{\alpha\beta}(lk;l'k')u_\beta(l'k'), \tag{6.12}$$

the equation of motion of a crystal reads

$$M_k\ddot{u}_\alpha(lk) = -\sum_{l'k'\beta} \Phi_{\alpha\beta}(lk;l'k')u_\beta(l'k'). \tag{6.13}$$

A solution of this set of coupled equations can be obtained in a lattice-periodic form, because, in this case it will satisfy the symmetry conditions (Horton and Maradudin, 1974) leading

$$u_\alpha(lk) = M_k^{-1/2} e_\alpha(k) \exp\left(\imath\mathbf{k}\cdot\mathbf{x}(l) - \imath\omega t\right). \tag{6.14}$$

The coefficient function $e_\alpha(k)$ satinsies the equation

$$\omega^2 e_\alpha(k) = \sum_{k'\beta} D_{\alpha\beta}(kk';\mathbf{k})e_\beta(k'), \tag{6.15}$$

which is obtained by substituting the second derivative of (6.14) into the equation of motion (6.13). The matrix $D_{\alpha\beta}$ is defined by the equation

$$D_{\alpha\beta}(kk';\mathbf{k}) = (M_kM_{k'})^{-1/2} \sum_{l'} \Phi_{\alpha\beta}(lk;l'k') \exp\left(-\imath\mathbf{k}[\mathbf{x}(l) - \mathbf{x}(l')]\right). \tag{6.16}$$

In the equation (6.15), there is no dependence on the cell index l. Since the atomic force constants depend only on the relative distances between the atoms, the origin l does not play a role anymore and can be set equal to 0. The matrix $D_{\alpha\beta}(kk';\mathbf{k})$ is called the *dynamical matrix* of the crystal. It is $3r \times 3r$ hermitian matrix (r is the number of atoms in the unit cell) with the properties

$$D_{\alpha\beta}(kk';\mathbf{k}) = D_{\beta\alpha}(k'k;\mathbf{k}), \tag{6.17}$$

$$D_{\alpha\beta}(kk';-\mathbf{k}) = D^*_{\alpha\beta}(kk';\mathbf{k}). \tag{6.18}$$

It follows from (6.15) that the allowed values of the squares of the frequency ω for a given value of $\mathbf{k}$ are the eigenvalues of the dynamical matrix $D_{\alpha\beta}(kk';\mathbf{k})$. Because the

latter is a $3r \times 3r$ matrix there are $3r$ solutions for ω^2 for each value of $\mathbf{k}$, i.e., the values $\omega_j^2(\mathbf{k})$, where $j = 1, 2, 3, \ldots, 3r$. The $3r$ functions $\omega_j^2(\mathbf{k})$ for each value of $\mathbf{k}$ can be regarded as the branches of the phonon dispersion. From the hermicity of the dynamical matrix it follows that $\omega_j^2(\mathbf{k})$ is real. Stability of the crystal implies that $\omega_j(\mathbf{k})$ must be also real. An imaginary frequency corresponds to atomic motions which are not harmonic having amplitudes given by (6.14) which grow exponentially with time. This means that stability requires that $\omega_j^2(\mathbf{k})$ is not only real, but also positive.

For each of the $3r$ values of $\omega_j^2(\mathbf{k})$ corresponding to a given value of $\mathbf{k}$ there exists a $3r$-component vector $e_\alpha(k)$, whose components are the solutions to the set of equations (6.15). To make it clear that this vector depends on the given value of $\mathbf{k}$ and is associated with the particular phonon branch j, it can be rewritten as $e_\alpha(k; \mathbf{k}j)$. The equation (6.15) reads then

$$\omega_j^2(\mathbf{k}) e_\alpha(k; \mathbf{k}j) = \sum_{k'\beta} D_{\alpha\beta}(kk'; \mathbf{k}) e_\beta(k'; \mathbf{k}j). \tag{6.19}$$

From the conditions imposed on the atomic force constants by the invariance of the potential energy and its derivatives against an infinitestimal rigid body displacement of the whole crystal (Horton and Maradudin, 1974) follows that the frequencies of three branches of $\omega_j(\mathbf{k})$ $(j = 1, 2, 3)$ vanish with vanishing $\mathbf{k}$ and the corresponding eigenvectors have the property that $e_\alpha(k; \mathbf{k} = \mathbf{0}, j)/\sqrt{M_k}$ is independent of k, i.e., the same for all atoms. These three branches are called *acoustic* branches, because in the long wavelength limit they give the frequency of sound waves propagating through the crystal. The remaining $3r - 3$ branches, whose frequencies approach nonzero values as $\mathbf{k}$ tends to zero, are called *optical* branches, because these branches are observed in infrared absorbtion and light scattering experiments in the limit $\mathbf{k} \to \mathbf{0}$.

The displacement pattern obtained by substituting into (6.14) a particular eigenvector $e_\alpha(\mathbf{k}j)$ and the corresponding frequency $\omega_j(\mathbf{k})$,

$$u_\alpha(lk) = \frac{1}{\sqrt{M_k}} e_\alpha(k; \mathbf{k}j) \exp\left[\imath \mathbf{k} \cdot \mathbf{x}(l) - \imath \omega_j(\mathbf{k}) t\right], \tag{6.20}$$

is called a *normal mode* of the crystal described by the wave vector $\mathbf{k}$ and branch index j.

6.1 Phonon calculation by *ab-initio* methods

The *linear-responce* method allows to expres the dynamical matrix in terms of the inverse dielectric matrix describing the responce of the valence electron density to a periodic lattice perturbation (Schütt, Pavone, Windl, Karch *et al.*, 1994). The *frozen phonons* method allows the calculation of phonon energy as a function of the displacement amplitude in terms of the difference in energies of distorted and ideal lattices (King-Smith and Needs, 1990). This approach is restricted to phonons, whose wavelength is compatible with the periodic boundary conditions applied to the supercell used in calculations. Another alternative is to use a direct approach to calculate the phonon dispersion using an *ab-initio* force constant method which we have employed in this work (Kunc and Martin, 1982).

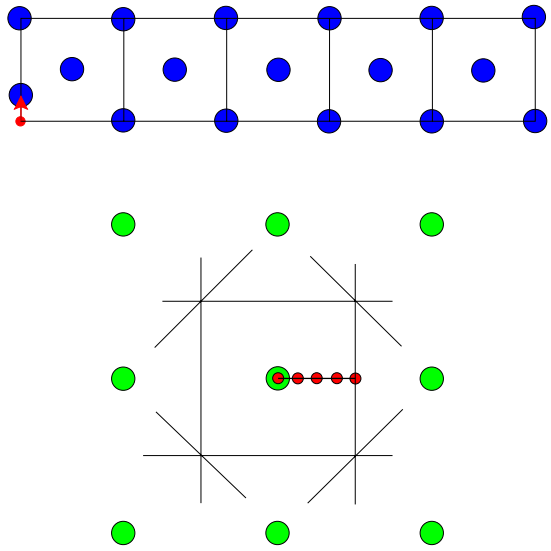

Figure 6.1: Schematic illustration of a supercell used in the direct method for calculating phonons. The longer supercell is taken for calculating the force constants; the marked $\mathbf{k}_L$-points in the Brillouin zone yield exact phonons frequencies. The elongated supercell is constructed from several crystal unit cells. Atoms from only one unit cell must be displaced in corresponding directions in order to obtain all atomic force constants.

6.2 Direct *ab-initio* force constant method

A general formulation of the direct *ab-initio* force constant method has been proposed by Parlinski *et al.* (1997). Usually this method is referred to as *direct* method. This method uses the forces calculated via the Hellmann-Feynman theorem in the total energy calculations. The calculations are done on a supercell with periodic boundary conditions. In such a supercell, a displacement $\mathbf{u}(0,k)$ of a single atom induces forces $\mathbf{F}(lk)$ acting on all other atoms (Parlinski, Li and Kawazoe, 1997),

$$F_\alpha(lk) = -\sum_{l'k'\beta} \Phi_{\alpha\beta}(lk;l'k') \cdot u_\beta(l'k'). \tag{6.21}$$

Ths expression allows to determine the force constant matrix directly from the calculated forces. In principle, in order to obtain the complete information of the values of all force constants, every atom of the primitive unit cell should be displaced and corresponding forces calculated. However, the crystal symmetry allowes to reduce considerably the number of necessary displacements. First, displacements of equivalent atoms lead to the same result, therefore, it is sufficient to displace single non-equivalent atoms only. The non-equivalent atom must be defined with respect to the atom kind and the space group symmetry of the supercell.

Generally, atoms should be displaced along three non-complanar directions, however, the site symmetry, which follows from the supercell space group symmetry, reduces the number of displacements. If the site group is cubic a displacement along a single fourth-fold axis is sufficient to reproduce the others by symmetry operations. If the site point group is tetragonal, the displacements should be taken along the fourth-fold symmetry axis and another one perpendicularly to this axis plane. Lower site point groups require three independent displacements (Parlinski, 2002).

The calculation of vibrational properties starts from a total optimization of the crystal with respect to the electronic part, lattice constants and atomic positions. Such optimiza-

tion should be carried out by using a quantum-mechanical first-principle program, which is able to define a stable configuration of the supercell and which allows to find the Hellmann-Feynman forces. In the optimized state, all the forces must vanish.

The phonon dispersion branches calculated by the direct method are exact for discrete wave vectors defined by the equation

$$\exp\left(2\pi\imath\mathbf{k}_L \cdot \mathbf{L}\right) = 1, \tag{6.22}$$

where $\mathbf{L} = (L_a, L_b, L_c)$ are lattice parameters of the supercell. Usually, the $\mathbf{k}_L$ wave vectors correspond to high-symmetry points of the Brillouin zone. Increase of the supercell size increases the density of the wave vector grid $\mathbf{k}_L$. In this case better accuracy of the phonon dispersion curves is achieved. The direct method implies that the dispersion curves between the exact points can be interpolated. The precision of such interpolation depends on how far the long range forces propogate in the crystal. If the forces converge to zero within a short distance (within the considered supercell), the presision of the phonons for $\mathbf{k} \neq \mathbf{k}_L$ is high. In the case of very long range interaction, the deviation from the correct solution can increase.

From the equation of motion (6.15) one can deduce the influence of the supercell size. The greater the range of the interatomic forces are the greater are the number of terms in the Fourier series in (6.15) for $\omega^2(\mathbf{k})$. So, in order to obtain accurate phonon dispersion curves for a crystal, one has to take care about the size of the supercell and the quality of the calculated Hellmann-Feynman forces. Usually, in order to obtain precise phonons along a desired direction, the calculations are carried out with elongated supercells. After all necessary atoms k have been displaced, the corresponding Hellmann-Feynman forces $F_\alpha(lk)$, the force constant matrix $\Phi_{\alpha\beta}(lk; l'k')$ and the dynamical matrix can be obtained according to (6.16). Diagonalization of the dynamical matrix yields for every value of $\mathbf{k}$ a number of eigenvalues for $\omega^2(\mathbf{k}, j)$ and corresponding polarization vectors $\mathbf{e}(\mathbf{k}, j)$.

7 Determination of phonon dispersions

It is a matter of fact that the static lattice approach, which is concerned with the average positions of atoms and neglects their motions, can describe a large number of crystalline properties. The electronic structure calculations are fairly successful in the framework of the adiabatic approximation. However, a number of properties cannot be explained by the static lattice model (Dove, 1993). These include:

- thermal properties, e.g., heat capacity;
- effects of the temperature on the lattice, e.g., thermal expansion;
- structural stability, the existence of phase transformations, including melting;
- transport properties, e.g., thermal conductivity, sound propagation;
- the existence of fluctuations, e.g., the temperature factor;
- certain electrical properties, first of all superconductivity;
- dielectric phenomena at low frequency;
- interaction of radiation (light, thermal neutrons) with matter.

This is why, the determination of phonons of a crystalline structure has always been a fundamental problem of physics.

Experimentally, the phonon dispersion curves can be measured by means of neutron scattering. Beams of neutrons scattered by matter turn out to have very suitable properties for phonon experiments (Dove, 1993). The mass of the neutron (1.675×10^{-27} kg) is of the same order as the mass of a nucleus. Hence the neutrons can be scattered elastically (no change in energy) inelastically (with energy change) by the nuclei. The wave length of a neutron beam is typically in the range $\sim$ 1-5 Å which fits well to the unit cell length providing a good resolution for measurements. Thermal neutrons have energies of up to $\sim$ 100 meV, which are similar to phonon energies. The electrostatic charge of the neutron is zero, which implies that the neutron does not interact with the electrons in matter via electrostatic forces. The neutron has a magnetic moment, which arises from the internal quark substructure of the neutron. Therefore, the neutron is able to interact with the magnetic moments of the atoms inside the crystal. In contrast to X-rays, the neutron beams experience a very low adsorbtion in matter. In fact neutron scattering is the only available technique for measuring all phonon dispersion curves across the whole Brillouin zone.

Infrared spectroscopy and Raman scattering are other methods of measuring phonon frequencies which are complementary to neutron scattering. Having zero rest mass, photons do not scatter from phonons in the same way as neutrons do. The photons can be scattered either by absorbing or creating a single phonon. In the first case, measurements involve shining a polychromatic beam of radiation onto the sample, and measuring the

frequencies at which adsorbtion occurs. These are typically in the infrared region of the electromagnetic spectrum, hence this technique is known as *infrared spectroscopy*. In the case when the photon creates a single phonon the scattering is called *Raman scattering*, named after one of its experimental discoverers.

In addition to the experimental techniques, recent advances in numerical methods and computational capability are driving attempts to perform accurate phonon calculations. The *ab-initio* based methods described above provide a fairly reliable alternative to the experimental measurements. In this study the direct force constant method is used to evaluate phonon dispersion curves for Ni_2MnGa.

7.1 Calculation of Hellmann-Feynman forces

In this study phonon dispersion curves are calculated by using the PHONON package developed by K. Parlinski (Parlinski, 2002; Parlinski, Li and Kawazoe, 1997). It has been designed to use input data of Hellmann-Feynman forces calculated with the help of an *ab-initio* electronic structure simulation program.

At the first step of the calculation, the PHONON package is used to define the appropriate crystal supercell for use of the direct method. The PHONON package helps to analyse this supercell by giving information about a minimum number of atomic displacements, for which the Hellmann-Feynman forces must be calculated using the *ab-initio* software. The Hellmann-Feynman forces are then used for the phonon calculations according to the formalism of the direct method, which has been discussed above.

In our case an orthorhombic $1 \times 5 \times 1$ supercell of 40 atoms formed by five tetragonal unit cells is used for the evaluation of the phonon spectrum. This supercell, shown in Fig. 5.1(c), is elongated in [110] direction allowing a very accurate calculation of the phonon spectrum in this direction. The elongation of the supercell provides more terms in the Fourier series of the Eq.(6.15) yielding at the same time five exact points $\mathbf{k}_L$ in [110] direction as shown in Fig. 6.1. Lattice parameters of the supercell are related to those of the cubic $L2_1$ structure as follows: $a_{\text{orth}} = (1/\sqrt{2})a_{\text{cubic}}$, $b_{\text{orth}} = (5/\sqrt{2})a_{\text{cubic}}$, $c_{\text{orth}} = a_{\text{cubic}}$; the equilibrium lattice parameter obtained by using VASP is $a_{\text{cubic}} = 5.8067$ Å (see Fig. 4.1) which agrees with the experimental value (Webster, Ziebeck, Town and Peak, 1984). The direction $[010]_{\text{orth}}$ of the supercell corresponds to the direction $[110]_{\text{cubic}}$ of the cubic $L2_1$ structure. This is the direction along which the phonon dispersions measured by inelastic neutron scattering revealed a soft TA_2 phonon mode (Mañosa Ll., Gonzalez-Comas, Obrado, Planes *et al.*, 1997; Mañosa Lluis, Planes, Zarestky, Lograsso *et al.*, 2001; Zheludev and Shapiro, 1996; Zheludev, Shapiro, Wochner, Schwartz *et al.*, 1995; Zheludev, Shapiro, Wochner and Tanner, 1996).

It is worth to repeat that the direct method implies that we calculate forces induced on all atoms of the supercell when a single atom is displaced from its equilibrium position. For the current case, i.e., the $L2_1$ structure presented by the long orthorhombic supercell (Fig. 5.1), displacements of three inequivalent atoms (Ga, Mn and Ni) are needed to obtain all atomic force constants. Each of these atoms must be displaced along three axes if the Cartesian coordinates. This implies that nine independent electronic struc-

Table 7.1: Table of irreducible representations of the supercell point group D_{2h} (mmm).

IR	1	4	3	2	25	28	27	26	
A_g(R)	1	1	1	1	1	1	1	1	x^2, y^2, z^2
B_{1g}(R)	1	1	-1	-1	1	1	-1	-1	xy
B_{2g}(R)	1	-1	1	-1	1	-1	1	-1	xz
B_{3g}(R)	1	-1	-1	1	1	-1	-1	1	yz
A_u	1	1	1	1	-1	-1	-1	-1	
B_{1u}(I)	1	1	-1	-1	-1	-1	1	1	z
B_{2u}(I)	1	-1	1	-1	-1	1	-1	1	y
B_{3u}(I)	1	-1	-1	1	-1	1	1	-1	x

Table 7.2: The list of atoms with corresponding displacements which have been used to calculate the force constants. The coordinates are given in units of the lattice parameters of the original tetragonal cell (*fractional coordinates*).

Configuration	Atom positions			Displacement (Å)		
1	0.00	3.00	0.00	0.03	0.00	0.00
2	0.00	3.00	0.00	0.00	0.03	0.00
3	0.00	3.00	0.00	0.00	0.00	0.03
4	0.00	3.50	0.75	0.03	0.00	0.00
5	0.00	3.50	0.75	0.00	0.03	0.00
6	0.00	3.50	0.75	0.00	0.00	0.03
7	0.00	3.00	0.50	0.03	0.00	0.00
8	0.00	3.00	0.50	0.00	0.03	0.00
9	0.00	3.00	0.50	0.00	0.00	0.03

ture calculations must be performed which finally give the Hellmann-Feynman forces. Diagonalization of the resulting dynamical matrix leads then to a set of eigenvalues for the phonon frequencies and corresponding eigenvectors. The calculations have to be done with an appropriate amplitude for the atomic displacements which in our case is taken to be $u = 0.03$ Å. This value is sufficiently small to yield the forces with required precision and to fulfil the conditions of the harmonic approximation we are using here. Before starting the calculations, the undisturbed structure of the supercell has to be optimized with respect to its volume, shape and positions of the atoms to ensure that no forces act on the atoms and that the supercell is not subject to the stress.

The symmetry of the supercell is given by the point group D_{2h} (mmm) which is characterized by the irreducible representations listed in Table 7.1.
The corresponding atomic displacements which are needed in order to calculate the phonon dispersions are listed in Table 7.2. The symmetry analysis allows to reduce the number of calculations to a minimum. The table gives the fractional coordinates of the displaced atom for each configuration, which are defined with respect to the principal tetragonal cell.

The electronic structure calculations, whereby the Hellmann-Feynman (HF) forces are obtained, are carried out with VASP (Kresse and Furthmüller, 1996; Kresse and Joubert, 1999) and the implemented projector-augmented wave formalism (PAW) (Blöchl, 1994). Within density functional theory, the electronic exchange and correlation are treated by using the generalised gradient approximation, GGA. In the calculations, the $3d$ electrons of Ga have been included as valence states. A plane-wave cutoff energy of 353.4 eV and a Monkhorst-Pack k-points generation scheme is used with a grid of $10 \times 8 \times 2$ points in the full Brillouin zone for the long orthorhombic supercell.

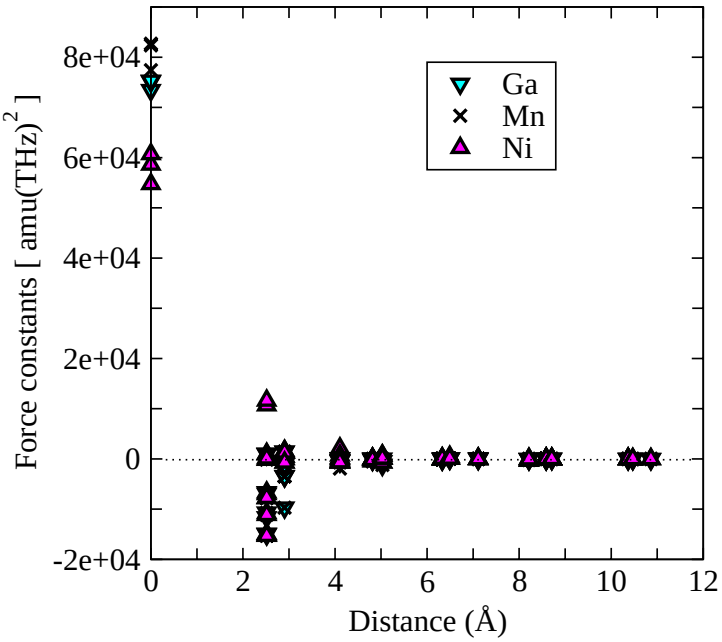

Figure 7.1: Dependence of the interatomic forces in Ni_2MnGa on the distance in [110] direction. The behaviour of these forces is an important criteria for the direct method. Only, if the forces converge to zero within the length of the supercell, the calculated phonons are correct (Parlinski, 2002). This plot shows that the calculated forces in case of Ni_2MnGa meet this criteria fairly well.

After all HF forces have been obtained from the electronic structure calculations, the atomic force constants are calculated. The latter must satisfy certain conditions in order to provide accurate phonon dispersion curves. One of these conditions is that the chosen supercell is large enough to accommodate the essential long-range interactions. In a perfect situation, a central atom of the supercell should not feel any force caused by a single displacement of another atom being at the boundary of the supercell. In other words, the forces caused by the atomic displacements must converge to zero within the half length of the supercell. Figure 7.1 presents a plot of the change of atomic force constants with the distance in the supercell along the [110] direction. Certainly, one can see that the current calculation fulfils the condition for the forces for all three inequivalent atoms, which means that the calculated phonon dispersion curves will be very accurate. The subsequent diagonalization of the the dynamical matrix will provide the phonon energies and corresponding polarization vectors. With respect to the polarization vectors, one cannot obtain directly the associated physical amplitudes since this information is not available within the harmonic approximation. The polarization vector $\mathbf{e}(k;\mathbf{k}j)$ give only the direction in which each atom moves and the relative amplitudes of the atomic displacements obeying the normalization condition for each $\mathbf{k}$ vector and phonon mode,

that

$$\sum_k |\mathbf{e}(k;\mathbf{k}j)|^2 = 1, \tag{7.1}$$

i.e., the sum over all atoms is 1.

7.2 Phonons and related properties of the cubic $L2_1$ structure

The phonon dispersion curves calculated for Ni_2MnGa in $[110]_{\text{cubic}}$ direction are shown in Fig. 7.2. According to the geometry of the supercell the phonon energies are exact at $\zeta = 0$ (Γ), $\zeta = 1.0$ (X) and three points in between: $\zeta = 1/4, 1/2, 3/4$. The phonon dispersion curves between these exact points are obtained from an appropriate interpolation scheme. There are no experimental data available for the optical phonon modes of Ni_2MnGa, only the acoustic modes have been measured. A comparison shows qualitative and quantitative agreement with the experimental results obtained from inelastic neutron scattering (Zheludev, Shapiro, Wochner and Tanner, 1996). For instance, following the acoustic branch, the value of the TA_2 mode at $\zeta = 1$, the value at crossing of LA and TA_1 branches and the position of maximum of the LA branch are 2.33, 4.43 and 5.13 THz, respectively, in good agreement with the experimental values, 2.67, 4.35 and 5.07 THz. The slopes of the acoustical branches for $\zeta \to 0$ allow to estimate corresponding longitudinal and transverse ultrasound velocities (for the sound propagating in the [110] direction). Table 7.2 in comparison with some experimental data. The Table 7.2 shows that the calculated and measured values of the velocities are in a very good agreement.

Table 7.3: Experimental and theoretical values of the ultrasound velocities (propagating in the [110] direction) of Ni_2MnGa. The experimental values were measured by means of inelastic neutron scattering by Worgull *et al.* (1996); Zheludev *et al.* (1996). The theoretical values have been obtained from the initial slopes of the acoustic phonon branches at $\zeta \to 0$.

$\times 10^5$ cm/s	Experiment[a]	Experiment[b]	Theory
v_{L}	5.4	5.54	5.23
v_{TA_1}	3.5	3.56	3.35
v_{TA_2}	1.0	0.74	1.02

[a](Zheludev, Shapiro, Wochner and Tanner, 1996)
[b](Worgull, Petti and Trivisonno, 1996)

The most important feature of the calculated phonon spectrum is connected with the complete softening of the transverse acoustic [110]-TA_2 mode at around $\zeta = 0.3$. In the range between $\zeta = 0.2$ and $\zeta = 0.5$ the frequency of this mode is imaginary. In the experiment by Zheludev *et al.* (1996), the softening of the [110]-TA_2 mode is incomplete. It develops a deepest minimum at $T = T_{\text{P}} = 260$ K (where T_{P} is the premartensitic transition temperature), whereby the lowest frequency of the soft mode reaches a value of about 0.2 THz. At lower temperatures, $T < T_{\text{P}}$, the measured phonon mode indicates that

the crystal structure is different from the parent $L2_1$ structure. As a characteristic feature a stiffening of the [110]-TA_2 phonon mode with decreasing temperature is observed in the experiment. Our results show that because of the soft mode in the phonon dispersion the high-temperature $L2_1$ phase is instable at low temperatures.

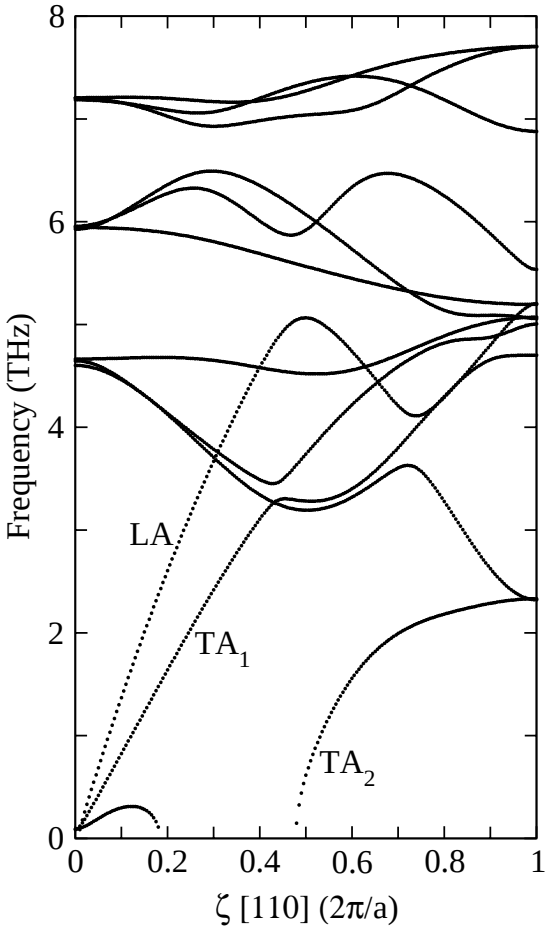

Figure 7.2: Calculated phonon dispersion curves for the cubic $L2_1$ structure of Ni_2MnGa. The reduced wave vector coordinate ζ spans the fcc BZ from Γ to X. Symmetry of each phonon band is given in Table 7.4.

The symmetry of the phonon modes presented in Fig. 7.2 is characterized by the point group of the supercell (see irreducible representations listed in Table 7.1). A list of phonon bands at the Γ point is given in Table 7.4 together with corresponding symmetry representations.

It is important to note that in the limit $\zeta \to 0$ the TA_2 phonon mode corresponds to the elastic shear constant $C' = \frac{1}{2}(C_{11} - C_{12})$. The value of C' is known to soften dramaticaly in the vicinity of the premartensitic transition temperature $T_P = 260$ K (Worgull, Petti and Trivisonno, 1996). The value of the wave vector has also a particular meaning here. Namely, the softening occurs around $\zeta = 1/3$. It corresponds to the phonon anomaly observed before in the experimental studies (Zheludev, Shapiro, Wochner and Tanner, 1996), but at the same time, the experimentally observed premartensitic structure is modulated by a well defined period characterized by $\zeta = 1/3$. The premartensitic transition is related to this soft mode which is reproduced in our first-principles calculations.

Table 7.4: The list of phonon frequencies at Γ with corresponding irreducible representations. In the case of acoustic bands the values of frequency are slightly different from zero because of the numerical procedure used here (correct zero values are given in brackets).

Multiplicity	Omega (THz)	Irreducible representation
1	-0.110 (0.0)	B_{2u}(I)
2	0.091 (0.0)	B_{1u}(I) + B_{3u}(I)
1	4.602	A_g(R)
1	4.647	B_{3g}(R)
1	4.664	B_{2g}(R)
1	5.927	B_{1u}(I)
1	5.945	B_{3u}(I)
1	5.956	B_{2u}(I)
1	7.186	B_{1u}(I)
2	7.207	B_{2u}(I) + B_{3u}(I)

The formation of the modulated premartensitic structure is responsible for the stiffening of the [110]-TA_2 phonon mode for $T < 260$ K. Further, at lower temperatures the premartensitic modulated structure will be replaced by the 5M or 7M. The impact of temperature is of principal importance here. Although finite-temperature *ab initio* calculations are beyond present days computer capabilities we may tentatively conclude from the zero temperature calculations that the particular kind of modulation observed in the martensitic phases of Ni_2MnGa can be identified with the displacements associated with the premartensitic transition at finite temperatures in the experiment. The the question is whether we can also reproduce the premartensitic 3M structure by first-principles calculations as well. We expect that the 3M strcture must be metastable at zero temperature with respect to the modulated martensitic 5M structure because of the experimentally obtained sequence of the phase transitions with decreasing temperature in Ni_2MnGa.

The instability of the cubic $L2_1$ structure at zero temperature is possibly the clue to understand how the martensite phase may nucleate. Instead of twinning and stacking faults, the modulation of the tetragonal martensitic structure of Ni_2MnGa corresponds to a smaller structural change easier to accommodate or to derive from the parent cubic structure. With respect to the electronic structure, the lowering of the symmetry allows for a splitting of the DOS at E_F (see Fig. 5.6), thereby decreasing the valence band energy contribution to the total energy. Thus, structural modulation and lowering of the electronic energy may explain both the 3M and 5M structures of Ni_2MnGa.

The transformation mechanism from the unstable $L2_1$ to the metastable 3M structure can be analysed on the basis of the behaviour of the polarisation vectors. Namely, polarization vectors of the soft [110]-TA_2 phonon mode show in which direction atoms move when this structural transformation takes place. A problem arises from the fact that the harmonic approximation used here does not allow to estimate the actual distances of the atomic diplacements. Another problem associated with the [110]-TA_2 mode is that it is imaginary for the corresponding $L2_1 \leftrightarrow$ 3M transition, which means that the physical

interpretation becomes difficult in this case. However, we may tentatively analyse the pattern of atomic displacements which yield the phase transfromation.

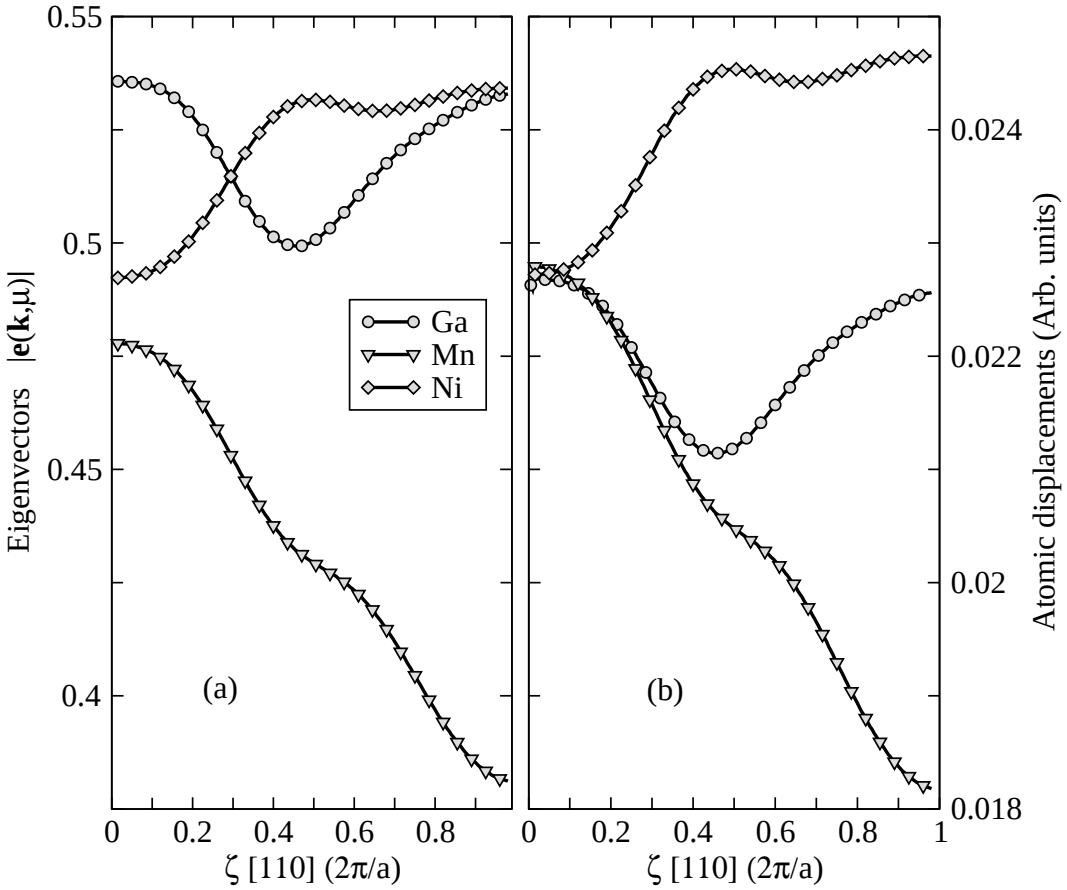

Figure 7.3: Eigenvectors and atomic displacements of the TA_2 phonon mode of Ni_2MnGa in the $L2_1$ structure.

The dispersion of polarization vectors related to the soft TA_2 mode is shown in Fig. 7.3(a). There are three different curves which correspond to three inequivalent atoms in the unit cell: Ga, Mn and Ni. We find that the polarization of this mode is in perfect agreement with what can be deduced from experiments: The atoms move strictly in one direction along the $[1\bar{1}0]_{\text{cubic}}$ direction, which is the x component of the eigenvectors in our case (the y and z components of the eigenvectors are zero). Remarkable is that for $\zeta \approx \frac{1}{3}$, the polarisation vectors of Ni and Ga show cooperative behaviour, which can be taken as a hint for a particular phonon softening. The dispersion curves of the polarization vectors for both kinds of atoms cross each other. Hence, for $\zeta \approx \frac{1}{3}$ the polarisation vectors of Ni and Ga have the same magnitude, which can lead to a kind of resonance behaviour. At the same time the polarization curve for Mn is also affected because of its inflection close to $\zeta = 0.4$.

From the polarization vectors, one can calculate corresponding atomic displacements using the expression (6.20). Figure 7.3(b) shows the atomic displacements for Ga, Mn

and Ni derived from the [110]-TA_2 mode, which exhibits the softening. Because of the harmonic approximation used here, the absolute values of the displacements cannot be obtained, but directions and relative amplitudes are correct. It is obvious from Fig. 7.3b that the atoms move with the same ampliude for $\zeta \to 0$. This means that the cubic structure is atable against distortion with $\mathbf{k} = 0$. If one atom is moved from its rest position, the whole crystal will move in the same direction with the same distance. However, with increasing ζ the atoms tend to rearrange themselves. The Ni atoms move more from their rest positions than Ga and Mn do. The Ga and Ni atoms seem to move in such a way as if they would be coupled. This is an interesting phenomenon which is still to be explained in further studies. Again the role of the Ni-Ga coupling discussed above shows up but this time in the calculation of the phonon dispersion curves. The coupling of Ni and Ga seems to be generally associated with the appearance of the soft mode and related acoustic distortions. One has tried to determine the 3M structure from experiment (see introduction), but the resulting structure disagrees with the present calculations. The 3M structure obtained by Brown *et al.* (2002) corresponds to the case if a value of ≈ 0.0227 is taken from the data in Fig. 7.3(b).

The 3M structure has been recently calculated by Andres Ayuela in (Zayak, Entel, Enkovaara, Ayuela *et al.*, 2003b). It has the same parameters of modulation as predicted by the present phonon calculations. All atoms move in the same direction (with the same phase). The period of modulation for that structure equals exactly three bct-lattice spacings, which corresponds to $\zeta = 1/3$. This is already the second modulated structure obtained for Ni_2MnGa. The only structure which is still to be found is the 7M structure (see Table 2.1).

Table 7.5: Experimental and theoretical values of the elastic constants of Ni_2MnGa. The experimental values were obtained from the ultrasonic pulse echo measurements (Vasil'ev, Kokorin, Savchenko and Chernenko, 1990; Worgull, Petti and Trivisonno, 1996). The theoretical values have been obtained from the sound velocities listed in Table 7.2.

	C_L	C_{44}	C'	C_{11}	C_{12}
			$\times 10^{12}$ dyn/cm^2		
Theory	2.22	0.91	0.084	1.394	1.226
Experiment[a]	2.50	1.03	0.045	1.52	1.43
Experiment[b]	2.42	0.92	0.63	2.13	0.87
Experiment[c]	2.48	0.98	0.065	1.56	1.43

[a](Worgull, Petti and Trivisonno, 1996)
[b](Vasil'ev, Kokorin, Savchenko and Chernenko, 1990)
[c](Stenger and Trivisonno, 1998)

The calculated from the phonon dispersion curves velocities for the ultrasound propagating in [110] direction are associated with the three independent elastic constants $C_L = \frac{1}{2}(C_{11} + C_{12} + 2C_{44})$, C_{44} and $C' = \frac{1}{2}(C_{11} - C_{12})$ related to the fact that they can be directly measured in experiments and can be used to characterise the structural stability

of a crystal. Using the density of $\rho = 8.13$ g/cm^3 for Ni_2MnGa the elastic constants can be calculated from the relations (Worgull, Petti and Trivisonno, 1996):

$$v_{\mathrm{L}} = \left(\frac{C_{\mathrm{L}}}{\rho}\right)^{1/2}, \qquad v_{44} = \left(\frac{C_{44}}{\rho}\right)^{1/2}, \qquad v' = \left(\frac{C'}{\rho}\right)^{1/2}. \tag{7.2}$$

Table 7.2 lists the theoretical elastic constants obtained from the phonon dispersion curves and the experimental values obtained from ultrasonic pulse echo technique measurements (Worgull, Petti and Trivisonno, 1996). One can see that the phonon calculations provide fairly good egreement with experiment. Moreover, the best agreement with respect to the sound velocities (Table 7.2) is connected with the experimental data obtained from the neutron measurements by Zheludev *et al.* (1996), which is believed to be the most accurate result.

7.2.1 Acoustic-optical coupling

We have considered so far only the acoustic mode TA_2, because this mode is responsible for the phase transformation $L2_1 \rightarrow 3M$. However, it is obvious from Fig. 7.2 that the other two acoustic modes, TA_1 and LA, are coupled to the low-lying optical modes.

The coupling of different phonon modes is restricted by their symmetry. Any phonon mode has a certain symmetry, which includes the symmetry operations which are not removed by the vibration. In another way of saying, each vibrational mode corresponds to a single irreducible representation of the point group of the particular wave vector. The main effect of symmetry is that vibrations of the same symmetry can interact, while those of different symmetry cannot. This means that the displacements patterns of two modes of the same symmetry can mix (implying that one cannot identify a unique displacement pattern of a mode if another mode of the same symmetry exists). This means also that two modes with of the same symmetry cannot have crossing dispersion curves. Instead of crossing, two modes will tend to cross but will in fact "repel" as they energetically approach each other. This effect is known as *anti-crossing* (Dove, 1993).

Figure 7.4 shows several anti-crossings which appear when the acoustic modes TA_1 and LA approach the low-energy optical modes. The optical modes in Fig. 7.2 form three groups with three branches in each of the groups. One of the groups has relatively low frequencies. Analysis of the polarization vectors shows that this low-lying optical modes are mainly derived from Ni vibration states, since for $\zeta \rightarrow 0$, all three optical modes are pure Ni vibrations, while they start to mix with Ga and Mn for ζ approaching a value 0.5. Figure 7.4 shows only a part the phonon dispersion with the low-lying optical modes labeled by TO_1, TO_2 and LO. The TO_2 branch is completely decoupled from the TA_2 acoustic mode, which has the same symmetry. The TA_2 mode exhibits softening and lies extremely low in frequency so that there is no acoustic-optical coupling in this case. The other two optical modes shown in Fig. 7.4, namely TO_1 and LO, are significantly coupled to the corresponding acoustic modes. The LO mode mixes its vibrational states with the LA mode at two points, $\zeta = 0.3$ and $\zeta = 0.715$, forming two anti-crossings. Also, the TO_1 mode forms anti-crossing at $\zeta = 0.43$ with the TA_1 acoustic mode. Remarkable

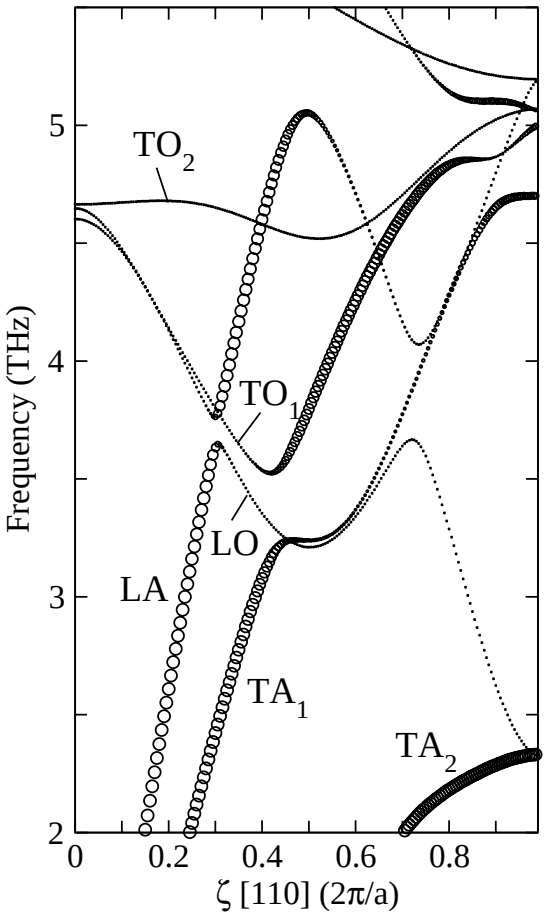

Figure 7.4: The phonon dispersion curves for the cubic $L2_1$ structure of Ni_2MnGa. This plot shows only a range of the phonon frequencies, (2.0-5.5) THz, in order to enlarge the anti-crossings between optical and acoustic branches. Also, the thickness of the lines is defined by a special filter (form factor), which shows the intensity of a particular branch, see below Eq. (7.4).

is that this interaction of the optical and acoustic vibrations decreases significantly the frequncies of the optical modes. It other words, they soften and the minimum is reached exactly at $\zeta = 0.5$. In the case of the non-coupled optical mode TO_2 the softening is hardly seen.

If the acoustic and optical modes are coupled we expect anomalies to show up in the corresponding polarization vectors. Figure 7.5 shows how this coupling affects the behaviour of the polarization vectors of the Ga acoustic modes. The Ga atom is chosen for clarity but the acoustic modes of the other atoms show similar trends. Figure 7.5 illustrates that the acoustic-optical hybridization (compare with Fig. 7.4) leads to a number of anomalies, which occur at the corresponding wave vector coordinates $\zeta = 0.3$, $\zeta = 0.43$ and $\zeta = 0.715$. These three anomalies shown in Fig. 7.5 for $\zeta = 0.3$, $\zeta = 0.43$ and $\zeta = 0.715$ can be tentatively associated with the the three different modulated structures of Ni_2MnGa: 3M, 5M and 7M, respectively. At this point this can be directly only for the 5M structure, which is characterized by the wave vector $[\zeta\zeta 0](2\pi/a)$, at $\zeta = 0.43$. But a relation between the other two modulated structures and the phonon anomalies at $\zeta = 0.3$ and $\zeta = 0.715$ can be also found.

The 7M structure shown in Fig. 7.6 was obtained by Brown *et al.* (2002) from neutron powder diffraction measurements. It is very complicated compared to the 5M structure

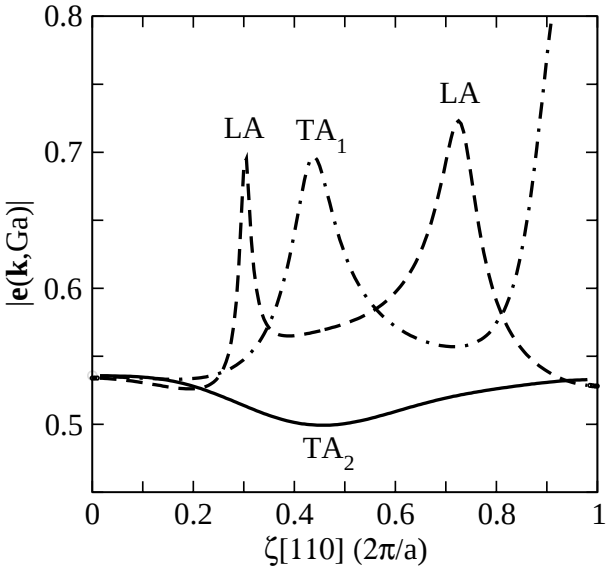

Figure 7.5: Dispersion of the polarization vectors of Ga for the $L2_1$ structure.

(see Fig. 5.2) and it is difficult to say whether it can be characterized by some specific wave vector. Tentatively, the wave vector $[\zeta\zeta 0](2\pi/a)$ with $\zeta = 0.715$ can be associated with the 7M structure. The value $\zeta = 0.715 \approx 5/7$ implies that 5 periods of mdulation must be accommodated by 7 lattice spacings. This periodical distortion is illustrated in Fig. 7.6. Five periods of this distortion are marked by hand-drawn crosses placed at the inflection points. But the 7M structure possesses also another periodicity characterized by the ratio $3/7 \approx 0.43$. Hence, the anomalies related to the 5M structure are also connected with the 7M structure.

The 3M structure can be associated with the anomaly at the wave vector $[\zeta\zeta 0](2\pi/a)$, with $\zeta = 0.3$. The calculated 3M structure is shown in Fig. 7.7. Its modulation is characterized by $\zeta = 1/3$ rather then $\zeta = 0.3$, but we have to keep in mind that the 3M structure is stable in the temperature range of $200 : \ \mathrm{K} < T < 260$ K, while the calculations are done at $T = 0$ K. It can be speculated that calculations at finite temperatures will reproduce the phonon anomaly of the 3M structure at a right position. On the other hand, the 5M structure is stable at zero temperature and the agreement of the wave vector with $\zeta = 0.43$ is excellent. The 7M structure is also stable at low temperatures with the value $\zeta = 0.715$ very close to 5/7.

7.2.2 Electron-phonon coupling

It turnes out that the position of the acoustic-optical anti-crossings in Fig. 7.4 and corresponding peaks of the polarization vectors in Fig. 7.5 can be compared with positions of anomalies found in the susceptibility, $\chi([110]q)$, calculations (Lee, Rhee and Harmon, 2002; Velikokhatnyi and Naumov, 1999). Figure 7.8 shows a plot of the susceptibility data obtained by Lee *et al.* (2002). Four peaks of the susceptibility are derived from the spin-up bands at $[\zeta\zeta 0](2\pi/a)$ for $\zeta \approx 0.4$ and $\zeta \approx 0.715$, and from the spin-down bands

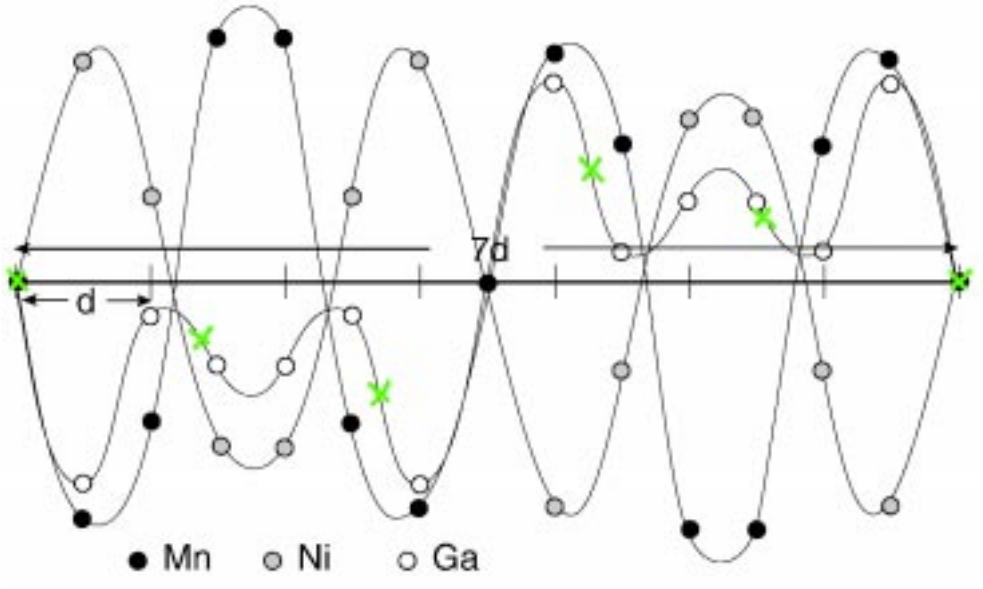

Figure 7.6: The 7M structure obtained by Brown *et al.* (2002) from a fit to the experimental data. This structure has not been obtained in the calculations so far. At the same time, the true displacement pattern of the 7M structure can be slightly different from what is shown in the Figure because the kind of fitting procedure used to obtain this structure always implies some initial guess about the structure. The hand-drawn crosses show positions of inflection points which devide the whole structure in five periods. This division is consistent with our idea that the 7M structure is characterized by the wave vector $5/7[110](2\pi/a)$. Consequently, it is related to the phonon anomaly at $\zeta = 0.715$ shown in Fig. 7.5.

at $\zeta \approx 0.425$ and $\zeta \approx 0.6$. The same peaks have been reported by Velikokhatnyi and Naumov (1999).

The idea here is to find a correspondence between the positions of the susceptibility peaks, the phonon anomalies found in the present study and the specific periods of modulation of the 3M, 5M and 7M structures shown in the Fig. 7.7, Fig. 5.2 and Fig. 7.6. The comparison shows that the susceptibility peak at $\zeta = 0.4$ (0.425) is related to the 5M structure characterized by $\zeta = 0.433$. The susceptibility peak derived from the spin-up bands at $\zeta = 0.715$ is very probably related to the phonon anomaly found for the same wave vector, which can be associated with the 7M structure. However, the 7M structure (see Fig. 7.6) can also be characterized by a modulation corresponding to the ratio 3/7, i.e., three full periods within seven lattice spacings. This shows that the anomalies found at $\zeta \approx 0.433$ are also related to the 7M structure.

The problem now is how to associate the susceptibility peak at $\zeta = 0.6$ with the phonon anomaly found at $\zeta = 0.3$. Here we have to look for the difference of the 3M structure compared to the 5M and 7M structures, the latter two being the low-temperature martensites. The 3M structure (see Fig. 7.7) has a modulation with a half-period consisting of an integer number of atomic planes. This means that the atoms at the half-period are in their non-modulated rest positions. Hence, every third (110) atomic plane is not disturbed by the 3M modulation (in contrast to the full period which would imply that

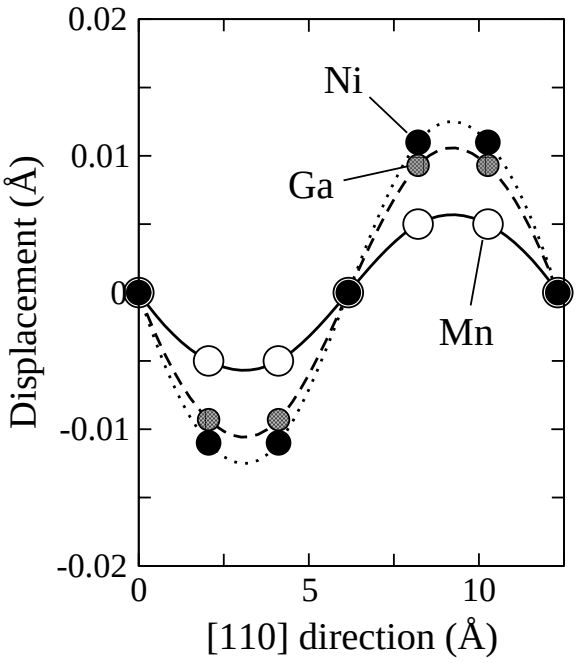

Figure 7.7: The 3M structure calculated by A. Ayuela *et al* (Zayak, Entel, Enkovaara, Ayuela *et al.*, 2003b). The static wave-like distortion is consistent with the pattern predicted by the soft [110]-TA_2 mode. The wavevector corresponding to this distortion coincides with the phonon anomaly at $\zeta = 0.3$ in Fig. 7.5.

only every sixth (110) plane is in its rest position). One can imagine that this gives rise to a factor of 2 for the wave vector of the susceptibility peak position. Hence, both $\zeta = 0.3$ and $\zeta = 0.6$ wave vectors are characteristic for the 3M structure.

It was shown by Lee *et al.* (2002) that the susceptibility peaks vary with depending the magnetization. Namely, the peak of the susceptibility moves from $\zeta = 0.3$ to $\zeta = 0.4$ when the magnetization increases (upon cooling) from 60% to 80% of its saturation value. This is a beautiful idea which allows to explain the fact that the premartensitic transition appears at higher temperatures (when magnetization is smaller), while the 5M structure will replace the 3M structure upon cooling due to increase of the magnetization. However, there are still discussions about this issue. It is not yet clear whether the magnetization really plays such an important role here. Therefore it makes sense to calculate phonon dispersion for the cubic phase of Ni_2MnGa with lower magnetization value (60%) as sugested by Ayuela and Enkovaara (2003), the result of which will show in how far the idea of Lee *et al.* (2002) can be applied to Ni_2MnGa.

However, there are several points not being discussed by Lee *et al.* (2002). The first one concerns the peaks at $\zeta = 0.6$ and $\zeta = 0.715$. The interpretation given above can hopefully cover this matter. Another point is the smooth change of the wave vector for the modulation which arises from the findings of Lee *et al.* (2002). This would mean that the 3M structure gradualy changes its modulation wave vector towards the 5M. However, this is not the case in experiment. The phase transformation from 3M to 5M happens upruptly, being actually the first order. Also, it is not clear how the susceptibility peaks are related to the acoustic-optical phonon anomalies. And last, what is the criterion which defines the particular modulation to appear under certain conditions, remembering the fact that the 3M modulation appears at higher temperatures. Upon cooling 3M is replaced

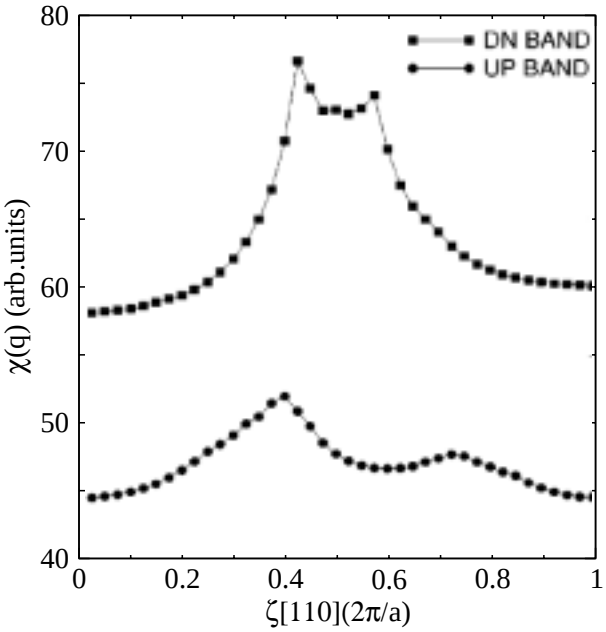

Figure 7.8: Generalized susceptibility of the spin-up and spin-down bands which cross the Fermi level as calculated by Lee *et al.* (2002).

by the 5M or 7M (we do not consider the non modulated T structure at this point). The 5M structure can be suppressed in favour of the 7M structure by an external uniaxial pressure applied to the sample.

Since the susceptibility (Fig. 7.8) was calculated at zero temperature, the corresponding ground state might be the 5M structure. At the same time, both spin-up and spin-down electron bands give rise to the susceptibility anomalies at the wave vector characterizing the 5M structure. This implies that carriers with both spin orientations are involved simultatiously. One may speculate that the reason for this may be connected with the electron-phonon coupling, which does not distinguish charges with different spins. The argumentation is then as follows. At some finite temperature, 260 K, for instance, the total magnetization is about 60% of its low-temperature saturation value. According to Lee *et al.* (2002) the spin-up bands will give rise to a peak in the susceptibility at $\zeta = 0.3$, while the spin-down electrons produce a peak at $\zeta = 0.6$, and both peaks can be related to the 3M structure. Similar discussion can be used to explain the 7M structure. Forexample, applied pressure will move one of the susceptibility peaks, say the one at $\zeta = 0.6$, towards $\zeta = 0.715$, which will stabilize the 7M structure and suppress the 5M structure. Besides the electron-phonon coupling also electro-electron interaction is important for the stability matter. In particular for martensites involving transition metals like Ni, Co or Fe the electron-electron scattering is more important than for other systems (Singleton, 2001).

7.2.3 Vibrational density of states

We now discuss the individual contributions of the atoms to the phonon modes. It was shown that the TA_2 phonon mode is extremely low and even imaginary, thereby being

uncoupled from the corresponding optical modes, in particular the TO_2 mode. Whereas, the other two acoustic modes, LA and TA_1 are significantly coupled to the optical phonons of the LO and TO_1 branches, respectively. There is also a group of optical modes which have frequencies above 5 THz which are not coupled to the acoustic modes. Also the optical modes with the higher frequencies have only a weak wavevector dependence, while the low-lying optical modes show strong dispersion. Similar to lattice dynamics of molecular crystals, one can consider the low-frequency optical vibrations as *external modes* and the high-frequency modes as *internal modes* (Dove, 1993). The difference is that the latter involve distortions of the nearest neighbour bonding distances. The external modes, in turn, involve more complicated behaviour, where several atoms move as rigid units with frequencies being typically below 3-4 THz.

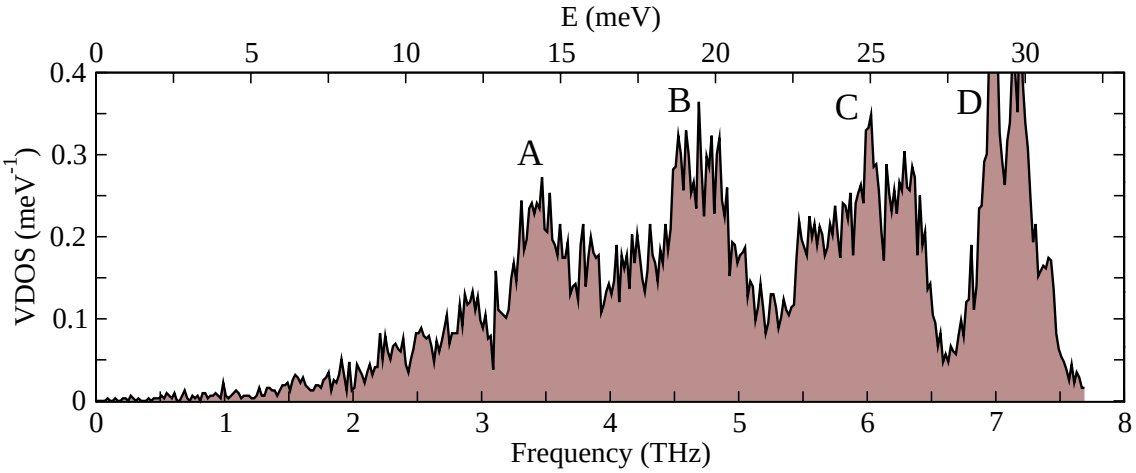

Figure 7.9: Distribution of the total vibrational density of states of Ni_2MnGa, which has been calculated from the phonon dispersion curves by using Eq. (7.3).

One can learn more about significan coupling of atoms from the distribution of the vibrational density of states (VDOS). The total VDOS calculated from the phonon dispersion for the $L2_1$ structure is shown in Fig. 7.9. We note that these phonon DOS is not complete since the summation is not done over the whole BZ, but only over the [110] direction. The distribution of the partial phonon density of states is given by

$$g_{\alpha,k}(\omega) = \frac{1}{nd\Delta\omega} \sum_{\mathbf{k},j} |e_\alpha(k;\mathbf{k},j)|^2 \, \delta_{\Delta\omega}(\omega - \omega(\mathbf{k},j)), \tag{7.3}$$

where $e_\alpha(k;\mathbf{k},j)$ is the α-th Cartesian component of the polarization vector for the k-th atom; n is the number of sampling k points and d is the dimension of the dynamical matrix (Parlinski, 2002). The total VDOS is calculated by sum of all partial contributions.

Figure 7.9 shows the presence of four maxima separated in frequency, which are labeled by A, B, C and D. The latter two peaks (C and D) are formed by the optical branches which were assigned already as internal modes. The peaks are sharp because of the flat character of these modes, i.e., their weak dependence on $\mathbf{k}$.

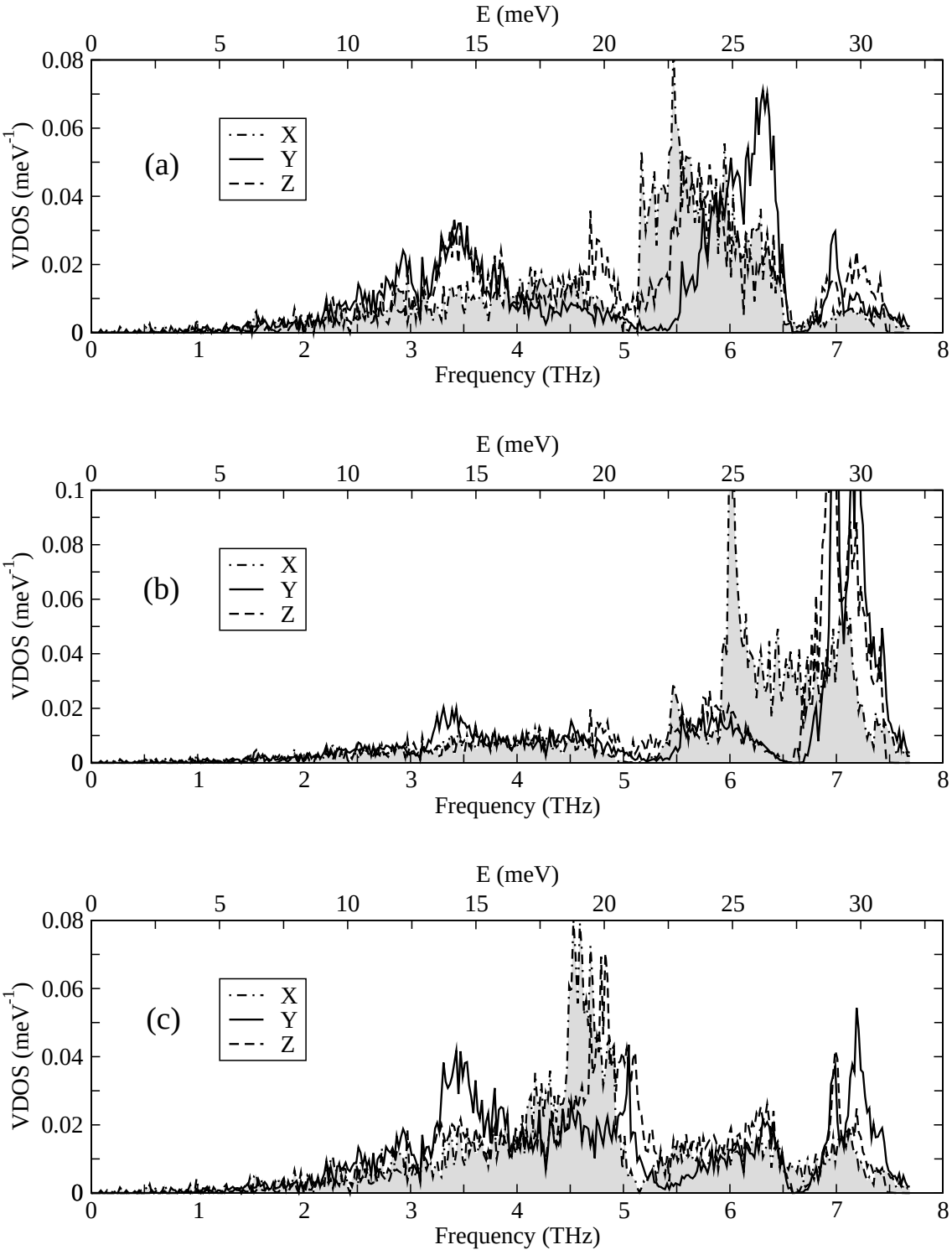

Figure 7.10: Partial phonon density of states of Ni_2MnGa calculated from the phonon dispersion curves via Eq. (7.3): (a) Ga, (b) Mn and (c) Ni.

The partial phonon DOS presented in Fig. 7.10 shows that the peak D is formed mainly by the vibrations of Mn. The fact that the Mn atoms vibrate with the highest frequencies is undestandable, because Mn is the lightest atom in Ni_2MnGa. The broad wide peak C at 6 THz is mainly connected with the vibrations of Ga and with small a contribution from Mn. The optical modes of Ni have the lowest frequencies. The peak B in Fig. 7.9 is related to Ni and corresponds to the TO_2 mode. This mode does not couple to the acoustic vibrations and therefore more localized in energy.

The most interesting peak of the VDOS is labeled by A. It is connected with the two modes of Ni which mix with corresponding acoustic modes. Only the y and z vibrational components contribute to this peak, corresponding to the longitudinal mode and the z-polarized transverse mode, whereby the longitudinal contribution is considerably stronger. Figure 7.10 shows that in this case Ni and Ga appear to be coupled through the longitudinal vibrations. The related peaks in Fig. 7.10(a) and Fig. 7.10(c) are at the same position and of the same size (shape). Also, longitudinal-phonon optical modes can be associated with charge density waves being related to the sharp peaks in the magnetic susceptibility $\chi(q)$ (Lee, Rhee and Harmon, 2002; Velikokhatnyi and Naumov, 1999). Such charge density waves can be responsible for structural instabilities in crystals.

7.2.4 Form factors

In addition to the phonon dispersion curves shown in Fig. 7.2, one can use specific filters which allow to extract additional information. The same phonon dispersion curves can be plotted by taking into account information about atomic displacements which shows how atomic displacements are related to specific phonon branches. This is presented in Fig. 7.11 in form of so called *form factors* (Parlinski, 2002). The thickness of the lines is proportional to the values of the form factors. Figure 7.11(a) shows the resulting relative intensities of the phonon modes with respect to the atomic displacements (Parlinski, 2002), whereby the following expression for the form factor has been used,

$$F^{(S)}(\mathbf{k}, j) = \left| \sum_{\mu} \frac{\mathbf{e}(\mathbf{k}, j; \mu)}{\sqrt{M_\mu}} \right|^2 . \tag{7.4}$$

A second form factor can be introduced which is called *projected* form factor, It plays a similar role as the dynamical structure factor and is connected with the intensity of one-phonon coherent neutron scattering (Parlinski, 2002):

$$F^{(P)}(\mathbf{k}, j) = \frac{1}{\mathbf{k}^2} \left| \sum_{\mu} \frac{\mathbf{k}\mathbf{e}(\mathbf{k}, j; \mu)}{\sqrt{M_\mu}} \right|^2 . \tag{7.5}$$

The form factor presentation of the phonon modes allows to show nore clearly the points where hybridizations of the phonons take place and which modes are involved. In Fig. 7.2, at wave vector $[0.3, 0.3, 0](2\pi/a)$, the dispersion curves only cross each other with no sign of hybridization (anti-crossing), whereas Fig. 7.11 shows clearly the hybridization of the LA phonon mode with the corresponding optical mode.

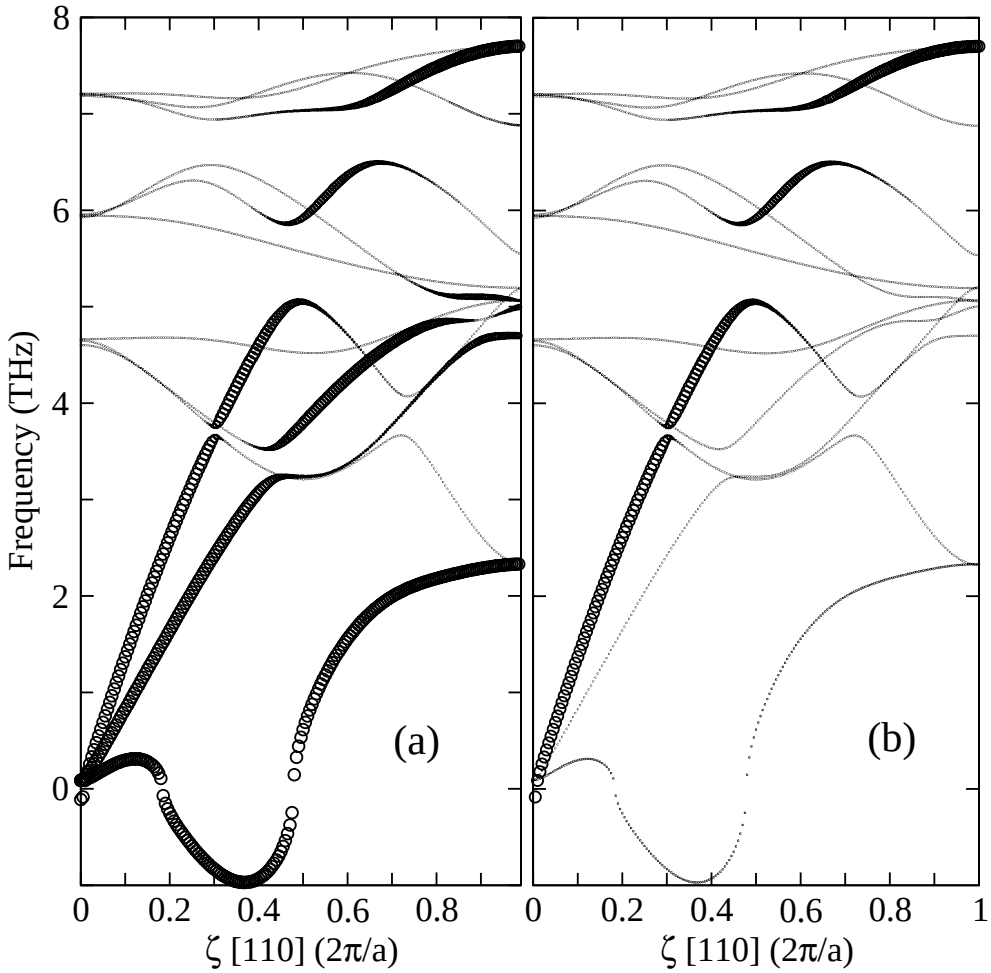

Figure 7.11: Phonon form factors of Ni_2MnGa calculated from the phonon dispersion curves.

From the discussion so far we can draw the following statements. The softening of the TA_2 mode is responsible for the instability of the cubic $L2_1$ structure with respect to the corresponding distortion. The cubic structure transforms first to the premartensitic 3M structure (which has been recently calculated by A. Ayuela (Zayak, Entel, Enkovaara, Ayuela *et al.*, 2003c)) and at lower temperatures to the 5M (or 7M) martensitic structure.

In addition, we have found that the low-lying optical modes couple to the acoustic modes. This acoustic-optical interaction is responsible for the fine modulation of the 5M structure shown in Fig. 5.3. The main factor which causes this effect is the coupling of Ni and Ga atoms leading to a drastical lowering of the corresponding optical modes and to the formation of charge-density waves. The latter can be related to the magnetic susceptibility anomalies (Lee, Rhee and Harmon, 2002; Velikokhatnyi and Naumov, 1999) which shows pronounced peaks at $\mathbf{q} = [\zeta, \zeta, 0](2\pi/a)$ for $\zeta = 0.43$, $\zeta = 0.6$ and $\zeta = 0.715$. This relates the phonon anomalies with the anomalies of the susceptibility and explains the formation of the specific modulated structures. For a more detailed discussion we would have to evaluate the impact of the electron-electron and electron-phonon interactions on

the spin-resolved charge density. This is beyond the scope of present work.

Some further aspects have not been considered so far, like the influence of the elastic entropy which is believed to be also involved in the sequence of phase transitions in Ni_2MnGa (Ayuela and Enkovaara, 2003; Enkovaara, Ayuela, Nordström and Nieminen, 2002b). Of further interest might be influence of the magnetic noncollinearity, although it was shown that spin spirals do not show anomalies which could be connected with the shuffling of the $L2_1$ structure (Enkovaara, Ayuela, Jalkanen, Nordström *et al.*, 2003a).

In view of the present results, the intermediate and the martensitic transitions seem to be really independent of each other. This is an intriguing hypothesis which could be confirmed by investigations of other Heusler alloys which also show martensitic transfrmations and magnetic shape memory.

7.3 Phonons and related properties of the bct (I4/mmm) structure

The discussions above showed that the $L2_1$ structure has a strong tendency to undergo a phase transformation with specific shufflings of atoms, giving rise to the 3M, 5M or 7M structures. In addition, Ni_2MnGa may also be stable at low temperature without any modulation as the calculation of the T structure shows (see Table 2.1 and Fig. 4.2). Experimentally this structure can be stabilized under applied uniaxial pressure (Martynov and Kokorin, 1992) or for certain Ni-Mn-Ga compositions (Ayuela and Enkovaara, 2003).

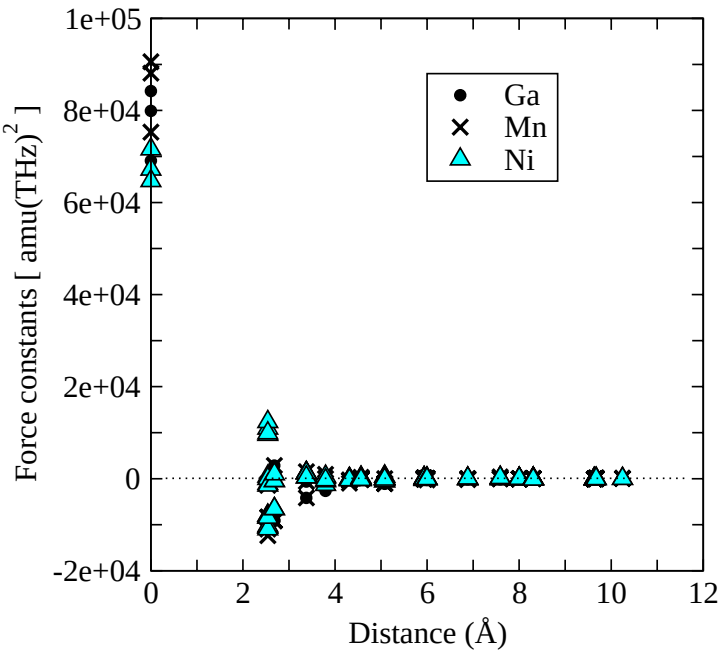

Figure 7.12: Dependence of the interatomic forces for the T structure of Ni_2MnGa on the distance in [110] direction. Vanishing forces is the criteria to be met in order to obtain correct phonons using the direct method. This plot shows that the interatomic forces in Ni_2MnGa converge to zero within ~ 6 Å. The length of the supercell is ~ 18 Å, which means that the calculated phonons are very accurate.

The long $1 \times 5 \times 1$ supercell of 40 atoms used above in the phonon calculation of the cubic $L2_1$ structure, can be easily modified for the case of the T structure. For this, corresponding lattice parameters have to be scaled according to the ratio $c/a = 1.25$,

Table 7.6: List of phonon frequencies at the Γ point with irreducible representations of the vibrations. For the acoustic modes the nonzero values are corrected by the values in brackets; they arise from certain limitations in the numerical algorithm in case of $k \to 0, \omega \to 0$.

Multi.	Omega	Irreducible Representations
1	-0.199 (0.0)	B_{3u}(I)
1	-0.118 (0.0)	B_{1u}(I)
1	0.132 (0.0)	B_{2u}(I)
1	5.082	A_g(R)
1	5.246	B_{1u}(I)
2	5.938	B_{2u}(I) + B_{3u}(I)
1	6.233	B_{2g}(R)
1	6.283	B_{3g}(R)
1	7.247	B_{2u}(I)
1	7.261	B_{3u}(I)
1	7.518	B_{1u}(I)

whereby the volume is kept constant. The new supercell parameters are $a_{\text{orth}} = 3.793$ Å, $b_{\text{orth}} = (5/\sqrt{2})a_{\text{cubic}}$ Å and $c_{\text{orth}} = 6.754$ Å. Analysis of the supercell symmetry shows that nine independent atomic displacements are needed in order to evaluate the phonon dispersion curves for the [110] direction (the point group of the supercell is the same as in the case of the $L2_1$ structure allowing a direct comparison of results for the two structures simple).

Figure 7.13 shows the resulting phonon dispersion curves calculated for Ni_2MnGa along the [110] direction in the T structure. Similar to the previous case, the phonon energies are exact for $\zeta = 0$ (Γ), $\zeta = 1.0$ (X) and three points inbetween: $\zeta = \frac{1}{4}, \frac{1}{2}, \frac{3}{4}$. Curves between these exact points have been obtained from interpolation which gives an accurate description because of the length of the supercell and the fact the the forces converge as shown in Fig. 7.12. Although there are no experimental data available for the T structure, which is martensitic, meaning that the structural domains make specific orientation of the sample meaningless, the calculated dispersions are particularly interesting.

We find that the [110]-TA_2 phonon mode is not soft for the T structure in contrast to $L2_1$. It also does not show any tendency to undergo a modulated superstructural change like the 5M structure inspite of the fact that the only difference between $L2_1$ and T lies in the c/a ratio.

Of further interest is that we also observe for the T structure a coupling between acoustic and low-lying optical modes. Symmetry allows the longitudinal and transverse acoustic and optical modes to form unti-crossings at $\zeta \approx 0.3$, $\zeta \approx 0.43$, respectively. Similar phonon anomalies were observed in case of the cubic structure (see Fig. 7.2). However, here, there is no phonon anomaly at $\zeta = 0.715$. In view of the previous discussions about the role of the acoustic-optical coupling, it is surprising to find these anomalies for the structure for which no kind of modulation is expected. In the previous case we have taken

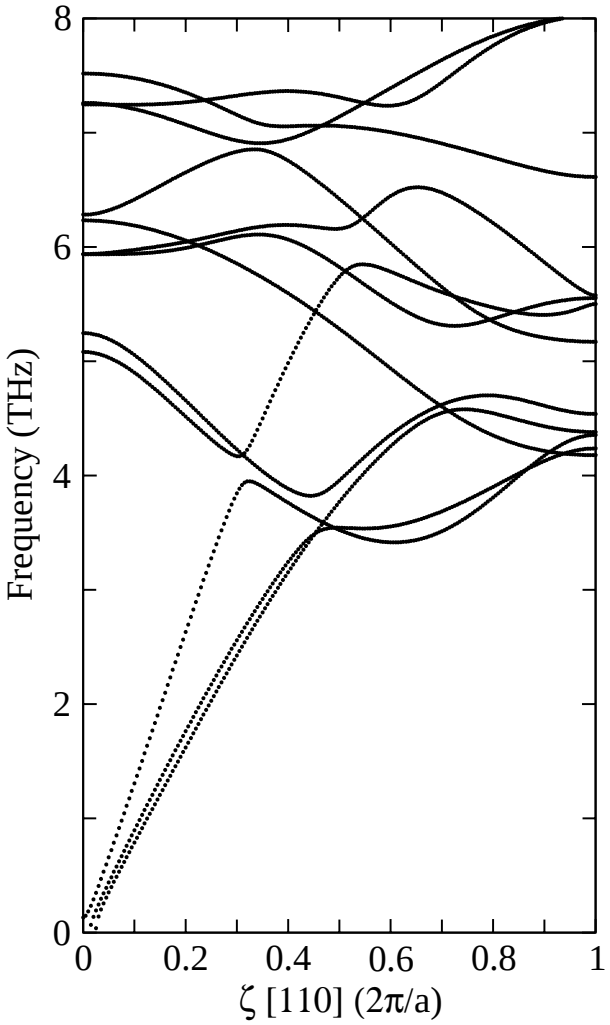

Figure 7.13: Calculated phonon dispersion curves of the tetragonal (I4/mmm) structure of Ni_2MnGa. The reduced wavevector coordinate ζ spans the fcc BZ from Γ to X. The symmetry of each phonon mode at the Γ point is given in Table 7.6.

the anomalies shown in Fig. 7.5 as a hint for strong electron-phonon coupling, which, together with the susceptibility peaks, was suggested to be responsible for the sequence of phase transformations in Ni_2MnGa. We could also relate the transformations to the fine delails of the modulated structure (see Fig. 5.3). Therefore, the question is now how the acoustic-optical coupling affects the T structure and is there any long-range interactions?

Inspite of the fact that we have not yet done supercell calculations for all possible modulation patterns, for the T structure we do not expect that also the T structure could lower its energy for apropriate shuffles of atoms (which are present in practically all martensites).

The phonon dispersion curves allow to obtain the ultrasound velocities propagating along [110] in Ni_2MnGa. The initial slopes of the acoustic branches LA, TA_1 and TA_2 give corresponding values for v_{L}, v_{TA_1} and v_{TA_2}, which are listed in Table 7.7 together with the experimental data measured by Vasil'ev *et al.* (1994) for the whole temperature range from 4 to 360 K. The masurements show anomalies at $T_{\mathrm{P}} = 260$ K, $T_{\mathrm{M}} = 200$ and also allow to obtain the sound velocities in the limit $T \to 0$ K. Since the T structure for

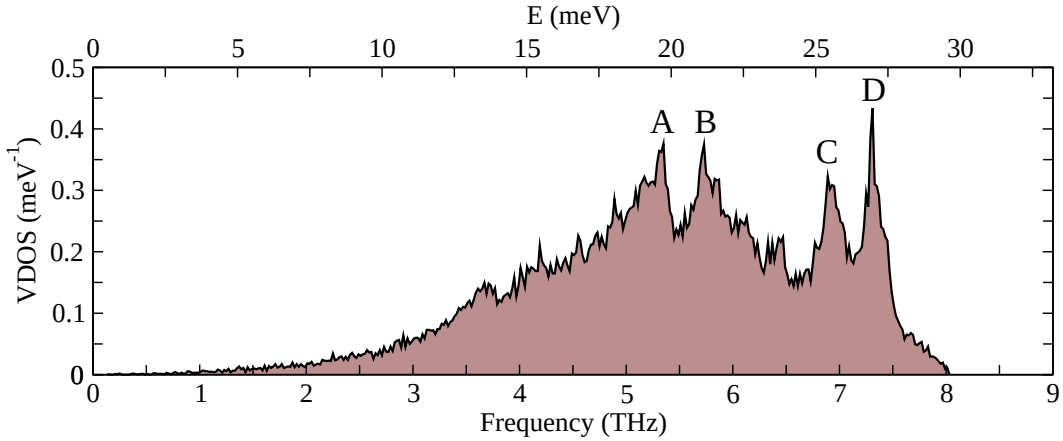

Figure 7.14: Total vibrational density of states calculated for the [110] direction of the tetragonal Ni_2MnGa structure with $c/a = 1.25$.

which the phonons have been calculated here exists at low temperatures, the calculated values can be compared with the experimental ones (see Table 7.7). We observe that the calculated values are smaller than the experimental ones, but still can be considered to be in a reasonable agreement. One should also remember that the measured sound velocities might correspond rather to the 5M than to the T structure.

Table 7.7: Experimental and theoretical values of the ultrasound (propagating in [110] direction) velocities of Ni_2MnGa. The experimental values were measured by means of the electromagnetic-acoustic transformation (EMAT) and echo-pulse techniques by Vasil'ev *et al.* (1994). The theoretical values have been obtained from the initial slopes of the acoustic phonon branches for $\zeta \to 0$.

$\times 10^5$ m/s	Experiment[a]	Theory
v_{L}	5.7	4.88
v_{TA_1}	4.2	3.52
v_{TA_2}	3.4	3.26

[a](Vasil'ev, Keiper, Kokorin, Chernenko *et al.*, 1994)

Figure 7.14 shows the distribution of the vibrational DOS corresponding to the phonon dispersion curves presented in Fig. 7.13. It is obvious that, in contrast to the $L2_1$ structure, there is much less structure in the VDOS distribution. The peaks labeled by A, B, C and D are not so distinct as for the cubic case before. The reason for this mixture is that the optical modes in the case of the T structure are not degenerate any more at the Γ point. For the cubic structure the optical modes formed three groups of curves which are degenerate at the Brillouin zone center. Now, tetragonal symmetry has removed the degeneracy of the optical branches leading to a diferent sequence of the phonon modes (compare Fig. 7.2, Fig. 7.13 and Table 7.4 and 7.6).

More details can be discussed by studing the partial VDOS shown in Fig. 7.15. Again, similar to the case of the $L2_1$ structure, the Mn atoms have the highest frequencies. Well

recognizable is the coupling of Ga and Ni atoms. This effect gives rise to the A and B peaks of the total VDOS in Fig. 7.14. The two peaks lie between 5 and 6 THz, having very similar sizes and shapes as can be recognized from Fig. 7.15(a,c). Remarkable is that these peaks are formed by x vibrational components alone. Vibrations along the Z and Y directions do not show any significant coupling effects of different kind of atoms. There is a very low peak of the VDOS around 3.6 THz arising from Ga and particularly by its z-vibrational component, see Fig. 7.15(a). However, Ga is not significantly coupled to the vibrations of the other atoms.

Similar to the case of the cubic structure, we can present the phonon dispersion curves for the T structure using the form factors given by formulas (7.4) and (7.5), see Fig. 7.16. In the case of Fig. 7.16(a) those modes which have the highest intensity. The second plot in Fig. 7.16(b) shows those modes which vibrate strongly along the direction of the wavevector. Both form factors are important in neutron scattering experiments.

7.4 Conclusions for the phonon calculations

We have calculated phonon dispersion curves of two non-modulated structures of Ni_2MnGa, namely, of the cubic high-temperature $L2_1$ structure and of the low-temperature tetragonal T structure (see Table 2.1). The cubic structure has been found to be unstable due to the soft acoustic phonon [110]-TA_2 mode. The soft mode anomaly appears at the wave vector q=1/3[110], which is consistent with the experimental data and results in modulated shuffles of atoms in the 3M, 5M and 7M structures. It has been shown that the subtle competition of low-lying optical modes of Ni and acoustic modes accounts for the experimentally observed wave vectors, for which anomalies have been observed. The results of the phonon calculations are consistent with the susceptibility calculations by Lee *et al.* (2002), which allow to discuss the conditions to be met in order to obtain modulated phases. Phonon calculations along with an analysis of the 5M structure showed that the modulation has additional details which can be related to the acoustic-optical coupling of phonons. The tetragonal structure was found to be stable, which agrees also with experiment. In both cases the dispersions allowed to estimate the elastic parameters, which turned out to be in very good agreement with experimental data.

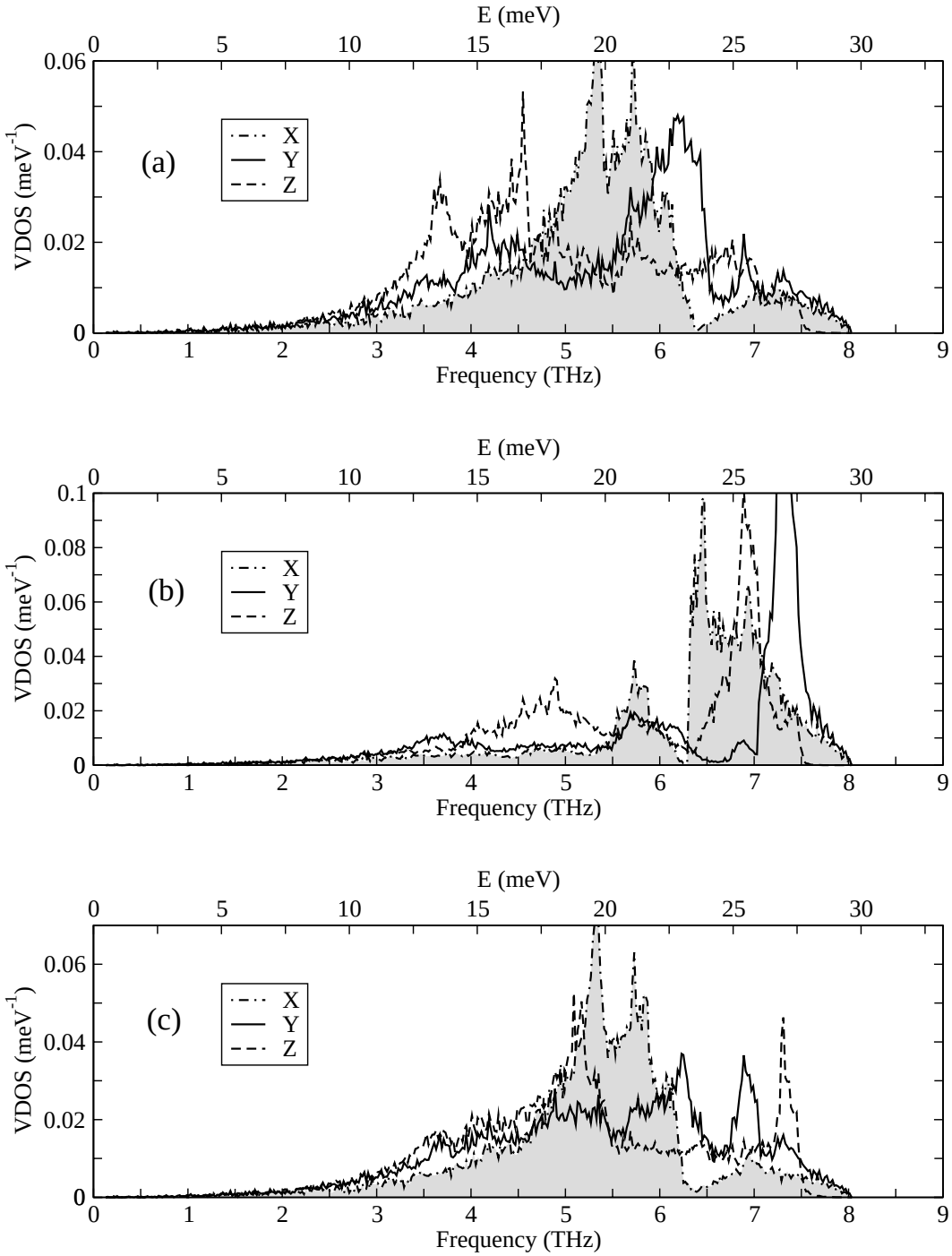

Figure 7.15: Partial vibrational density of states calculated for the [110] direction of the bct Ni_2MnGa (T) structure.

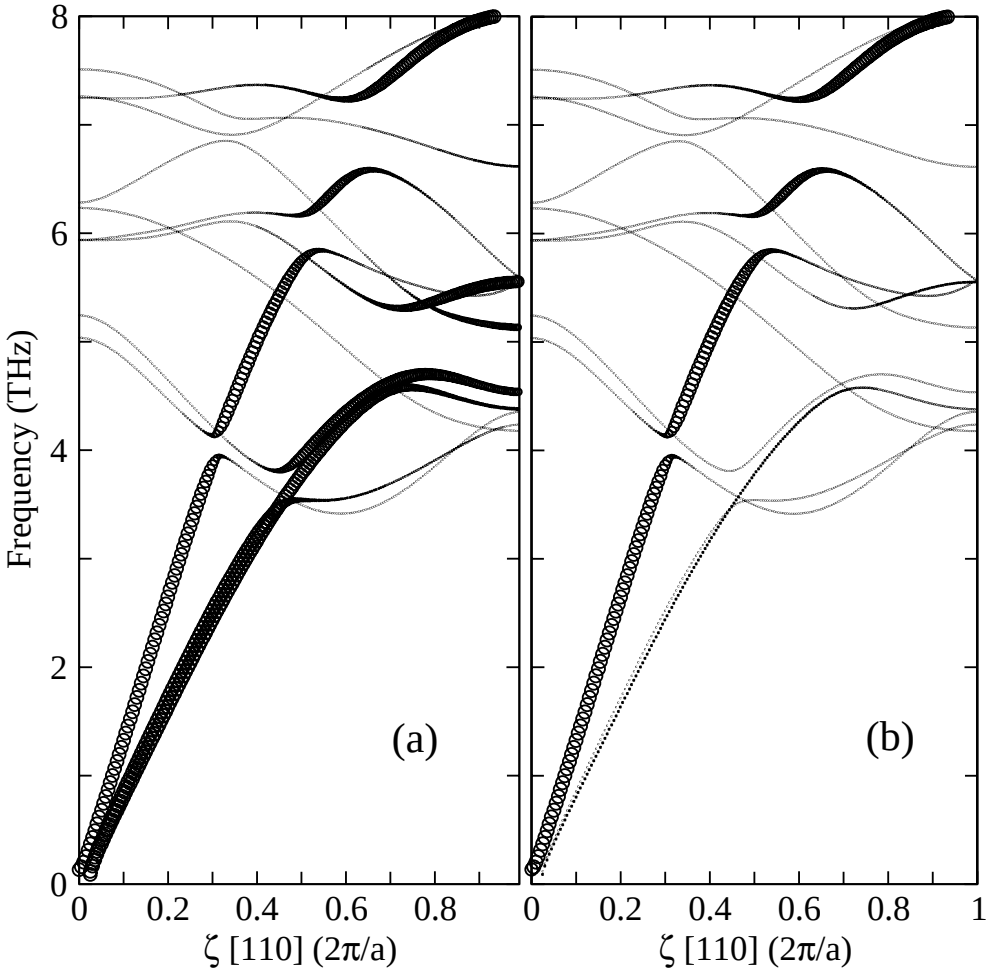

Figure 7.16: Phonon form factors for the bct structure of Ni_2MnGa calculated from the phonon dispersion curves.

8 Study of non-stoichiometric systems

Most experimental studies concentrate on off-stoichiometric compositions of Ni-Mn-Ga (as shown in the ternary compositional diagram in Fig. 2.7) while theoretical studies are mostly done for the stoichiometric structure of Ni_2MnGa. Hence, theoretical investigations for the off-stoichiometric compositions are urgently needed. The results obtained so far allow to discuss the importance of the Ni-Ga interaction in Ni-Mn-Ga showing that stability of the modulated shuffles benefits from this coupling (and the locally broken symmetry). The modulation facilitates the formation of hybrid Ga-p states with other atoms, which is less favourable in a perfectly symmetric environment, where Ga "cannot choose" neighbours to couple (the shuffles of atoms remove this degeneracy allowing for a lower energy of the system).

The question now is whether the modulated shuffles are the only way to remove the perfect order. This could also be done by doping the structure by local defects which would reflect much better experimental situation, where the order rate is usually not more then 98% (Webster, Ziebeck, Town and Peak, 1984). In order to check this we have simulated off-stoichiometric $Ni_{2+x}Mn_{1-x}Ga$ structures for compositions which have been already studied experimentally by Vasil'ev *et al.* (1999a). In particular, we expect from these calculations further information about the phase transitions shown in Fig. 2.8.

In the off-stoichiometric simulations a simple cubic supercell of 16 atoms is used which allows to describe the composition $Ni_{8+1}Mn_{4-1}Ga_4$ shown in Fig. 8.1 with corresponding parameter $x = 0.25$ in $Ni_{2+x}Mn_{1-x}Ga$ (see Fig. 2.8). An extra atom of Ni is placed onto one of the Mn positions (here at the central site of Fig. 8.1). This supercell has first been optimized with respect to atomic positions and volume for $c/a = 1$. After relaxation the optimal volume was smaller by about 1.6% (192.51 Å^3) compared to the stoichiometric structure (195.79 Å^3) yielding a small change of the atomic positions of Ni while Mn and Ga positions as well as the extra Ni position remained unchanged. Figure 8.1 shows that the extra Ni atom has eight nearest Ni neighbours which relaxed towards this extra Ni atom. Figure 8.2 shows a projection of two atomic (001)-planes on top of each other with one plane containing the extra Ni as well as the Mn and Ga atoms, and with the other plane just above the extra-Ni containing only Ni atoms. One can see in Fig. 8.2

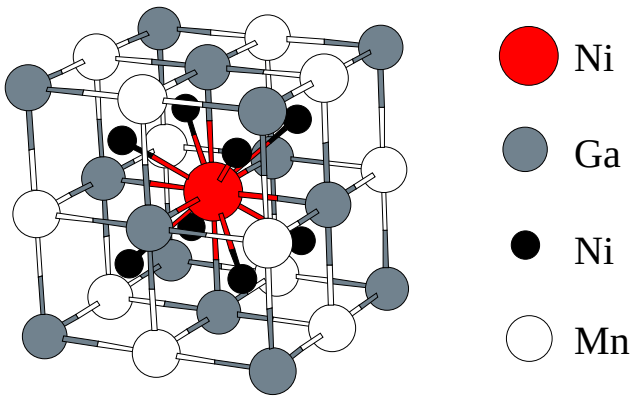

Figure 8.1: An off-stoichiometric supercell for $Ni_{2+x}Mn_{1-x}Ga$ with $x = 0.25$ obtained by replacing Mn atom by a Ni atom in one of the 16 position of the $L2_1$ cell.

how the structure re-arranges itself due to the replacement of Mn by Ni. A more realistic situation of stronger intermixing in a larger supercell would be required which has not been considered so far.

The relaxation did not change ferromagnetically aligned moments apart from the extra Ni which has got a smaller magnetic moment (0.24 μ_B) compared to the regular Ni atoms ($\approx 0.35\ \mu_B$). Keeping the experimentally observed magnetic order is important here because of a tendency to form an antiferromagnetic alignment of the magnetic moments in Ni-Mn-Ga. It was shown by Enkovaara *et al.* (2003b) that indeed Mn-doped (an extra Mn atom replaces Ga) Ni-Mn-Ga is antiferromagnetic in agreement with experimental data. In turn, the present results agree with experimental studies for the Ni-doped alloys (Vasil'ev, Bozhko, Khovailo, Dikshtein *et al.*, 1999a).

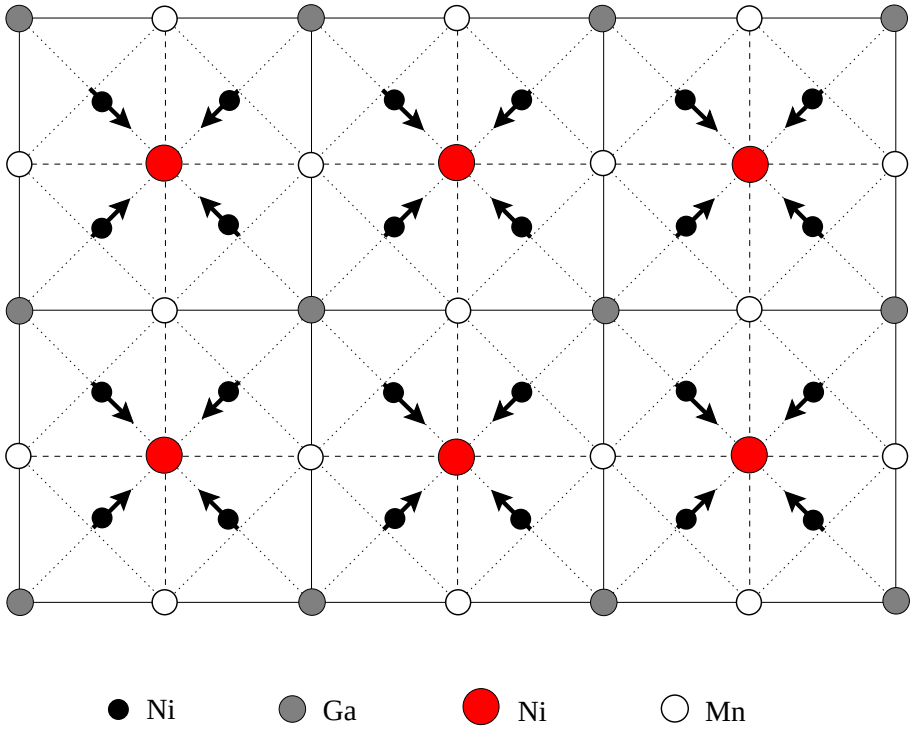

Figure 8.2: Projection of two atomic (001)-planes of the $Ni_{8+1}Mn_{4-1}Ga_4$ structure in its equilibrium state obtained after structural relaxation.

This relaxed cubic structure is now used to study the impact of a tetragonal deformation. Figure 8.3 shows the dependence of the total energy on the c/a ratio for the three cases: perfect stoichiometric Ni_2MnGa structure, the 5M structure, and off-stoichiometric structure defined by $Ni_{8+1}Mn_{4-1}Ga_4$. It turns out that the total energy curve for the case of the off-stoichiometry has a minimum at $c/a = 0.94$, exactly the value for which also the 5M structure has minimal energy coinciding with the experimental data for c/a ratio. This shows that both modulation and disorder are responsible for the stable tetragonal structure with $c/a = 0.94$.

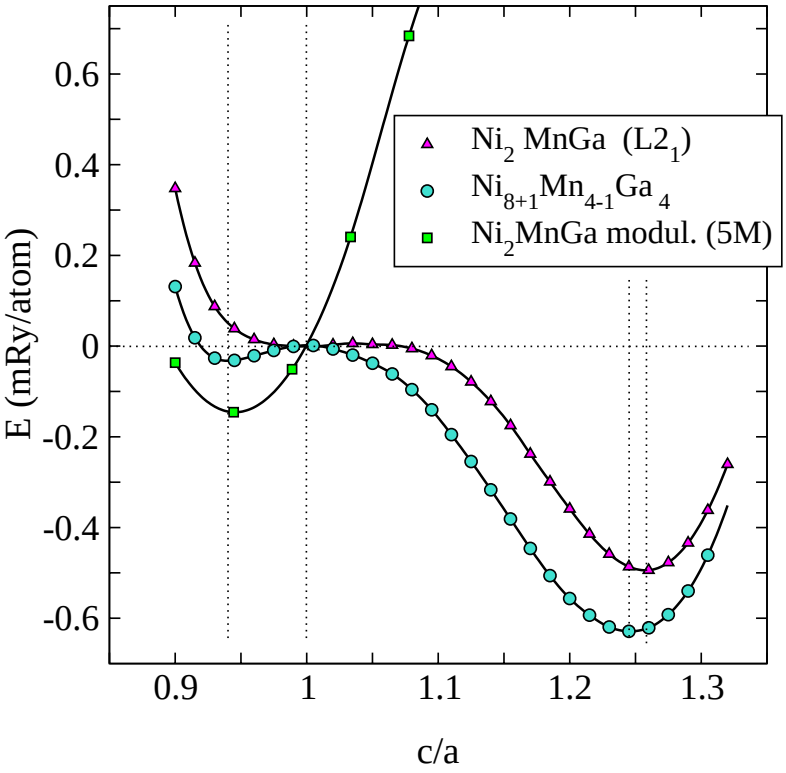

Figure 8.3: The relative change of the total energy of Ni_2MnGa as a function of the c/a ratio for the three different cases: Ordinary $L2_1$ structure, modulated 5M structure and off-stoichiometric superstructure with formula $Ni_{8+1}Mn_{4-1}Ga_4$.

Figure 8.4 presents the total electronic DOS for the off-stoichiometric case (structure shown in Fig. 8.1). The DOS is shown for the cubic structure with $c/a = 1$ and the tetragonal structure with $c/a = 0.94$. Important is here the dip in the minority-spin DOS right at the Fermi level. The dip is present for both cases, but develops stronger for the more stable tetragonal structure. The analysis of the partial DOS shows again that the two peaks responsible for the dip originate from the Ni-d and Ga-p orbitals (the effect is similar to the results obtained for the 5M structure in Zayak *et al.* (2003c)).

In summary, the off-stoichiometric calculations for the $Ni_{8+1}Mn_{4-1}Ga_4$ supercell yield a local minimum in the total energy curve at $c/a = 0.94$, which is the "natural" tetragonality ratio for Ni-Mn-Ga at low temperatures. The same tetragonality ratio can be obtained in the calculations when taking into account modulation (5M structure). Similar to the case of the 5M structure stability of the $c/a = 0.94$ ratio is related to a dip in the minority-spin DOS which develops from hybridizing Ni-d and Ga-p states right at E_F stabilizing the tetragonal variant with $c/a = 0.94$. In future work, it is necessary to perform calculations using the GGA+U method. This will split further apart the bonding and anti-bonding states around E_F thereby deepening the dip. We expect from these calculations the 5M structure to have lowest energy and the T structure to be metastable.

It is also necessary to perform further off-stoichiometric calculations. Theoretical studies must consider a range of $0 < x < 0.25$ and must move gradually from smaller to larger x values as it was done in experimental studies (Bozhko, Vasil'ev, Khovailo, Dikshtein *et al.*, 1999; Khovailo, Takagi, Bozhko, Matsumoto *et al.*, 2001; Vasil'ev, Bozhko, Khovailo, Dikshtein *et al.*, 1999a). But, this is computationally extremely demanding

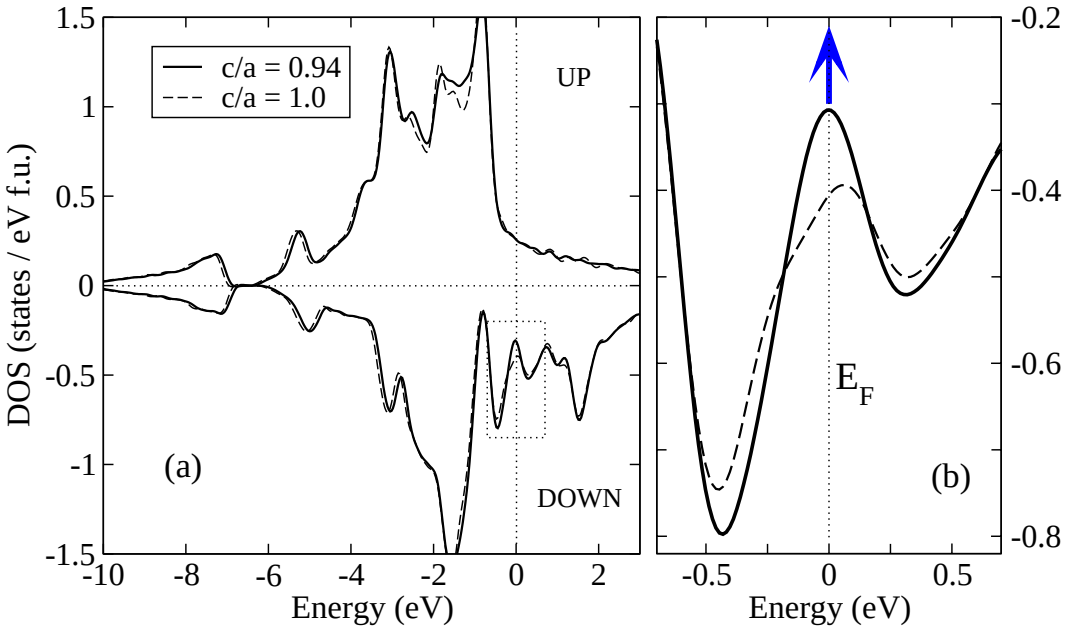

Figure 8.4: Electronic density of states of the off-stoichiometric alloy $Ni_{2+x}Mn_{1-x}Ga$ with $x = 0.25$ for the two cases: Unstable $c/a = 1$ and metastable $c/a = 0.94$. (a) Total DOS for the cell with 16 atoms. (b) Enlargement of the total DOS which shows better the dip in the minority spin density of states. Analysis of the partial density of states shows that the states which form the dip are derived from the Ni-d and Ga-p orbitals.

and beyond the scope of the present work. Another approach is to use different *ab-initio* methods, like those which are based on the concept of a pseudo-atom (KKR-CPA). The KKR-CPA approach is very well suited for non-stoichiometric calculations. We found that the KKR-CPA method can reproduce fairly well lattice constant of the cubic structure and magnetic moments of the atoms in $Ni_{2+x}Mn_{1-x}Ga$. However, the elastic properties cannot be reproduced correctly. That is why the supercell approach is the only possible way for realistic non-stoichiometric calculations.

Summary

This work presents an atomistic theoretical study of the ferromagnetic Heusler compound Ni_2MnGa with respect to its magnetic, structural and dynamical properties. The entire variety of the properties is discussed in terms of total energy electronic structure calculations. The thesis consists of eighth chapters, a summary, an appendix and a list of references. Here is a brief summary of the eight chapters.

Chapter 1 gives a short general introduction to Heusler alloys and their physical properties. In Chapter 2 we present an overview of the experimental background and and previous theoretical investigations of Ni_2MnGa. In Chapter 3 a short introduction to the density functional theory is given, which is the basis for all methods used in this work. In Chapter 4 we presents the results of total energy calculations for Ni_2MnGa. The main attention is paid to the basic properties of the parent high-temperature cubic $L2_1$ structure, which is taken as reference system in all discussions. These calculations yielded results being in agreement with existing experimental data for the atomic order, lattice parameters, magnetic moments and elastic constants. Tetragonal deformations of the $L2_1$ structure have led to another stable structure of Ni_2MnGa with $c/a > 1$, which is also known from the experimental investigations. The tetragonal structure has lower total energy compared to the $L2_1$ structure, as expected for the low-temperature case. The tetragonal phase represents a structure of a single martensitic domain (variant). This is the only martensitic structure of Ni_2MnGa, which still has a perfect symmetry. The other structures, along with the premartensitic one are known to be modulated. Some additional calculations with respect to the volume variation, tetragonal and orthorhombic deformations have been carried out in order to confirm the principal role of the atomic shuffles in Ni_2MnGa. The results obtained so far show that further calculations must be carried out on super-structures, which can accommodate more crystallographic unit cells of Ni_2MnGa with modulated shuffles of the atoms, that considered up to this point of the study. Chapter 5 presents results of calculations for Ni_2MnGa supercells obtained by taking into account atomic shuffles. The first and the most important result is the observation that the calculations yield a stable super-structure (5M) with modulated shuffles of the atoms. This structure has a tetragonal (in average) symmetry characterized by the ratio $c/a = 0.94$, which agrees perfectly with the experimental data. An analysis of the electronic structure shows that the stability of the modulation arises from a coupling of the minority-spin Ga-p-electrons and Ni-d-electrons, which occupy hybrid states right at the Fermi level. The shuffling is presented by a static wave of atomic displacements propagating along the [110] direction with polarizaton along $[1\bar{1}0]$. It has been argued that this modulation is related to specific nesting properties of the Fermi surface of Ni_2MnGa and the soft acoustic phonon mode [110]-TA_2, which is observed in Ni_2MnGa. Along with the modulation, the calculations revealed the existence of additional shuffles, which have an "optical" pattern of atomic displacements. Chapter 7 reports on the results of phonon calculations for two different non-modulated structures of Ni_2MnGa. The phonon spectra have been calculated for the [110] direction. The dispersion of phonons for the cubic

structure shows a complete softening of the transverse acoustic phonon mode [110]-TA_2 around the wave number [ζ ζ 0], for $\zeta = 1/3$, which corresponds to the wave vector of the premartensitic modulation. The soft mode frequency is imaginary in a wide range for $0.2 < \zeta < 0.5$, which implies an instability of the cubic structure against the modulation shuffling, the period of which is not well defined. Analysis of the vibrational density of states shows that there is a coupling between low-lying optical modes of Ni with acoustic modes [110]-TA_1 and [110]-LA. This coupling yields three different anomalies in the phonon dispersion. The wave vectors of these anomalies are those, which define periods of modulations in the 3M, 5M and 7M structure of Ni_2MnGa. The phonon dispersion calculated for the tetragonal structure with $c/a > 1$ shows no instability as predicted before. Chapter 8 deals with an off-stoichiometric structure $Ni_{8+1}Mn_{4-1}Ga_4$. The structure, in which every fourth atom of Mn is replaced by Ni, shows properties similar to the 5M structure, which was discussed in the previous chapters. Namely, the atomic disorder can stabilize the same (experimentally observed) tetragonal structure with $c/a = 0.94$ as the modulation. This allows to conclude that the stability of Ni_2MnGa in low temperature martensitic structures is related to several factors: Modulation, atomic disorder and, possibly, non-collinear magnetic order. But all these factors turn to stabilize the same effect with respect to the electronic structure of Ni_2MnGa, which yields the $c/a = 0.94$ ratio. This is rather intriguing and not yet completely understood. As discussed above, one important effect is the population of the minority-spin bands right at the Fermi level, which result from favourable Ga(p)- Ni(d) hybrid states.

A Appendix

A.1 Ginzburg-Landau theory for Ni-Mn-Ga

A.1.1 Introduction

Apart from the atomistic simulations discussed in this work we have investigated Ni_2MnGa and its alloys by using a Landau-type of description (Landau and Lifshitz, 1981) which allows to introduce appropriate order parameters for the different magneto-elastic transformations and which also allows to investigate in detail the symmetry changes associated with the transformations. In this approach, the difference in the free energies between the parent and the product phases is considered as a function of the order parameter, which is equal to zero in the high-symmetrical parent phase and becomes non-vanishing below the crytical point i.e., in the low-symmetry product phase. The symmetry group of the product phase is always a subgroup of the symmetry group of the parent phase.

It should be noted that Landau's theory in its general use only has the purpose to provide a phenomenological description, which may quantitatively not be correct in detail. However, it works rather well for displacive phase transitions, and it is possible to give a physical interpretation of the various parameters. An excellent short introduction to the Landau theory can be found in the book of Dove (Appendix D) (Dove, 1993). A more detailed description with real applications is given by Toledano and Toledano (1987) and Izyumov and Syromyatnikov (1990).

For a second-order phase transition, one can expand the Gibbs free energy, G, in a power series of the order parameter, Q, about $Q = 0$ and G_0:

$$G(Q) = G_0 + \frac{1}{2}aQ^2 + \frac{1}{4}bQ^4 + \dots \tag{A.1}$$

Terms with odd powers of Q are absent for the cases when the symmetry $G(-Q) = G(Q)$ must be preserved. The equilibrium value of Q is from the minimum of the free energy, G, giving the conditions for the extremum and stability:

$$\frac{\partial G}{\partial Q} = 0; \qquad \frac{\partial^2 G}{\partial Q^2} > 0. \tag{A.2}$$

When the coefficients a and b are both positive, $G(Q)$ has a single minimum at $Q = 0$, so that the free energy expansion describes the system in the high-symmetry phase in its equilibrium state. For a being negative and b still positive, $G(Q)$ has a maximum at $Q = 0$ and minima at $\pm Q_0$, so that the equilibrium state of the system is the low-symmetry phase. Since the sign of the coefficient a determines which phase is stable, we can assume a change of sign when cooling through the transition temperature T_C. This can simply be expressed by

$$a = \tilde{a}(T - T_C), \tag{A.3}$$

where $\tilde{a}$ is a positive constant. It is usualy assumed that the coefficient b and all higher order coefficients have a much weaker dependence on the temperature, so that they can be

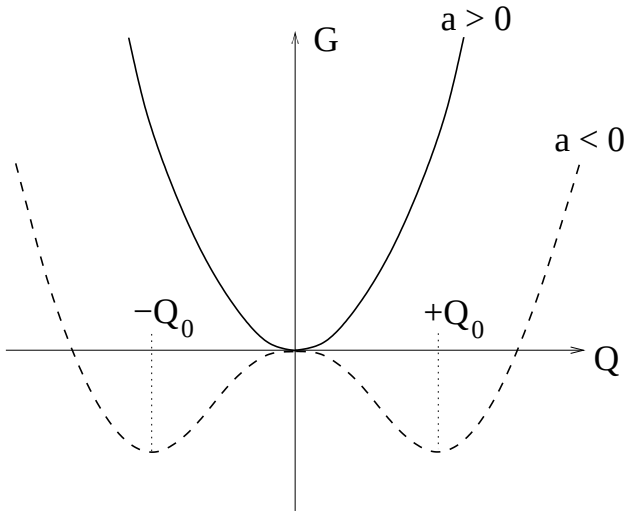

Figure A.1: Dependence of Gibbs free energy on the order parameter for the two cases: the solid line presents the case $a > 0$ when the high-symmetry phase is stable; the dashed line corresponds to the case of $a < 0$. i.e., when the minima of the free energy are at non-zero values of the order parameter Q.

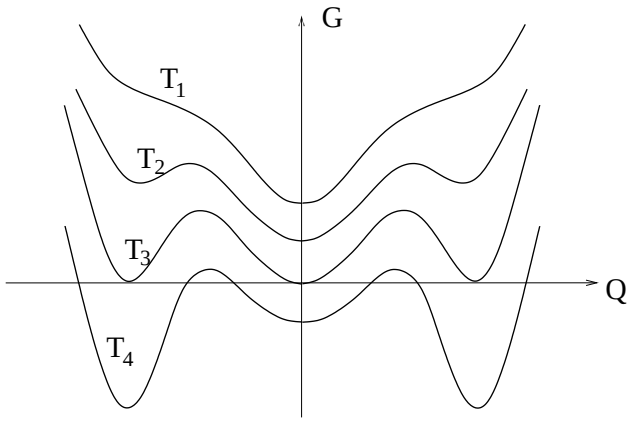

Figure A.2: Dependence of Gibbs free energy on the order parameter for different temperatures $T_1 > T_2 > T_3 > T_4$. For T_1 there is only one minimum of the energy. At T_2 two additional minima appear but still the high-temperature phase with $Q = 0$ is the most stable one. At T_3 all three minima have the same energy which corresponds to the point of phase transition. For T_4 the low-temperature phase is the most stable one with respect to the high-symmetry parent one.

considered to be approximately constant. With this assumption, the Landau free energy can be written as

$$G_L(Q) = \frac{1}{2}\tilde{a}(T - T_C)Q^2 + \frac{1}{4}bQ^4, \tag{A.4}$$

where the term G_0 is not taken into account.
The Landau free energy can be applied to first-order phase transitions when the quadratic term is negative and a higher-order term is also included giving

$$G_L(Q) = \frac{1}{2}\tilde{a}(T - T_C)Q^2 - \frac{1}{4}bQ^4 + \frac{1}{6}cQ^6. \tag{A.5}$$

In this case, a derivative of the free energy with respect to the order parameter gives a third order linear equation, the roots of which depend on the sign of its discriminant. Thus, $G_L(Q)$ has a single minimum at $Q = 0$ for $T > T_C + b^2/4\tilde{a}c$. Just below this temperature, $G_L(Q)$ has three minima at $Q = 0$ and $\pm Q_0$.

In many cases it is important to consider an order parameter which can interact with other (*secondary*) order parameters like the magnetization components or some additional distortion ε. The resultant behaviour depends on the symmetries of Q and ε. If they have the same symmetry, the two quantities can couple bilinearly in the free energy. Otherwise, the next-lowest coupling in the free energy will be between ε and Q^2.

The Landau free energy for the bilinear coupling is given as

$$G_L(Q) = \frac{1}{2}aQ^2 + \frac{1}{4}bQ^4 + \frac{1}{2}\eta\varepsilon Q + \frac{1}{2}C_{el}\varepsilon^2, \tag{A.6}$$

where η is the coupling constant, and C_{el} is the elastic constant in the absence of the coupling. The effect of bilinear coupling is to increase the transition temperature. The Landau free energy for quadratic coupling is given by

$$G_L(Q) = \frac{1}{2}aQ^2 + \frac{1}{4}bQ^4 + \frac{1}{2}\xi\varepsilon Q^2 + \frac{1}{2}C_{el}\varepsilon^2, \tag{A.7}$$

where ξ is the coupling constant. The effect of the quadratic coupling is to reduce the size of the coefficient of the quadratic term, such that if the coupling is sufficiently strong the quadratic coefficient becomes negative and the transition changes from second order to first order.

A.1.2 Application to Ni_2MnGa

The martensitic transformation which occurs in Ni_2MnGa belongs to the class of so-called *thermoelastic* phase transitions. This kind of transformation is characterized by the reversibility of a crystallographic structural change, i.e., the system regains its high-temperature state through the transition point upon heating. The reversibility of the transformation means that the phase transition takes place between equilibrium phases, whereby the structural coherence and the symmetry braking at a critical temperature imply that this transition can be analyzed within the frame of Landau theory (Fradkin, 1994). The fundamental difference of the structure of the martensitic phase with respect to the parent lattice is known to be related to the spontaneous strain (Roitburg, 1978). It means that the structural change takes place through the elastic instability of the crystalline lattice of the parent high-temperature phase with respect to a spontaneous homogeneous strain of some kind. This also means that some combination of the elastic moduli vanishes at the critical temperature (Falk and Konopka, 1990; Fradkin, 1994) giving rise to a softening of the corresponding acoustic phonon mode. Though the soft mode does not completely soften (at the transition temperature) meaning that the order parameter jumps at the transition upruptly, the martensitic phase transition may still be treated as a weakly discontinuous one and be considered in the frame of Landau theory, which is orriginaly is a theory of continious phase transitions.

A characteristic feature of Ni_2MnGa is that the Curie temperature T_C is higher than the temperature for the martensitic transition, T_M (Webster, Ziebeck, Town and Peak,

1984). Therefore, the influence of magnetic order on the martensitic transformation is of particular interest. Experimental data and approximate theoretical estimations show that the magnetic order in Ni-Mn-Ga alloys (with a composition close to the stoichiometric one) allows to induce the martensitic transformation by means of an external magnetic field (Bozhko, Vasil'ev, Khovailo, Dikshtein *et al.*, 1999). Another feature of Ni-Mn-Ga, which must be taken into account, is the existence of the intermediate modulated structure 3M between the parent $L2_1$ and the product martensitic phases. Moreover, the modulation exists also in the martensitic phases, 5M and 7M.

It is possible to discuss a phenomenological Ginzburg-Landau model (Fradkin, 1994; Gooding and Krumhansl, 1988) for the formation of the intermediate phase as well as for the martensitic transformations. In order to be as realistic as possible, experimental data can be used to fit the parameters of the theory. Since Landau theory in particular allows to discuss the symmetry changes at the transitions, it is possible to perform a detailed analysis of the magneto-structural coupling, which is needed in order to understand the influence of magnetic order on the martensitic transition and the intermediate phase.

The Landau theory allows to describe Ni_2MnGa as a cubic ferromagnet of O_h symmetry which undergoes a structural phase transformation from a high symmetry cubic phase to the low symmetry tetragonal D_{4h} phase. The symmetry group of the latter phase is a subgroup of the cubic one. In this case, the components of a macroscopic strain tensor e_{ik} can be considered as order parameters for the structural transformation. The magnetic state is described by the magnetization $\mathbf{M}$. A free-energy expansion is formulated in such a way that the functional is invariant under the actions $\hat{O}$ of the space group of the fcc phase of Ni-Mn-Ga ($\hat{O}(F) \to F$, $\hat{O} \in O_h$), leading to

$$\begin{aligned} F = &\frac{1}{2}(c_{11}+2c_{12})e_1^2 + \frac{1}{2}a(e_2^2+e_3^2) + \frac{1}{2}c_{44}(e_4^2+e_5^2+e_6^2) + \frac{1}{3}be_3(e_3^2-3e_2^2) \\ &+\frac{1}{4}c(e_2^2+e_3^2)^2 + \frac{1}{\sqrt{3}}B_1e_1\mathbf{m}^2 + B_2\left[\frac{1}{\sqrt{2}}e_2(m_x^2-m_y^2) + \frac{1}{\sqrt{6}}e_3(3m_z^2-\mathbf{m}^2)\right] \\ &+B_3\left(e_4m_xm_y + e_5m_ym_z + e_6m_zm_x\right) + K_1(m_x^2m_y^2 + m_y^2m_z^2 + m_x^2m_z^2) \\ &+\frac{1}{2}\alpha\mathbf{m}^2 + \frac{1}{4}\delta_1\mathbf{m}^4 - \mathbf{M_0H_0}, \end{aligned} \tag{A.8}$$

where the e_i are linear combinations of the strain tensor components e_{ik},

$$\begin{aligned} e_1 &= (e_{xx}+e_{yy}+e_{zz})/\sqrt{3}, \\ e_2 &= (e_{xx}-e_{yy})/\sqrt{2}, \\ e_3 &= (2e_{zz}-e_{xx}-e_{yy})/\sqrt{6}, \\ e_4 &= e_{xy},\ e_5 = e_{yz},\ e_6 = e_{zx}. \end{aligned} \tag{A.9}$$

In (A.8), a, b and c are linear combinations of the components of the second, third and

fourth order elasticity moduli, respectively, with (Fradkin, 1994):

$$\begin{aligned} a &= c_{11} - c_{12}, \\ b &= (c_{111} - 3c_{112} + 2c_{123})/6\sqrt{6}, \\ c &= (c_{1111} + 6c_{1112} - 3c_{1122} - 8c_{1123})/48, \end{aligned} \tag{A.10}$$

$\mathbf{m} = \mathbf{M}/M_0$ is the unit vector of the magnetization and M_0 the saturation magnetization; B_i are magnetostriction constants; K_1 is the first cubic anisotropy constant; α_1 and δ_1 are exchange parameters.

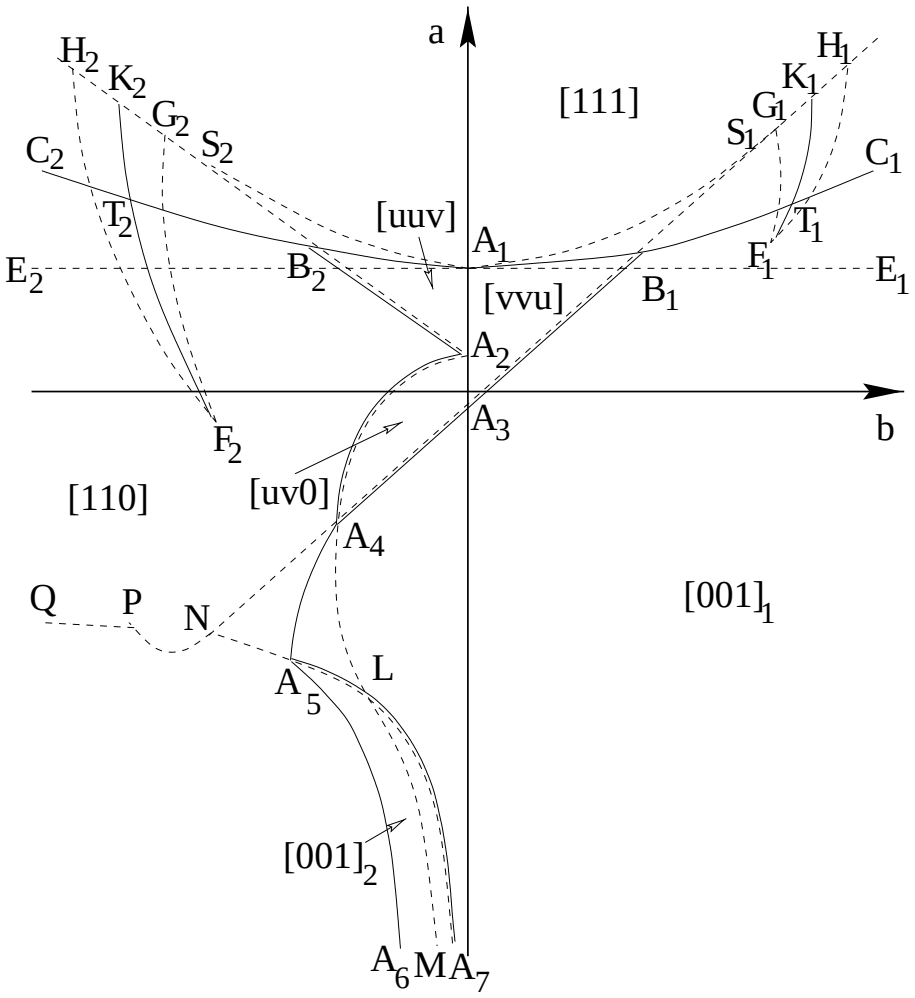

Figure A.3: Theoretical phase diagram of a ferromagnet which exhibits a magnetoelastic phase transformation from a cubic parent phase to one of the low-symmetry product phases.

A minimization of (A.8) with respect to the deformation tensor components e_1, e_4, e_5 and e_6, which are not responsible for the considered kind of structural transformation,

leads to a renormalization of the free energy parameters,

$$\begin{aligned}\delta &= \delta_1 - B_1^2/[6(c_{11}+2c_{12})],\\ K &= K_1 - B_3^2/2c_{44},\\ F_0 &= -B_1^2/[6(c_{11}+2c_{12})].\end{aligned} \tag{A.11}$$

Here we concentrate on the case $K < 0$, $B_2 > 0$ and $c > 0$.

It is difficult to minimize the free energy (A.8) analytically for all possible parameters. In order to obtain analytical results, one can consider the functional at the low-temperature limit. For $T \ll T_C$ and $M \approx M_0$ the exchange terms can be omitted, which leads a simpler form of the free energy expression:

$$\begin{aligned}F = F_0 + \frac{1}{2}a(e_2^2+e_3^2) + \frac{1}{3}be_3(e_3^2-3e_2^2) + \frac{1}{4}c(e_2^2+e_3^2)^2 + \\ B_2\left[\frac{1}{\sqrt{2}}e_2\sin^2\theta\cos 2\phi + \frac{1}{\sqrt{6}}e_3(3\cos^2\theta-1)\right] + \\ \frac{1}{4}K(\sin^4\theta\sin^2 2\phi + \sin^2 2\theta),\end{aligned} \tag{A.12}$$

where θ and ϕ are the polar and the azimuth angles of the magnetization vector.

A phase diagram (see Fig. A.3) for the low-temperature case with respect to the second and third order parameters of the free energy expansion (elastic moduli, a and b) has been obtained from an analytical minimization of (A.12). Exact solutions of all elements of the diagram have been reported by Buchelnikov *et al.* (1999). Here we present a brief analysis of the diagram. In Fig. A.3, all the phases are labeled with respect to corresponding easy magnetic axis. The solid lines mark the first order phase transitions, while the dashed lines show boundaries of the stability areas. The solid and dashed lines drawn close to each other mark second order phase transitions, where phase transitions and stability losses happen simultaneously.

Since, according to Landau theory, one can express the second order coefficient as $a = a_0(T - T_{\mathrm{M}})$, with T_{M} the critical temperature for the martensitic transformation, the process of cooling can be described by decreasing the parameter a. The parameter a_0 can be estimated from experimental data. Thus, in Fig. A.3 [111] denotes a high-temperature cubic phase with magnetic easy axis pointing along [111]. It is the only cubic phase in this diagram. If one decreases a by starting from the phase [111] the thermodynamic way corresponds to cooling. Below the dashed line $\mathrm{H_2K_2G_2S_2A_1S_1G_1K_1H_1}$ the strained structure appears, while the cubic phase exists above the dashed line $\mathrm{E_2E_1}$. In the area between $\mathrm{H_2K_2G_2S_2A_1S_1G_1K_1H_1}$ and $\mathrm{E_2E_1}$ two equlibrium states, cubic and strained, coexist. As a phase transition we consider the line $\mathrm{C_2C_1}$ on which the free energies of both phases are equal. There is a difference in representing the martensitic tranformation when discussing theory and experiments. In the latter case there are two transition points, T_{AM} and T_{MA}. Here, we say that T_{AM} corresponds to line $\mathrm{E_2E_1}$, and T_{MA} corresponds to line $\mathrm{H_2K_2G_2S_2A_1S_1G_1K_1H_1}$. The interval between these two lines is considered to be the hysteresis associated with the martensitic tranformation.

Depending on the sign and magnitude of b we obtain upon cooling different low temperature phases (with $c/a > 1$ or $c/a < 1$ for the tetragonal phases). Thus, the parameter b is of special interest. Since the strains e_i are roughly proportional to b/c, [1] (here, the elastic modulus c is kept constant). Consequently, decreasing b leads to smaller tetragonal distortions in the product phase. The line C_2B_2 marks a transition from the [111] phase to the tetragonal [110] phase. The line B_2A_1 is a transition from [111] to the angle phase [uuv] with magnetic easy axis rotating from [111] to [110] upon cooling and vice versa when heating. The line A_1B_1 represents a transition of the latter type but to the phase [vvu][2]. In this phase the easy axis rotates from [111] to $[001]_1$ upon cooling and vice versa upon heating. Rotation of the magnetic easy axes in the angular phases occurs due to a competition between the cubic anisotropy and the magnetostriction of the crystal. This kind of interaction takes place in the case of $K < 0$ (for the case $K > 0$ see (Buchelnikov, Vasilev, Zayak and Entel, 2001b; Buchelnikov, Zayak and Entel, 2002)). The line B_1C_1 is a phase transition from the cubic [111] phase to the tetragonal phase $[001]_1$. We note the difference between the cases $b > 0$ and $b < 0$. In the first case the cubic phase undergoes distortions which decrease the lattice parameter in direction [001] and increase the lattice parameters in the (001) plane (this corresponds to the tetragonality ratio $c/a < 1$). For the case of $b < 0$ the straines are of opposite kind ($c/a > 1$). We also note that a change of sign of B_2 leads to a symmetric reflection of the phase diagram with respect to the vertical axis "a". On the lines B_2A_2 and B_1A_3, rotations of the magnetic easy axes in the phases [uuv] and [vvu] are complete and second order spin reorientation transitions take place to the phases with fixed directions of magnetic easy axes [110] and $[001]_1$, respectively.

Inside the area $H_2F_2G_2$ there are two equilibrium tetragonal solutions for the martensitic phase [110]. The line K_2F_2 is a first order phase transition between the two tetragonal phases. Above the point T_2 this transition occurs between two metastable solutions, below this point - between two stable tetragonal martensitic phases. The same situation holds for the case $b > 0$ in the area $G_1H_1F_1$. The existence and the sizes of the both areas, $H_2F_2G_2$ and $G_1H_1F_1$, depend on a ratio of the ellastic constants and on the parameter of magnetostriction. The first order phase transitions on the lines K_2F_2 and K_1F_1 are of the isostructural type. From a mathematical point of view this is possible because we have three solutions inside the areas $H_2F_2G_2$ and $G_1H_1F_1$. As soon as $[001]_1$ and [110] are described by a cubic equation of state, inside of these areas the discriminants of the equation are negative. One can also say that these iso-structural transitions occur because of the anharmonisity in the free-energy expression (A.8). The phase [uv0] inside $A_2A_3A_4A_2$ is an intermediate one between the phases [110] and $[001]_1$. In this diagram we also observe spliting of the first order phase transition, line A_4A_5 into two second order phase transitions (lines A_2A_4 and A_3A_4) with a crytical point A_4. The phase [110] exists on the left of the dushed line $H_2K_2G_2S_2B_2A_2A_4LM$. The phase $[001]_1$ exists on the right of the line $H_1K_1G_1S_1B_1A_3A_4NA_5A_7$. The line A_5LA_7 is a second order phase transition

[1] It should be clear from the context when the parameter c denotes the third order elastic modulus or when it stands for the lattice constant along the z axis.

[2] In all notations for magnetization directions we assume that (u > v)

line between the phases $[001]_1$ and $[001]_2$, whereby the latter one has another type of symmetry. The phase $[001]_2$ exists below the line $QPNA_5LA_7$. The line A_5A_6 is a first order phase transition line between the phase [110] and the phase $[001]_2$. The line A_5A_7 is a second order phase transition line between the phases $[001]_1$ and $[001]_2$.

For the case of $T \ll T_C$ and $K < 0$ one can conclude that because of the symmetry breaking and the magneto-elastic coupling the martensitic transformation in a ferromagnet can be accompanied by a magnetic spinreorientation.

A.1.3 Extension to off-stoichiometric $Ni_{2+x}Mn_{1-x}Ga$

According to the experimental data (Vasil'ev, Bozhko, Khovailo, Dikshtein *et al.*, 1999a) the approximation $T \ll T_C$ is valid for the case of stoichiometric composition, Ni_2MnGa. However, it cannot be used for other compositions because the increase of Ni atoms causes both T_C and T_M to approach each other (see Fig. 2.8). In this case the low-temperature approximation cannot be used in the free energy expansion (A.8).

In order to obtain results which can be compared to the experimental data, we will deal with the temperature T and concentration x as the main parameters for $Ni_{2+x}Mn_{1-x}Ga$. Close to the critical points T_C and T_M the parameters a and α can be expressed as

$$\begin{aligned} a &= a_0(T - T_M), \quad \alpha = \alpha_0(T - T_C), \\ T_C &= T_{C0} - \gamma x, \quad T_M = T_{M0} + \sigma x. \end{aligned} \tag{A.13}$$

Here a_0, α_0, γ, σ are parameters which can be determined from the available experimental $(T,\ x)$ phase diagram obtained by (Vasil'ev, Bozhko, Khovailo, Dikshtein *et al.*, 1999a). T_{M0} and T_{C0} are the critical temperatures for Ni_2MnGa (i.e. for $x = 0$).

The following set of parameters can be used in order to bring the theory in accordance with experimental data for $Ni_{2+x}Mn_{1-x}Ga$: $b = 2.5 \cdot 10^{11}$ erg/cm^3, $c = 2.8 \cdot 10^{12}$ erg/cm^3, $K = -10^5$ erg/cm^3, $B_2 = 10^7$ erg/cm^3, $\delta = 10^9$ erg/cm^3, $H_0 = 0$, and with respect to (A.13), $a_0 = 9 \cdot 10^{10}$ erg/cm^3, $\alpha_0 = 10^9$ erg/cm^3, $T_{M0} = 200$ K, $T_{C0} = 375$ K, $\gamma = 175$ K, $\sigma = 700$ K.

A.1.4 Premartensitic transformation

Along with the martensitic transition, there is a premartensitic transformation of the high temperature phase into the intermediate 3M phase preceeding the transformation to the martensite structure. In this intermediate phase the parent cubic phase is modulated by transverse waves with wave vector $\mathbf{q}||[110]$ and polarization $\mathbf{i}||[1\bar{1}0]$ (TA_2 acoustic phonon branch) (Zheludev, Shapiro, Wochner and Tanner, 1996). Among the different wavelengths, there is a dominating 1/3[110] mode. The transformation from austenite to the intermediate phase is of weakly first-order.

According to an earlier theoretical proposal by Gooding and Krumhansl (1988) we consider the displacements of atoms according to the expression

$$\mathbf{u}(\mathbf{r}) = |\psi|\,\mathbf{i}\sin(\mathbf{k}\,\mathbf{r} + \phi), \tag{A.14}$$

with $\mathbf{k} = 1/3(1,1,0)$, $\mathbf{i} = (1,\overline{1},0)$; $|\psi|$ and ϕ as new order parameters. The expression for the free energy has to be completed by additional terms like $F_\psi(\psi)$, $F_{\psi m}(\psi,\mathbf{M})$ and $F_{\psi e}(\psi,e_i)$ defined by

$$F_\psi = \frac{1}{2}A|\psi|^2 + \frac{1}{4}B^0|\psi|^4 + \frac{1}{6}C_0|\psi|^6 + \frac{1}{6}C_1[\psi^6 + (\psi^*)^6], \tag{A.15}$$

$$F_{\psi m} = \left[\frac{1}{3}N_1^0\mathbf{m}^2 + N_2\left(m_z^2 - \frac{1}{3}\mathbf{m}^2\right) + N_3^0 m_x m_y\right]|\psi|^2, \tag{A.16}$$

$$F_{\psi e} = \left(\frac{1}{\sqrt{3}}D_1 e_1 + \frac{2}{\sqrt{6}}D_2 e_3 + D_3 e_4\right)|\psi|^2. \tag{A.17}$$

In expression (A.15) the term containing C_1 is minimized with respect to the phase ϕ. There is a minimum of (A.15) for $\phi = \pm\pi/6, \pm\pi/2, \pm 5\pi/6$ if $C_1 > 0$ and $\phi = 0, \pm\pi/3, \pm 2\pi/3, \pi$ if $C_1 < 0$. We will assume that C_1 is positive, B negative, A can be expressed as $A = A_0(T - T_\psi)$, where T_ψ is the critical temperature for the premartensitic transition. The full free energy expansion is then of the form,

$$\begin{aligned} F = F_0 + F_e(e_i) + F_\psi(\psi) + F_{\psi e}(\psi,e_i) + F_{\psi m}(\psi,m_i) + \\ F_{me}(m_i,e_j) + F_a(m_i) + F_{\psi m}(m_i,\psi) + F_{ex}(m_i). \end{aligned} \tag{A.18}$$

An analytical minimization of (A.18) with respect to the components of the deformation tensor, e_1 and e_{4-6}, leads to a renormalization of the parameters in Eqs. (A.15), (A.16) and (A.17) yielding $B = B^0 - 2D_3^2/c_{44} - 2D_1^2/3(c_{11}+2c_{12})$, $N_1 = N_1^0 - D_1B_1/6(c_{11}+2c_{12})$, $N_3 = N_3^0 - B_3D_3/c_{44}$. For other coefficients the renormalization is the same as in Section A.1.2. Coefficients N_1, N_2, N_3, D_2, which are responsible for the interaction of the modulation order parameter with other order parameters, can be estimated from a fit to experimental data.

We have now to minimize a functional with six order parameters. The additional parameter $|\psi|$ does not complicate the minimization procedure. The calculations were performed by assuming that $|\psi|$ is of the order of or less than $|\mathbf{u}|$, which means $|\psi| \approx 10^{-8}$ cm. Consequently, the coefficients in (A.15) are $A = 10^{23}$ erg/cm^3, $B = -10^{39}$ erg/cm^3, $C = C_0 + C_1 = 10^{55}$ erg/cm^3. These parameters are valid for the case that F_e and F_ψ in (A.18) are of the same order of magnitude.

The phase diagram obtained on the basis of Eq. (A.18) is shown in Fig. A.4 (to be compared with Fig. 2.8). In this diagram the dotted line LL' shows a first-order phase transition to the phase with modulated structure, while a part of it denoted by LF corresponds to the premartensitic phase transition. The existence of this transition is supported by the experimental data. The line FL' marks the transition to the modulated structure within the martensitic phase. However, there is no experimental evidence for this kind of transformation. There is little chance to find the theoretical line FL' in experiments because a realistic martensitic structure with different variants might not allow for this phase transition.

The phase FC[111] exists inside the area AMSRVUXP. The area of stability for FT[001] is marked by P'UXWMM'TN'A'. The phase FCM[vvu] is stable in the regions

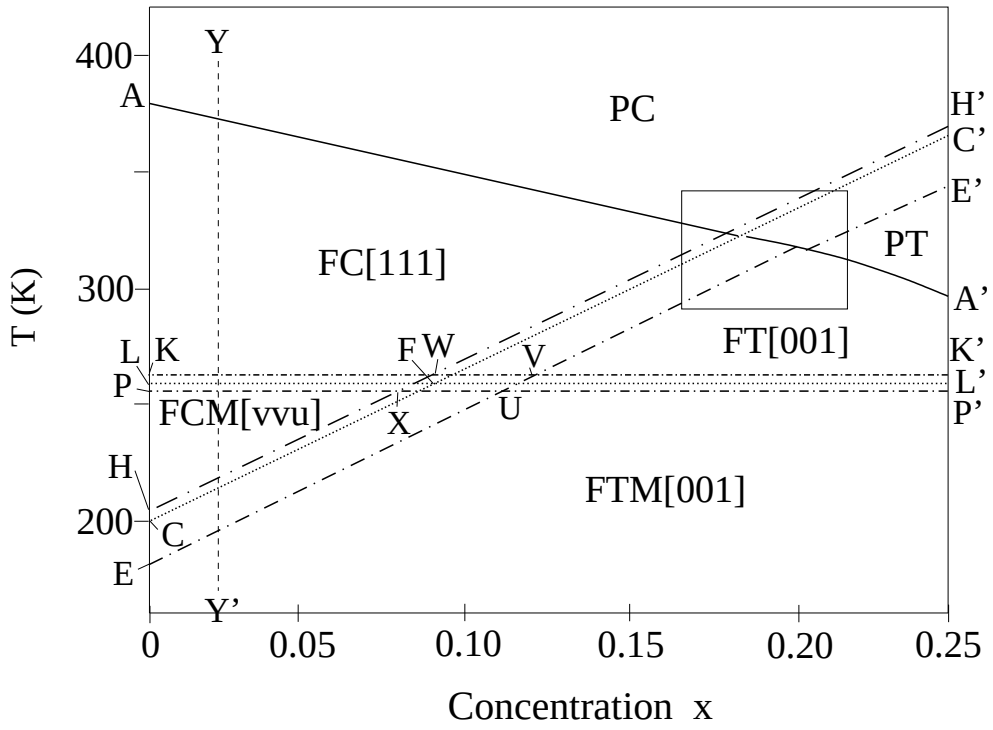

Figure A.4: Theoretical phase diagram of ferromagnetic $Ni_{2+x}Mn_{1-x}Ga$ in the (T, x) plane for the case that a the modulated structure has been taken into account. The dotted line represents first-order phase transitions; dash-dotted lines are the stability boundaries; the solid line represents phase transitions of second order. The phases are labeled as P: paramagnetic state, C: cubic lattice, F: ferromagnetic state and T: tetragonal lattice, M refers to the modulated structure.

KWVUE and FTM[001] below the line HXWVK'. The intermediate phase FCM[vvu] shows the modulation defined in (A.14). It is worthwhile to mention that the interaction associated with the parameter D_2 ensures the coupling between the modulation and the homogeneous tetragonal strain defined by (A.17) and accounts in the intermediate structure for the non-vanishing tetragonal distortion along with the modulation. Because of the smallness of this tetragonal distortion this intermediate phase is quasi-cubic. For the case that b and D_2 have the same sign the intermediate premartensitic and martensitic phases show the same type of tetragonal distortion. This case corresponds to the phase diagram shown in Figure A.4, where the intermediate phase is labeled by FCM[vvu]. If these parameters have different signs then the tetragonal distortions have a complicated character: The martensitic transformation can show a larger hysteresis and the intermediate phase must be labeled by FCM[uuv] ($u > v$). If the interaction defined by the coefficient D_2 is large enough, an additional magnetic phase transition occurs: A second-order transition from FCM[uuv] to FCM[110] and, a subsequent martensitic transformation from FCM[110] to FTM[001]. In order to emphasize the difference between the phases with [001] and [110] directions for the magnetization vector, we refer to the (a, b) phase diagram shown in Fig. A.3. Thus, one can conclude that, because of magnetostriction, the weak tetragonal distortion changes the magnetic order in the in-

termediate phase, whereby details of it depend on the values and signs of the coefficients D_2 and $N_{1,2,3}$.

The phases shown in Fig. A.4 have been obtained by using the following parameters: $D_2 = 10^3$ erg/cm^3, $N_1 = 10^3$ erg/cm^3, $N_2 = -10^2$ erg/cm^3, $N_3 = -10^2$ erg/cm^3. These values, together with values for the other parameters given above, yield more of less a realistic behaviour of the order parameters. For example, Fig. A.5 shows the temperature dependence of the components of the magnetization taken along the line YY' (in Fig. A.4) with the following transition temperatures: the Curie temperature, $T_C = 375$ K; the temperature for the transition to the modulated structure, $T_\psi = 260$ K, and the structural transition to the tetragonal phase, $T_M = 220$ K. For $T > 375$ K the paramagnetic state (PC) is stable, whereas for 260 K $< T <$ 375 K the ferromagnetic state with $\mathbf{M} \parallel [111]$ is stable. For 220 K $< T <$ 260 K the magnetic order changes because of the deformations in the premartensitic phase, while for $T <$ 220 K the magnetic order is the one of the tetragonal phase FTM[001]. Note, that the dependence of the magnetic order in the premartensitic phase depends on the parameters $N_{1,2,3}$.

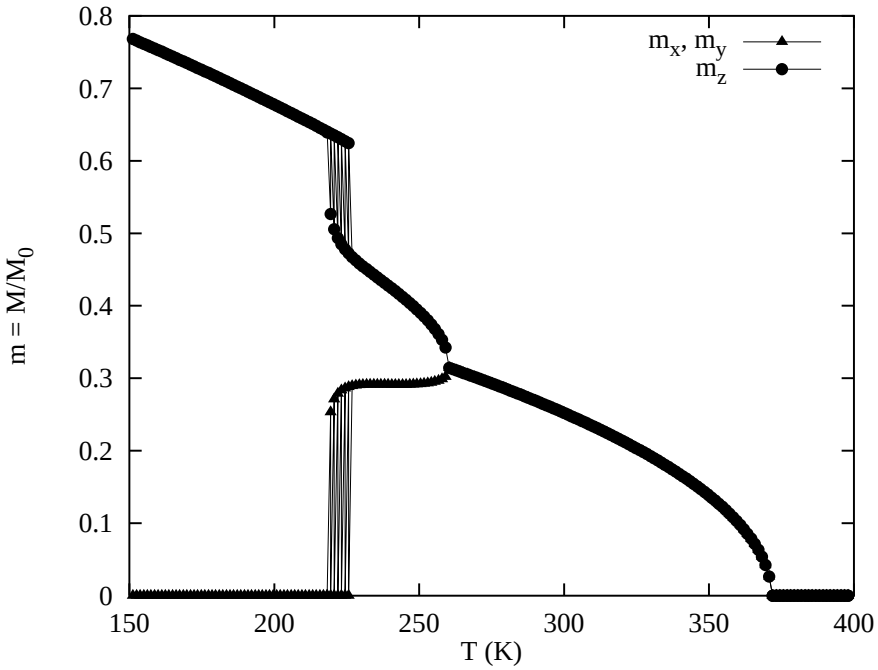

Figure A.5: Dependence of the dimensionless magnetization components on temperature for $Ni_{2+x}Mn_{1-x}Ga$ with $x = 0.02$ along the line YY' in Fig. A.4.

Different sets of parameters $N_{1,2,3}$ lead to modifications of the magnetic order in the modulated structures. The role of the parameter N_1 is connected with a renormalization of the exchange parameter α by $\alpha' = \alpha + N_1|\psi|^2$. The parameter N_2 controls a magnetostriction-like effect; its sign determines which kind of magnetic phase exists, $\mathbf{m} \in$ [vvu] or $\mathbf{m} \in$ [uuv] according to (u > v). If the parameter N_2 is large enough, it can cause an additional magnetic spin-reorientation transition inside the intermediate phase.

N_3 is also an interesting parameter. For $N_3 < 0$ the sign of m_x is equal to that of m_y. For the case of $N_3 > 0$ the x and y components of the magnetization have opposite. The role of this term will become more important whenever the phonon-magnon coupling is considered in addition.

A detailed analysis of all possible configurations in the $(T,\ x)$ phase diagram would require a much longer discussion. In this work we concentrated on a few results which have been obtained on the basis of a Ginzburg-Landau formulation. An extension of the present treatment will have to take into account external fields. Also according to (O'Handley, 1998) one can consider simple structural and magnetic domains within the framework of the Ginzburg-Landau theory. This would allow to describe the large magnetostrictive deformations occurring in Ni-Mn-Ga, see (Murray, Marioni, Kukla, Robinson *et al.*, 2000).

In conclusion, the theory presented here allows to describe structural, magnetic and coupled magneto-structural transitions of first- and second-order in a cubic ferromagnet like Ni-Mn-Ga. Magneto-structural interactions lead to a variety of different equilibrium states. If the Curie temperature happens to lie inside the hysteresis of the martensitic transformation, then the magnetic disorder-order transition is of first order. For $Ni_{2+x}Mn_{1-x}Ga$ this situation occurs only for a very narrow range of compositions. The size of this range depends on the value of the magnetostriction. A phenomenological description of the premartensitic transition is also possible, however, there are no experimental data available for a correct determination of the Landau parameters, D_2 and $N_{1,2,3}$, which leads to some ambiguity when fixing the equilibrium conditions. One possible way to improve this model is to combine it with results obtained from first-principles calculations.

Acknowledgments

First of all I would like to thank my thesis supervisor, Prof. Dr. Peter Entel, for an opportunity to do my PhD work in his group at the University of Duisburg. I thank him for the freedom which I was given to choose a subject to investigate and methods to use. I am very grateful for his continuous assistance and the encouragement shown to my work. I thank him for all the helpful discussions and the full support in everything I needed in order to progress through this investigation. Also I must mention the particular human respect and care he has shown to me in the course of this research.

I very much thank my colleagues in the group for the pleasant atmosphere in the whole department and a lot of discussions not only concerning my work. I am particularly grateful to Egbert Hoffmann and Dr. Heike Herper for their assistance with my calculations at the beginning of my work. I also thank Dr. Ralf Meyer for his patience with those plenty of questions which I addressed to him of different subjects of my work and life. Especially I have to mention Markus Gruner who always was the first I approached when having problems. With respect to the computer facilities I always obtained a full support from the system administrator of our group, Dr. Fred Hucht.

Much care was taken of me by Dr. Andrei Postnikov. He managed to explain in easy words the most complicated aspects of electronic structure calculations. His opinion was a guideline to my work all the time. Some parts of this study are based on ideas kindly proposed by Andrei in our discussions.

I am grateful for very productive and nice cooperation with Dr. Andres Ayuela and Dr. Jussi Enkovaara who worked at the Helsinki University of Technology when I was doing my thesis work. Discussions with them provided a lot of information about the system I have been studying.

I also thank Prof. Dr. Vasiliy Buchelnikov who worked with me during my studies in Russia. He has completely changed my life encouraging me to work in physics.

I acknowledge the financial support of the Deutsche Forschungsgemeinschaft (Graduiertenkolleg 277) which allowed me to stay in Germany during three years and work under optimal conditions.

References

Aaltio, I. and K. Ullakko (2000). Magnetic shape memory (MSM) actuators. In *Proceedings of the 7th International Conferenc on New Actuators, ACTUATOR 2000*, 45. Bremen, Germany.

Alder, B. J. and T. E. Wainwright (1957). Phase transition for a hard sphere system. *J. Chem. Phys.* **27**, 1208.

Ayuela, A. and J. Enkovaara (2003). private communications.

Ayuela, A., J. Enkovaara and R. M. Nieminen (2002). *Ab initio* study of tetragonal variants in Ni_2MnGa alloy. *J. Phys.: Condens. Matter* **14**, 5325.

Ayuela, A., J. Enkovaara, K. Ullakko and R. Nieminen (1999). Structural properties of magnetic Heusler alloys. *J. Phys.: Condens. Matter* **11**, 2017.

Blöchl, P. (1994). Projector augmented-wave method. *Phys. Rev. B* **50**, 17953.

Born, M. and H. Kun (1988). *Dynamical Theory of Crystal Lattices*. Clarendon Press, Oxford.

Bozhko, A., A. Vasil'ev, V. Khovailo, I. Dikshtein *et al.* (1999). Magnetic and structural phase transitions in the shape-memory ferromagnetic alloys $Ni_{2+x}Mn_{1-x}Ga$. *JETP* **88**, 957.

Brown, P. J., J. Crangle, T. Kanomata, M. Matsumoto *et al.* (2002). The crystal structure and phase transitions of the magnetic shape memory compound Ni_2MnGa. *J. Phys.: Condens. Matter* **14**, 10159.

Buchel'nikov, V., V. Romanov, A. Vasil'ev, T. Takagi *et al.* (2001). Model of colossal magnetostriction in the martensite phase of Ni-Mn-Ga alloys. *JETP* **93**, 1302.

Buchelnikov, V., A. Zayak, A. Vasil'ev, D. Dalidovich *et al.* (2001a). Phase transitions in ferromagnetic alloys $Ni_{2+X}Mn_{1-X}Ga$ with regard for the modulation order parameter. *JETP* **92**, 1010.

Buchelnikov, V. D., V. S. Romanov and A. T. Zayak (1999). Structural phase transitions in cubic ferromagnets. *J. Magn. Magn. Mater.* **191**, 203.

Buchelnikov, V. D., A. N. Vasilev, A. T. Zayak and P. Entel (2001b). The influence of magnetoelastic interaction on structural phase transitions in cubic ferromagnets. *JETP* **92**, 1019.

Buchelnikov, V. D., A. T. Zayak and P. Entel (2002). Magnetoelastic influence on structural phase transitions in cubic ferromagnets. *J. Magn. Magn. Mater.* **242-245**, 1457.

Campbell, C. C. M. (1975). Hyperfine field systematics in Heusler alloys. *J. Phys. F* **5**, 1931.

Castan, T., E. Vives and P.-A. Lindgard (1999). Modeling premartensitic effects in Ni_2MnGa: A mean-field and Monte Carlo simulation study. *Phys. Rev. B* **60**, 7071.

Cesari, E., V. Chernenko, V. Kokorin, J. Pons *et al.* (1997). Internal friction associated with the structural phase transformations in Ni-Mn-Ga alloys. *Acta Mater.* **45**, 999.

Chernenko, V. (1999). Compositional instability of β-phase in Ni-Mn-Ga alloys. *Scripta Materialia* **40**, 523.

Cochran, W. (1973). *Dynamics of Atoms in Crystals*. Edward Arnold, London.

Corso, A. D., A. Pasquarello, A. Baldereschi and R. Car (1996). Generalized-gradient approximations to density-functional theory: A comparative study for atoms and solids. *Phys. Rev. B* **53**, 1180.

Dove, M. T. (1993). *Introduction to Lattice Dynamics*. Cambridge University Press, Cambridge.

Enkovaara, J. (2003). Atomistic simulations of magnetic shape memory alloys. Ph.D. thesis, Helsinki University of Technology.

Enkovaara, J., A. Ayuela, J. Jalkanen, L. Nordström *et al.* (2003a). First-principles calculations of spin spirals in Ni_2MnGa and Ni_2MnAl. *Phys. Rev. B* **67**, 054417.

Enkovaara, J., A. Ayuela, L. Nordström and R. M. Nieminen (2002a). Magnetic anisotropy in Ni_2MnGa. *Phys. Rev. B* **65**, 134422.

Enkovaara, J., A. Ayuela, L. Nordström and R. M. Nieminen (2002b). Structural, termal, and magnetic properties of Ni_2MnGa. *J. Appl. Phys.* **91**, 7798.

Enkovaara, J., O. Heczko, A. Ayuela and R. M. Nieminen (2003b). Coexistance of ferro- and antiferromagnetic order in Mn-doped Ni_2MnGa. *Phys. Rev. B* **67**, 212405.

Falk, F. and P. Konopka (1990). Three-dimentional Landau theory describing the martensitic phase transformation of shape-memory alloys. *J. Phys.: Cond. Matter* **2**, 61.

Fradkin, M. (1994). External field in the Landau theory of a weakly discontinuous phase transition: Pressure effect in the martensitic transitions. *Phys. Rev. B* **50**, 16326.

Fritsch, G., V. V. Kokorin and A. Kempf (1994). Soft modes in Ni_2MnGa single crystals. *J. Phys.: Condens. Matter* **6**, L107.

Godlevsky, V. and K. Rabe (2001). Soft tetragonal distortions in ferromagnetic Ni_2MnGa and related materials from first principles. *Phys. Rev. B* **63**, 134407.

Gonis, A., editor (2000). *Theoretical material science: Tracing the electronic origins of materials behavior*. Materials Research Society.

Gonzalez-Comas, A., E. Obrado, L. Mañosa, A. Planes *et al.* (1999). Magnetoelasticity in the Heusler Ni_2MnGa alloy. *J. Magn. Magn. Mater.* **196–197**, 637.

Gooding, R. and J. Krumhansl (1988). Theory of the bcc-to-9R structural phase transformation of Li. *Phys. Rev. B* **38**, 1695.

Gooding, R. J. and J. A. Krumhansl (1989). Symmetry-restricted anharmonicities and the CsCl-to-7R martensitic structural phase transformation of the Ni_XAl_{1-X} system. *Phys. Rev. B* **39**, 1535.

Grüner, G. (1988). The dynamics of charge-density waves. *Rev. Mod. Phys.* **60**, 1129.

Harrison, W. A. (1980). *Electronic Structure and the Properties of Solids: the physics of the chemical bond*. W. H. FREEMAN AND COMPANY.

Harrison, W. A. and C. J. Phillips (1974). un. *Phys. Rev. Lett.* **33**, 410.

Heusler, F. (1903). *Verh. Dtsch. Phys. Ges.* **5**, 219.

Horton, G. K. and A. A. Maradudin (1974). *Dynamical Properties of Solids*. North-Holland Publishing Company, Amsterdam.

Izyumov, Y. and V. Syromyatnikov (1990). *Phase Transitions and Crystall Symmetry*. Kluwer Acad. Publ., New York.

Jin, X., M. Marioni, D. Bono, S. M. Allen *et al.* (2002). Empirical mapping of Ni-Mn-Ga properties with composition and valence electron concentration. *J. Appl. Phys.* **91**, 8222.

Kadau, K., T. C. Germann, P. S. Lomdahl and B. L. Holian (2002). Microscopic wiev of structural phase transitions induced by shock waves. *Science* **296**, 1681.

Kagoshima, S., H. Nagasawa and T. Sambongi, editors (1988). *One-dimentional conductors*. Springer-Verlag, Berlin. Chapter 2.

Khovailo, V., T. Takagi, A. Bozhko, M. Matsumoto *et al.* (2001). Premartensitic transition in $Ni_{2+X}Mn_{1-X}Ga$ Heusler alloys. *J. Phys.: Condens. Matter* **13**, 9655.

King-Smith, R. D. and R. J. Needs (1990). A new and efficient scheme for first-principles calculations of phonon spectra. *J. Phys.: Cond. Matter* **2**, 3431.

Kokorin, V., V. Chernenko, J. Pons, C. Segu *et al.* (1997). Acoustic phonon mode condensation in Ni_2MnGa compound. *Solid State Commun.* **101**, 7.

Kresse, G. and J. Furthmüller (1996). Efficient iteative schemes for *ab initio* total energy calculations using a plane-wave set. *Phys. Rev. B* **54**, 11169.

Kresse, G. and D. Joubert (1999). From ultrasoft pseudopotentials to the projector augmented-wave method. *Phys. Rev. B* **59**, 1758.

Kübler, J., A. Williams and C. Sommers (1983). Formation and coupling of magnetic moments in Heusler alloys. *Phys. Rev. B* **28**, 1745.

Kunc, K. and R. M. Martin (1982). *Ab initio* force constants of gaas: A new approach to calculation of phonons and dielectric properties. *Phys. Rev. Lett.* **48**(6), 406.

Landau, L. D. and E. M. Lifshitz (1981). *Statistical Physics*. Pergamon, Oxford, 3rd edition.

Lee, Y., J. Y. Rhee and B. N. Harmon (2002). Generalized susceptibility of the magnetic shape-memory alloy Ni_2MnGa. *Phys. Rev. B* **66**, 054424.

L'vov, V., E. Gomonaj and V. Chernenko (1998). A phenomenological model of ferromagnetic martensite. *J. Phys.: Condens. Matter* **10**, 4587.

MacLaren, J. M. (2002). Role of alloying on the shape memory effect in Ni_2MnGa. *J. Appl. Phys.* **91**, 7801.

Mañosa Ll., A. Gonzalez-Comas, E. Obrado and A. Planes (1999). Premartensitic phase transformation in the Ni_2MnGa shape memory alloy. *Mater. Science and Engineering A* **273–275**, 329.

Mañosa Ll., A. Gonzalez-Comas, E. Obrado, A. Planes *et al.* (1997). Anomalies related to the TA_2-phonon-mode condensation in the Heusler Ni_2MnGa alloy. *Phys. Rev. B* **55**, 11068.

Mañosa Lluis, A. Planes, J. Zarestky, T. Lograsso *et al.* (2001). Phonon softening in Ni-Mn-Ga alloys. *Phys. Rev. B* **64**, 024305.

Martynov, V. and V. Kokorin (1992). The crystal structure of thermally- and stress-induced martensites in Ni_2MnGa single crystals. *J. Phys. III (France)* **2**, 739.

Metropolis, N., A. W. Rosenbluth, M. N. Rosenbluth, H. T. A *et al.* (1953). Equation of state calculation by fast computing mashines. *J. Chem. Phys.* **21**, 1087.

Morito, S. and K. Otsuka (1996). Electron microscopyof new martensites with long period staking order structures in $Ni_{50}Al_xMn_{50-x}$ alloys. *Mater. Science of Engineering A* **208**, 47.

Murnaghan, F. D. (1944). The compressibility of media under extreme pressures. *Proc. National Acad. Sci. USA* **3**, 244.

Murray, S., M. Farinelli, C. Kantner, J. Huang *et al.* (1998). Field-induced strain under load in Ni-Mn-Ga magnetic shape memory materials. *J. Appl. Phys.* **83**, 7297.

Murray, S., M. Marioni, A. Kukla, J. Robinson *et al.* (2000). Large field induced strain in single crystalline Ni-Mn-Ga ferromagnetic shape memory alloy. *J. Appl. Phys.* **87**, 5774.

Nishiyama, Z. (1978). *Martensitic Transformations*. Academic Press, New York.

O'Handley, R. (1998). Model for strain and magnetization in magnetic shape-memory alloys. *J. Appl. Phys.* **83**, 3263.

O'Handley, R. C., S. J. Murray, M. Marioni, H. Nembach *et al.* (2000). Phenomenology of giant magnetic-field-induced strain in ferromagnetic shape-memory materials. *J. Appl. Phys.* **87**, 4712.

Otsuka, K. and T. Kakeshita (2002). Science and technolgy of shape-memory alloys: New developments. In *MRS Bulletin*. www.mrs.org/publications/bulletin.

Overholser, R., M. Wutting and D. Neumann (1999). Chemical ordering in Ni-Mn-Ga Heusler alloys. *Scripta Materialia* **40**, 1095.

Parlinski, K. (2002). Phonon. Cracow, Poland. Software, version 3.11.

Parlinski, K., Z.-. Q. Li and Y. Kawazoe (1997). First-principles determination of the soft mode in cubic ZrO_2. *Phys. Rev. Lett.* **78**, 4063.

Perdew, J. P. (1992). Atoms, molecules, solids, and surfaces: Application of the generalized gradient approximation for exchange and correlation. *Phys. Rev. B* **46**, 6671.

Planes, A., E. Obrado, A. Gonzales-Comas and Ll. Mañosa (1997). Premartensitic transition driven by magnetoelastic interaction in bcc ferromagnetic Ni_2MnGa. *Phys. Rev. Lett.* **79**, 3926.

Roitburg, A. L. (1978). Solid State Physics. In H. Ehrenreich, F. Seitz and D. Turnbull, editors, *Advances in Research and Applications*, volume 33, 317. Academic Press, New York.

Roothaan, C. C. J. (1951). New developments in molecular-orbital theory. *J. Chem. Phys.* **23**, 69.

Schlagel, D., Y. Wu, W. Zhang and T. Lograsso (2000). Chemical segregation during bulk single crystal preparation of Ni-Mn-Ga ferromagnetic shape memory alloys. *J. Alloys and Compounds* **312**, 77.

Schütt, O., P. Pavone, W. Windl, K. Karch *et al.* (1994). *Ab initio* lattice dynamics and charge fluctuations in alkaline-earth oxides. *Phys. Rev. B* **50**(6), 3746.

Söderling, P., O. Eriksson, J. M. Wills and A. M. Boring (1993). Theory of elastic constants of cubic transition metals and alloys. *Phys. Rev. B* **48**, 5844.

Singh, D. J. (1994). *Planewaves, Pseudopotentials and the LAPW Method*. Kluwer Academic Publishers, Boston.

Singleton, J. (2001). *Band Theory and Electronic Properties of Solids*. Oxford Masters Series in Condensed Matter Physics. Oxford University Press, Oxford.

Springborg, M. (2000). *Methods of Electronic-Structure Calculations: From Molecules to Solids*. WILEY.

Srivastava, G. P. (1990). *The Physics of Phonons*. Adam Hilder (IOP Publishing Ltd), New York.

Stenger, T. and J. Trivisonno (1998). Ultrasonic study of the two-step martensitic phase transformation in Ni_2MnGa. *Phys. Rev. B* **57**, 2735.

Stuhr, U., P. Vorderwisch, V. Kokorin and P.-A. Lindgard (1997). Premartensitic phenomena in the ferro- and paramagnetic phases of Ni_2MnGa. *Phys. Rev. B* **56**, 14360.

Takeuchi, I., O. O. Famodu, J. C. Read, M. A. Aronova *et al.* (2003). Identification of novel compositions of ferromagnetic shape-memory alloys using composition spreads. *Nature Mater.* **2**, 180.

Tickle, R. and R. James (1999). Magnetic and magnetomechanical properties of Ni_2MnGa. *J. Magn. Magn. Mater.* **195**, 627.

Toledano, J.-C. and P. Toledano (1987). *The Landau theory of phase transitions*. World Scientific, Singapore.

Ullakko, K., J. K. Huang, C. Kantner, R. C. O'Handley *et al.* (1996). Large magnetic-field-induced strains in Ni_2MnGa single crystals. *Appl. Phys. Lett.* **69**, 1966.

Ullakko, K., A. Sozinov and P. Yakovenko (2000). Large magnetic-field induced strains in Ni-Mn-Ga alloys due to redistribution of martensitic variants. Cond-mat/0004211.

Vanderbilt, D. (1990). Soft self-consistent pseudopotentials in a generalized eigenvalue formalism. *Phys. Rev. B* **41**, 7892.

Vasil'ev, A., A. Bozhko, V. Khovailo, I. Dikshtein *et al.* (1999a). Structural and magnetic phase transitions in shape-memory alloys $Ni_{2+x}Mn_{1-x}Ga$. *Phys. Rev. B* **59**, 1113.

Vasil'ev, A., A. Bozhko, V. Khovailo, I. Dikshtein *et al.* (1999b). Structural and magnetic phase transitions in shape memory alloys $Ni_{2+X}Mn_{1-X}Ga$. *J. Magn. Magn. Mater.* **196–197**, 837.

Vasil'ev, A., A. Keiper, V. Kokorin, V. Chernenko *et al.* (1994). The structural phase transitions in Ni_2MnGa induced by low-temperature uniaxial stress. *Int. J. of Applied Electromagnetics in Materials* **5**, 163.

Vasil'ev, A. N., V. V. Kokorin, Y. I. Savchenko and V. A. Chernenko (1990). The magnetoelastic properties of a Ni_2MnGa single crystal. *JETP* **71**, 803.

Velikokhatnyi, O. and I. Naumov (1999). Electronic structure and instability of Ni_2MnGa. *Phys. Solid State* **41**, 617.

von Barth, U. and L. Hedin (1972). A local exchange-correlation potential for the spin polarized case: I. *J. Phys. C* **5**, 1629.

Webster, P., K. Ziebeck, S. Town and M. Peak (1984). Magnetic order and phase transformation in Ni_2MnGa. *Phil. Mag.* **49**, 295.

Webster, P. J. (1969). Heusler alloys. *Contemp. Phys.* **10**, 559.

Webster, P. J. (1971). Magnetic and chamical order in Heusler alloys containing cobalt and manganese. *J. Phys. Chem. Solids* **32**, 1221.

Wei, Z. and G.Engdahl (2000). Design and simulation of magnetic shape memory and magnetostrictive actuators. In *Proceedings of the 7th International Conferenc on New Actuators, ACTUATOR 2000*, 42. Bremen, Germany.

Wood, W. W. and J. D. Jacobsen (1957). Preliminary results from a recalculation of the Monte-Carlo equation of state of hard spheres. *J. Chem. Phys.* **27**, 1207.

Worgull, J., E. Petti and J. Trivisonno (1996). Behavior of the elastic properties near an intermediate phase transition in Ni_2MnGa. *Phys. Rev. B* **54**, 15695.

Wu, G., C. Yu, L. Meng, J. Chen *et al.* (1999). Giant magnetic-field-induced strains in Heusler alloy NiMnGa with modified composition. *Appl. Phys. Lett.* **75**, 2990.

Zayak, A., V. Buchelnikov and P. Entel (2002). A Ginzburg-Landau theory for Ni-Mn-Ga. *Phase Transitions* **75**, 243.

Zayak, A., P. Entel and J. Hafner (2003a). A first-principles investigation of tetragonal and orthorhombic deformations in the ferromagnetic Heusler alloy Ni_2MnGa. *Journal de Physique IV: International conference on martensitic transformations ICOMAT'02* To appear.

Zayak, A. T., P. Entel, J. Enkovaara, A. Ayuela *et al.* (2003b). A first-principles investigation of phonon softenings and lattice instabilities in the shape-memory system Ni_2MnGa. *Phys. Rev. B* To appear, cond-mat/0304315.

Zayak, A. T., P. Entel, J. Enkovaara, A. Ayuela *et al.* (2003c). First-principles investigations of homogeneous lattice-distortive strain and shuffles in Ni_2MnGa. *J. Phys.: Condens. Matter* **15**, 159.

Zhao, G. L. and B. N. Harmon (1992). Phonon anomalies in β-phase Ni_xAl_{1-x} alloys. *Phys. Rev. B* **45**, 2818.

Zheludev, A. and S. Shapiro (1996). Uniaxial stress dependence of the $(\zeta\zeta 0)-$ TA_2 anomalous phonon branch in Ni_2MnGa. *Solid State Commun.* **98**, 35.

Zheludev, A., S. Shapiro, P. Wochner, A. Schwartz *et al.* (1995). Phonon anomaly, central peak, and microstructures in Ni_2MnGa. *Phys. Rev. B* **51**, 11310.

Zheludev, A., S. Shapiro, P. Wochner and L. Tanner (1996). Precursor effects and premartensitic transformation in Ni_2MnGa. *Phys. Rev. B* **54**, 15045.

Zuo, F., X. Su and K. Wu (1998). Magnetic properties of the premartensitic transition in Ni_2MnGa. *Phys. Rev. B* **58**, 11127.

Curriculum Vitae

Personal data

Name:	**Alexei Timurovich Zaiak**
Date of birth:	April 16, 1976
Place of birth:	Chelyabinsk, Russia
Nationality:	Russian
Marial status:	unmarried
Present position:	PhD student in the group of Prof. Dr. P. Entel at the University Duisburg-Essen, Germany

Graduate program

Sept. 1993:	Enrollment at the Chelyabinsk State University (Physics Faculty)
June 1999:	Master of Science: Physics, Chelyabinsk State University, Chelyabinsk, Russia (Speciality: Solid State Physics) Diploma-thesis: *Structural and magnetic phase transitions in cubic ferromagnets with shape-memory effect*, supervised by Prof. Dr. V. D. Buchelnikov
Since July 2000:	PhD work in the theoretical Low-Temperature Physics section at the University Duisburg-Essen, Germany (Supervisor: Prof. Dr. P. Entel)

Professional experience

- Theoretical study of coupled electromagnetic and magnetoelastic surface waves in antiferromagnets (Research project at the Chelyabinsk State University).
- Ginzburg-Landau theory for structural and magnetic phase transitions in ferromagnets (Diploma thesis).
- *Ab-initio* density functional simulations of crystal structures: Electronic structure, magnetic order, phase stability, phonons.
- Development of scientific software in UNIX enviroments using programming languages C/C++, Fortran, Perl.
- Practical work on different kinds of computers: PCs, work-stations, massive-parallel super-computers (CRAY, IBM, HP).

Languages

Native Russian, working English, and basic German.

List of publications

[I] V. D. Buchelnikov, A. N. Vasil'ev, A. T. Zayak, and P. Entel, The influence of magnetoelastic interaction on structural phase transitions in cubic ferromagnets, JETP **92**, 1019 (2001).

[II] V. D. Buchelnikov, V. S. Romanov, and A. T. Zayak, Structural phase transitions in cubic ferromagnets, J. Magn. Magn. Mater. **191**, 203 (1999).

[III] V. G. Shavrov, V. D. Buchelnikov, and A. T. Zayak, Phase transitions in an Ni-Mn-Ga ferromagnetic alloy with allowance for the modulation order parameter, Phys. Met. Metallogr. **89**, Suppl. 1, S84 (2000).

[IV] V. D. Buchelnikov, A. T. Zayak, A. N. Vasil'ev, D. L. Dalidovich, V. G. Shavrov, T. Takagi, and V. V. Khovailo, Phase transitions in ferromagnetic $Ni_{2+x}Mn_{1-x}Ga$ alloys with regard for the modulation order parameter, JETP **92**, 1010 (2001).

[V] V. Buchelnikov, A. Zayak, A. Vasilév, and T. Takagi, Phenomenological theory of structural and magnetic phase transitions in shape memory Ni-Mn-Ga alloys, Int. J. Appl. Electromagn. Mech. **12**, 19 (2000).

[VI] V. D. Buchelnikov, A. T. Zayak, and P. Entel, Magnetoelastic influence on structural phase transitions in cubic ferromagnets, J. Magn. Magn. Mater. **242-245**, 1457 (2002).

[VII] A. T. Zayak, V. D. Buchelnikov, and P. Entel, A Ginzburg-Landau theory for Ni-Mn-Ga, Phase Transitions **75**, 243 (2002).

[VIII] A. T. Zayak, P. Entel, J. Enkovaara, A. Ayuela, and R. M. Nieminen, First-principles investigations of homogeneous lattice-distortive strain and shuffles in Ni_2MnGa, J. Phys.: Condens. Matter **15**, 159 (2003)

[IX] A. T. Zayak, P. Entel, and J. Hafner, A first-principles investigation of tetragonal and orthorhombic deformations in the ferromagnetic Heusler alloy Ni_2MnGa, J. Phys. IV France (ICOMAT'02) **112**, 985 (2003)

[X] A. T. Zayak, P. Entel, J. Enkovaara, A. Ayuela, and R. M. Nieminen, A first-principles investigation of phonon softenings and lattice instabilities in the shape-memory system Ni_2MnGa, Phys. Rev. B **68**, 132402 (2003)

[XI] A. T. Zayak, P. Entel, and V. D. Buchelnikov, Dynamical properties of Ni_2MnGa from density functional calculations, to appear in 2004.

[XII] A. T. Zayak and P. Entel, Role of shuffles and atomic disorder in Ni-Mn-Ga, Mater. Science and Engineering A (ESOMAT'03), accepted.